Enhancing the performance of lithium batteries through the development of improved electrolyte formulation, formation protocol and graphite surface modification

Zur Erlangung des akademischen Grades eines

DOKTORS DER NATURWISSENSCHAFTEN

(Dr. rer. nat.)

der KIT-Fakultät für Chemie und Biowissenschaften

des Karlsruher Instituts für Technologie (KIT)

genehmigte

DISSERTATION

von

Frau Varvara Sharova

KIT-Dekan: Prof. Dr. Reinhard Fischer

Referent: Prof. Dr. Stefano Passerini

Korreferent: Prof. Dr. Helmut Ehrenberg

Tag der mündlichen Prüfung: 13.12.2017

„I have not failed. I've just found 10,000 ways that won't work"

Thomas Edison, inventor

To my mom

ABSTRACT

Lithium-ion batteries are already employed for the realization of small electric vehicles, which offer significant reduction of air pollution. Despite the advantages of the currently used battery materials, the continuous search and implementation of the new materials with improved chemical, physical and electrochemical properties is essential to increase the energy density and, thus, extend the e-vehicle's driving range. On the other hand, the optimization and the better understanding of the state-of-the-art systems is equally important. This information can provide further insights of the currently employed systems and ease the introduction of the new materials. The scope of this thesis is to analyze the influence of electrolyte formulation, formation protocol and the surface modification of graphite on the properties of the anode/electrolyte interface and enhanced lithium battery performance.

Solid polymer electrolytes with either ionic liquids or ceramic fillers plasticizing the polymer have been widely investigated in the recent decades. However, only few literature reports compare the influence of each material on the resulting electrolyte. Therefore, the individual and combined effects of an ionic liquid ($Pyr_{14}TFSI$) and ceramic filler (SiO_2) on the thermal and electrochemical properties of PEO-LiTFSI electrolytes were investigated and are reported herein. The electrolyte containing both components had the lowest glass transition (-60 °C) and melting temperatures (27 °C), the highest conductivity at any investigated temperature and the highest limiting current density (at 40 °C). The quaternary solid polymer electrolyte also exhibited the best long-term cycling performance in Li/LiFePO$_4$ cells.

The imide salt, LiTFSI, which is commonly employed in solid polymer electrolytes, is also considered as an alternative salt for Li-ion batteries. However, the investigation of this salt as an additive has got only minor interest, although it is widely used in commercial batteries. Therefore, the use of LiTFSI and two other imide salts (LiFSI and LiFTFSI) as additives in the organic liquid electrolyte with respect to the state-of-the-art additive, vinylene carbonate, was evaluated and is reported in the thesis. It is shown that the introduction of lithium imide salts in the electrolyte considerably improved the 1st cycle coulombic efficiency and the long-term cycling stability of graphite/LiFePO$_4$ cells. Using LiTFSI, a capacity fading of only ~2% occurred over 600 cycles while the control cell with the state-of-the-art additive (VC) lost ~20% of the initial capacity. The results of XPS analysis and impedance spectroscopy of graphite electrodes showed that, after the formation cycle, the SEI obtained in the presence of imide salts was thinner, less resistive and contains more LiF than that obtained using VC. The additional study using different ratios between the main salt (LiPF$_6$) and LiTFSI proved that LiF mostly originates from the decomposition of LiPF$_6$, thus indicating the stability of the imide salt towards cathodic currents. Despite the beneficial effect of the imide salts on the lithium-ion cell performance, a slightly reduced thermal stability of the SEI was observed.

The tuning of the electrolyte composition is an effective strategy for the formation of a stable SEI on the anode surface. On the other hand, the sequence of initial cycles, necessary for the SEI build-up (usually called simply formation) can significantly affect this process. Hence, the influence of three different formation protocols on the cell cyclability and possible time reduction via the use of a dual-current protocol was also discussed. This protocol yielded higher rate capability and comparable capacity retention in the full cells with respect to the industrial counterpart. The XPS investigation on the graphite electrodes revealed possible dissolution of the SEI upon discharge, which was more pronounced with industrial protocol with respect to lab standard and dual-current counterparts. HRTEM images indicated that the formation of the SEI rather occurred in between the graphene layers on the contrary to the common idea of its formation on the anode surface. According to the images, industrial protocol led to the least pronounced surface amorphization, which was attributed to the higher cycling temperature accelerating the process kinetics. Overall, the dual-current protocol seemed to be an acceptable alternative to the industrial one, allowing simpler settings. Although the initial validation in the pouch cells showed higher impedance with dual-current protocol compared to the lab standard counterpart, further investigations on the pouch cell level are required to complete the study.

Finally, the optimization of the graphite material could enhance its performance, especially the rate capability. This was evaluated via the application of a carbon-coating, which was reported to enhance lithium diffusion in the material. Only cheap and environmentally friendly materials were considered as possible carbon precursors. It was shown that the coating reduced the first cycle coulombic efficiency by 3–10% compared to pristine graphite due to the increase of the surface area available for the continuous electrolyte decomposition. However, the use of citric acid as a carbon source (5 wt%) improved the rate capability of graphite, resulting in the specific delithiation capacity at 3C of 228 mAh g^{-1} *vs* 211 mAh g^{-1} for the uncoated graphite. The attempt to reduce the coating amount from 5 to 2 wt% resulted in a lower rate capability, but the 1st cycle coulombic efficiency was similar to that of pristine graphite.

ZUSAMMENFASSUNG

Lithium-Ionen-Batterien sind unabkömmlich für die Realisierung von Elektrofahrzeugen, die eine deutliche Reduzierung der Luftverschmutzung ermöglichen. Trotz der Vorteile der derzeit verwendeten Batteriematerialien ist die kontinuierliche Suche und Implementierung von neuen Materialien mit verbesserten chemischen, physikalischen und elektrochemischen Eigenschaften von zentraler Bedeutung, um die Energiedichte zu erhöhen und somit die Reichweite des E-Fahrzeugs zu erweitern. Andererseits ist ein besseres Verständnis der heutigen Systeme ebenso wichtig, um Optimierungen zu ermöglichen und die Einführung neuer Materialien zu erleichtern.

In dieser Arbeit wird der Einfluss von Formierungsprotokollen, der Elektrolytzusammensetzung und von Oberflächenmodifikation von Graphit auf die Eigenschaften der Anoden/Elektrolyt-Grenzfläche und letztlich auf eine verbesserte Batterieleistung hin untersucht.

Polymerelektrolyte, die entweder ionische Flüssigkeiten oder Keramikfüllstoffe enthalten, wurden in den letzten Jahrzehnten weitgehend untersucht. Nur wenige Literaturberichte vergleichen jedoch den Einfluss der einzelnen Komponenten auf den resultierenden Elektrolyten. Daher wurden die individuellen und kombinierten Einflüsse einer ionischen Flüssigkeit ($Pyr_{14}TFSI$) und eines keramischen Füllstoffs (SiO_2) auf die thermischen und elektrochemischen Eigenschaften eines PEO_{20}-LiTFSI Systems untersucht. Der Elektrolyt mit beiden Komponenten zeigt den niedrigsten Glasübergangspunkt (-60 °C) und die niedrigste Schmelztemperatur (27 °C), die höchste Leitfähigkeit bei jeder untersuchten Temperatur und die höchste Grenzstromdichte (bei 40 °C).

Das Leitsalz, lithium bis(trifluoromethansulfonyl)imid (LiTFSI), das üblicherweise in Polymerelektrolyten verwendet wird, kann auch als alternatives Salz in Li-Ionen-Batterien eingebracht werden. Die wissenschaftliche Untersuchung dieses Salzes als Additiv ist von großem Interesse, da es in kommerziellen Batterien bereits weit verbreitet ist. Daher wurden LiTFSI und zwei ähnliche Imidsalze als Additive in organischen flüssigen Elektrolyten und im Vergleich zu einem organischen Additiv, Vinylencarbonat (VC), untersucht. Die Verwendung von Lithiumimidsalzen in Elektrolyten führt zu erheblichen Verbesserungen der Coulomb-Effizienz des ersten Zykluses und der Langzeitstabilität von Graphit/$LiFePO_4$ Knopfzellen. Die Ergebnisse der XPS-Analyse und Impedanzspektroskopie an Graphitelektroden zeigen, dass die Passivierungsschicht (SEI – solid electrolyte interface) nach der Formierung dünner und weniger widerstandsfähig ist und mehr LiF enthält, wenn Imidsalze statt VC verwendet werden. Trotz der vorteilhaften Auswirkung der Imidsalze auf die Leistung der Lithium-Ionen Zellen wird eine verringerte thermische Stabilität der SEI beobachtet.

Die sorgfältige Formulierung des Elektrolyten ist eine wirksame Strategie zur Bildung einer stabilen SEI auf der Anodenoberfläche. Außerdem kann die Art der Formierung während der ersten Zyklen, die für den SEI-Aufbau erforderlich ist, diesen Prozess signifikant beeinflussen. Daher wirde auch der Einfluss von drei verschiedenen Formierungsprotokollen (Laborstandard-, Dual-Current-, und industrielles Protokoll) auf die Zyklisierbarkeit und auf mögliche Zeitreduzierung hin diskutiert. Das Dual-Current-Protokoll ermöglicht höhere Ratenfähigkeit und einen vergleichbaren Kapazitätserhalt der Zellen im Vergleich zum industriellen Protokoll. Die XPS-Untersuchung an den Graphitelektroden zeigt eine mögliche Wiederaufbau der SEI während der Entladung. Dieses Phänomen ist bei Verwendung des industriellen Protokolls vergleichsweise stärker ausgeprägt. Insgesamt scheint das Dual-Current-Protokoll eine akzebtabele Alternative zum industriellen Protokoll zu sein.

Schließlich kann die Optimierung des Graphitmaterials, z.B. durch eine Kohlenstoffbeschichtung, die elektrochemische Leistung, insbesondere die Ratenfähigkeit, verbessern. Dabei können nur günstige und umweltfreundliche Materialien als Kohlenstoff Präkursoren verwendet werden. Mit Citronensäure als Kohlenstoffquelle beschichteter Graphit zeigt eine verbesserte Ratenfähigkeit. So können spezifische Delithiierungskapazitäten von 228 mAh g^{-1} bei 3C gegenüber 211 mAh g^{-1} für den reinen Graphit erreicht werden.

LIST OF ABBREVIATIONS

BET	Brunaer-Emmett-Teller
CA	citric acid
CV	cyclic voltammetry
DMC	dimethyl carbonate
DSC	differential scanning calorimetry
EC	ethylene carbonate
EIS	electrochemical impedance spectroscopy
ESW	electrochemical stability window
FEC	fluoroethylene carbonate
GIC	graphite intercalation compound
HEV	hybrid electric vehicle
HOMO	highest occupied molecular orbital
HRTEM	high-resolution transmission electron microscopy
ICE	internal combustion engine
LCO	lithium cobalt oxide, $LiCoO_2$
LFP	lithium iron phosphate, $LiFePO_4$
LIB	lithium-ion battery
LiFSI	lithium bis(fluorosulfonyl)imide
LiFTFSI	lithium (fluorosulfonyl)(trifluoromethanesulfonyl)imide
LiTFSI	lithium bis(trifluoromethanesulfonyl)imide
LSV	linear sweep voltammetry
LTO	lithium titanium oxide, $Li_4Ti_5O_{12}$
LUMO	lowest unoccupied molecular orbital
M_w	molecular weight
CMC	sodium carboxymethyl cellulose
NCM	lithium-nickel-cobalt-mangan oxide, $LiNi_xCo_yMn_zO_2$
Ni-Cd	nickel-cadmium
Ni-MH	nickel-metal hydride
OCV/OCP	open circuit voltage/open circuit potential
PAA	poly(acrylic acid)

PC   propylene carbonate

PEO   poly(ethylene oxide)

PHEV   plug-in hybrid electric vehicle

PVA   poly(vynil alcohol)

Pyr_{14} N-butyl-N-methyl pyrrolidinium

rpm   revolutions per minute

SBR   styrene-butadiene rubber

SEI   solid electrolyte interphase

SEM   scanning electron microscopy

SHE   standard hydrogen electrode

SOC   state of charge

SPE   solid polymer electrolyte

TGA   thermogravimetric analysis

TM   transition metal

UV   ultraviolet

VC   vinylene carbonate

XPS   X-ray photoelectron spectroscopy

XRD   X-ray diffraction

CONTENTS

1. MOTIVATION

Renewable energy sources, such as wind, solar and hydropower have been widely accepted as alternatives to the current energy production, based on fossil fuels, in order to reduce the negative impact of greenhouse gases (CO_2 or CH_4) emissions on our planet. As the renewable energy sources are weather-dependent, the generated energy needs to be properly stored for the following use. Rechargeable batteries are suitable energy storage systems that convert electricity to the chemical energy and back with zero pollution. These batteries can also supply the energy to an electric motor for vehicular propulsion, thus making the replacement of the internal combustion engine (ICE) possible. Indeed, Ni-MH or lead acid secondary batteries have been already employed for hybrid electric vehicles (HEV) and plug-in hybrid electric vehicles (PHEV). Lithium-ion batteries (LIBs), which were first commercialized by Sony Corporation for the use in portable devices back in 1991 [1], are widely used to power electric-driven cars. Although Sony was the first company to manufacture LIBs for mass production, the pioneering concepts of a battery based on the intercalation materials was introduced by M. Armand already in 1970s. The possibility of partial or full substitution of ICE by the electric motors, allowing a significant reduction of CO_2 and CH_4 emissions and decreasing the oil dependence on the politically instable countries [2], was one of the key points driving the beginning of the extensive research in the field of LIBs. Later, the portable electronic market, aiming for lighter and smaller devices, accelerated the development of these batteries.

The comparison of the characteristics of the most common rechargeable battery types is reported in Table A1 (APPENDIX 1). The most obvious advantages of LIBs with respect to other batteries are the higher gravimetric and volumetric energy densities (Figure 1), which enable the use of smaller and lighter battery units. These two parameters are equally important for both portable electronics and automotive industries. Other important advantages of LIBs are the low self-discharge and no memory effect, the latter being a big issue, for example, for Ni-MH batteries. However, in terms of the driving range LIBs are still not competing with conventional gasoline, which can provide up to 80 times higher gravimetric and 20 times higher volumetric energy densities [3].

Commercial LIBs use graphite as anode material due to its low potential, close to that of lithium metal, enabling high cell voltage, stable long-term cycling performance, and relatively low cost. However, the moderate theoretical volumetric capacity, the limited lithium ion transport especially at high cycling rates (determined by the graphite structure), and the irreversible lithium consumption in the initial cycles (related to the formation of a passivation film) present significant drawbacks. Besides that, other challenges for lithium-ion battery technology include

safety issues and high production costs (current price including the cell pack is in the range of 200-250 \$/kWh [4, 5]). Although the overall toxicity of LIBs compared to lead-acid or Ni-Cd batteries is relatively low, the use of organic solvents as electrolyte components yields thermal instability, increased flammability, risk of leakages, sensitivity towards hydrolysis and possible release of the toxic products upon electrolyte decomposition [6].

Extended research has been dedicated to the identification of possible solutions for reducing the irreversible lithium losses via, for example, optimization of the electrolyte composition. As the state-of-the-art liquid electrolytes present good combination of low viscosity, high salt dissociation, relatively wide liquid range, and good ionic conductivity, one cost-efficient approach is the introduction of additional components (or additives) in small amounts, which assist in the anode passivation and reduce the irreversible lithium consumption. Some of these additives can also improve the safety performance of the batteries, preventing their ignition via, e.g., a shut-down mechanism. The formation itself, which refers to the number of initial cycles required for the anode passivation, is a time-consuming and expensive industrial process. Therefore, the better understanding of the influence of such parameters as current density and temperature as well as the design of the new protocols are highly desirable. The transport limitations of lithium in graphite anodes at higher current densities are related to the material itself and might be tuned by manipulating its structure.

The safety issues of LIBs are addressed by searching for alternative solvents and salts with lower toxicity, including the possible application of the ionic liquids. Additionally, solid electrolytes are considered, as they prevent the leakage of toxic liquid components, and also act as separators, which might lead to the possible reduction of battery manufacturing costs in the future.

Although lithium-ion batteries offer several significant merits with respect to other rechargeable battery types, the system is still young, compared, for example, to the more mature lead-acid technology, known since the late 1850s. Thus, the ongoing technology development and introduction of optimized and new materials and processes, enabling further increase in the energy density and safety, and subsequent cost reduction, is of high importance.
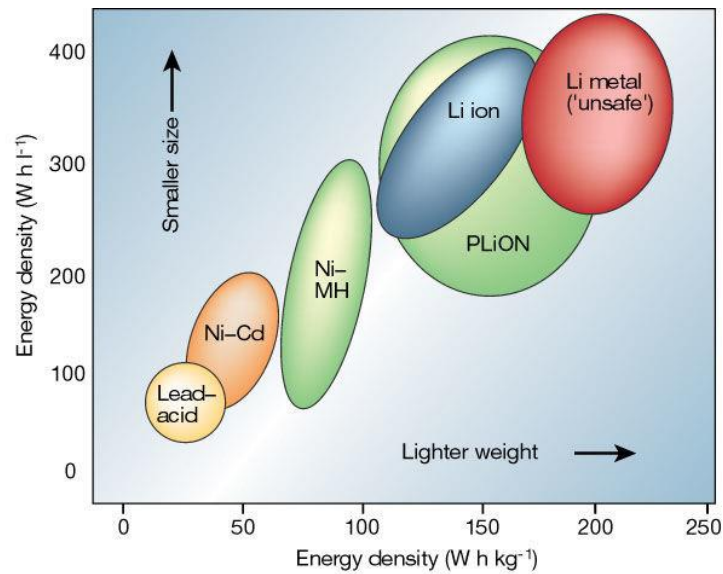
Figure 1. Ragone plot comparing different battery technologies in terms or volumetric and gravimetric energy densities (taken with permission from Ref.[7]).

The spectra of different applications, in which lithium-ion batteries have been already employed, is graphically shown in Figure 2. Although LIBs are still mostly used for portable devices and small power tools, the rapid increase of the battery sales for automotive applications can be clearly observed from 2012 to 2015. This is not only related to the appearance of such outstanding car manufacturers as Tesla, but also to the push of several countries towards reduction of combustion engine-driven vehicles. For example, according to the Climate Action Plan 2050, by 2030 only zero-emission vehicles should be sold in Germany. Whether this deadline would be reached or not, it is clear that further increase in the electrified automotive sales can be expected and with that the "better" batteries are highly desirable.
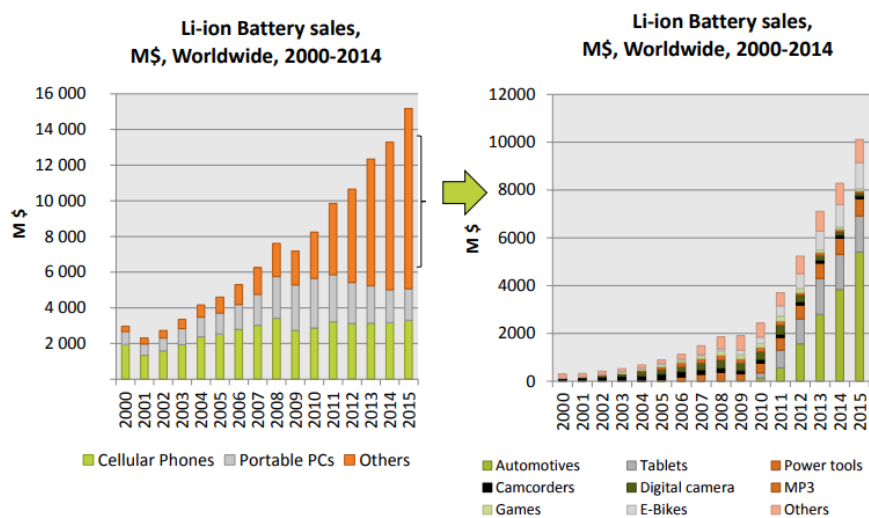
Figure 2. Li-ion battery sales charts by applications (taken from Ref.[8], available online).

As a personal motivation for my research I would like to highlight my hope to contribute for making the planet cleaner through the use of sustainable and environmentally-friendly technology. The statistics shows that Russia (my homeland) is one of the biggest oil producers in the world. According to the Ministry of Natural Resources and Environmental Protection of Russia available oil reserves will be depleted by 2044 with the current consumption rate [9]. Besides that, Russia is the 4th world largest producer of CO_2, which, taking into account the big territory, can also influence the changes in the international climate. Initial measures towards the reduction of carbon dioxide emissions are being taken by the Russian government. By 2030 the government plans to attract \$53 billion for the renewable energy sector [10]. Taking into account the high popularity of German cars among Russian drivers, I hope that the faster change to hybrid or fully electric vehicles in Europe would accelerate the development of renewable energy sources and the use of electric vehicles in Russia as well.

2. INTRODUCTION: LITHIUM-ION BATTERIES

It should be noted that a lithium-ion "cell" is a single unit reversibly converting chemical energy into electrical, whereas a lithium-ion "battery" is a stack of cells, connected in series. In this thesis, for sake of simplicity, both terms will be used to describe a single cell.

2.1 Working principle

Lithium-ion batteries consist of two electrodes. The positive (cathode) is casted on aluminum current collector and the negative (anode) is casted on copper current collector. The two electrodes are separated by a thin electron-insulating layer (called separator) soaked with the electrolyte (liquid or solid ionically conducting media). During the charge (i.e., upon application of an anodic current) lithium ions are extracted from the lithium-containing cathode, shuttled through the separator/electrolyte and intercalated into the anode host structure. Simultaneously, the electrons are flown through the external electric circuit in the same direction. This process spontaneously progresses in the reversed direction on discharge, thus providing the electrical power as shown in Figure 3. Due to its working principle LIBs are often termed as "rocking chair" batteries [11].
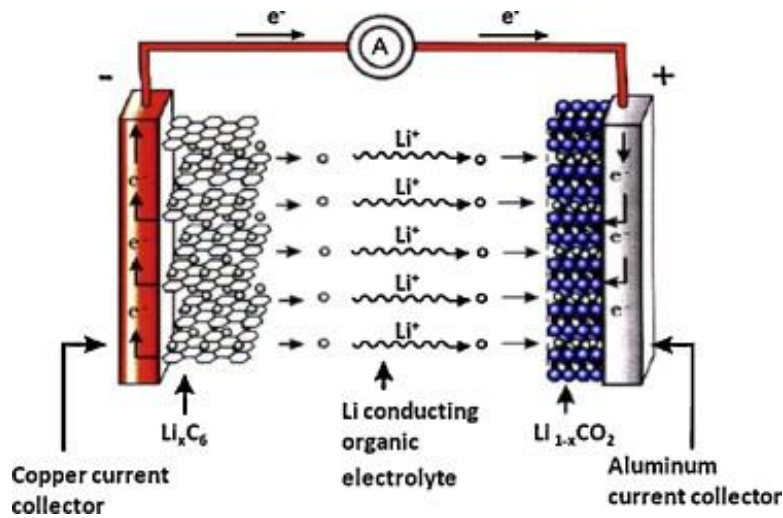
Figure 3. Scheme of a lithium-ion battery working principle (taken with permission from Ref.[2]).

The most commonly used anode material is graphite, whereas lithium metal oxides $LiMO_2$ (i.e., $LiCoO_2$) are employed as positive electrode material. The reversible reactions occurring at the electrodes upon charge/discharge can be then expressed in the following way:

$$anode: C_y + xLi^+ + xe^- \leftrightarrows Li_xC_y \qquad (2.1)$$
$$cathode: LiMO_2 \leftrightarrows xLi^+ + xe^- + Li_{(1-x)}MO_2 \qquad (2.2)$$
$$overall: C_y + LiMO_2 \leftrightarrows Li_xC_y + Li_{(1-x)}MO_2 \qquad (2.3)$$
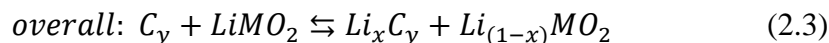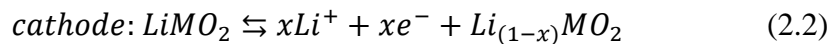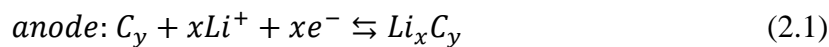
The electrolyte is usually a mixture of cyclic and linear aliphatic carbonates (such as ethylene carbonate and dimethyl carbonate, respectively), in which the lithium salt is dissolved. Among the available salts, lithium hexafluorophosphate ($LiPF_6$) is the most frequently employed one. The separator typically consists either of a polymeric membrane (polyethylene, polypropylene or their blend) or of non-woven fabric mat (polyolefin, polyamide, etc.) [12]. The properties, challenges and promising alternatives of the main battery components will be discussed in details in the following subchapters.

2.2 Battery definitions

The total charge per weight (Ah kg^{-1}) or per volume (Ah L^{-1}) transferred by the current I on charge or discharge is:

$$Q = \int_o^{\Delta t} I dt = \int_o^Q dq \qquad (2.4)$$

$Q(I)$ is usually called "capacity" and depends on the applied current. The current used to cycle a battery is generally defined as the rate at which battery is charged/discharged with respect to its maximum (theoretical) capacity. For example, 1C rate means that the current will charge/discharge the battery in 1 hour. For a battery with a capacity of 100 Ah, this equals to a charge/discharge current of 100 A.

Such important parameter as density of stored energy depends on the discharge current and can be acquired by measuring the time necessary for the complete battery discharge (or capacity):

$$Energy(q, I) = \int_o^{\Delta t} IV(t) dt = QV_{av}, \qquad (2.5)$$

whereas the output (instantaneous) power depends on the output voltage and can be expressed in the following way:

$$Power(q) = V(q)I_{dis} \qquad (2.6)$$

The energy is measured in Watt-hour (Wh) and can be either expressed per mass (Wh kg^{-1}) or per volume (Wh L^{-1}), whilst the unit for measuring the battery power is Watt (W), and similarly, volumetric (W L^{-1}) and specific/gravimetric (W kg^{-1}) power densities can be evaluated.

The reversibility of the charge/discharge processes is measured by the coulombic efficiency, expressed in %, and calculated using the following formula:

$$Efficiency = \frac{Q_{dis}}{Q_{ch}} \times 100 \qquad (2.7)$$

The capacity retention represents the ratio between discharge capacities in n^{th} and 1st cycles, calculated using the formula:

$$Capacity\ retention = \frac{Q_{dis_{n^{th}\ cycle}}}{Q_{dis_{1^{st}\ cycle}}} \qquad (2.8)$$

The cycle life of the battery for EV applications is usually determined by the number of cycles, for which the capacity retention is higher than 80% of the initial capacity value.

2.3 Electrode materials for Li-ion batteries

In principle, lithium-ion battery operates as a galvanic cell during discharge and as an electrolytic cell during charge. Hence, upon discharge the negative electrode acts as the anode (undergoing oxidation), whereas the positive electrode is the cathode (undergoing reduction). Upon charge the redox reaction is reversed, and so does the designation of the electrodes. Thus, it is more correct to denote the electrodes as negative and positive, which is independent of the operation mode. However, in this thesis for simplicity the galvanic cell mode (discharge) is used for the electrodes designation. Therefore, graphitic carbon is always denoted as the anode (or negative electrode), whereas lithium iron phosphate is designated as the cathode (or positive electrode).

2.3.1 Electrode/electrolyte stability and solid electrolyte interphase

Prior to the introduction of the main types of anode materials, it is necessary to present the solid electrolyte interphase (SEI), which plays an important role in the cycling performance of LIBs. The SEI is a passivation film forming on the surface of the electrode during the first charge/discharge cycle and protecting it from continuous reactions with electrolyte.

Both for the anode and the cathode, the formation of the SEI is related to the electrochemical instability of the electrolyte at low and high voltages, respectively. On the negative electrode the reduction of the electrolyte is attributed to the energy of the anode Fermi level being higher than the lowest unoccupied molecular orbital (LUMO) of the electrolyte, causing its decomposition (Figure 4). The same is also true for the cathode, whose Fermi level has a lower energy than the highest occupied molecular orbital (HOMO) of the electrolyte, initiating oxidation of the electrolyte. In fact, the voltage range between HOMO and LUMO, in which the electrolyte does not undergo reductive/oxidative decomposition defines its electrochemical stability window (ESW).
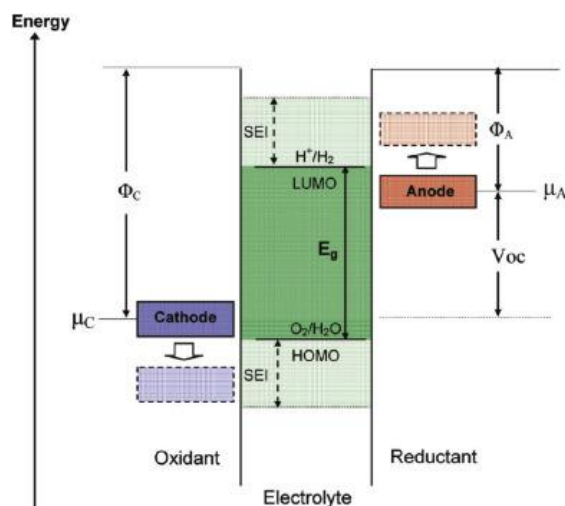
Figure 4. Energy distribution upon the formation of anode and cathode SEI under electro-redox conditions (taken from Ref.[13], open access article).

The SEI concept was first introduced by E. Peled [14] for the alkali metals, and later extended to carbon materials by Dahn et al. [15]. The formation of the SEI is vital to ensure long cycle life, good rate capability and improved safety of the LIBs. Recently, various research groups evidenced formation of similar passivation film on the cathode surface (aka cathode electrolyte interphase, CEI) [16, 17]. However, the composition and the role of the CEI require further investigation.

The perfect SEI (CEI) should act as an electronic insulator but be permeable to the transfer of lithium ions. The formation kinetics should be fast to reduce the irreversible losses. Furthermore, it should have uniform morphology and composition. Finally, it should be flexible and elastic to accommodate the volume changes of the active material upon repeated charge/discharge cycles.

2.3.2 Lithium metal anodes

Lithium metal batteries have been intensively investigated since 1970s. Indeed, the use of lithium metal as anode offers several significant advantages, such as the lowest redox potential (-3.04 V *vs* SHE), and high theoretical capacity (~3860 mAh g^{-1}), thus, enabling high theoretical energy density. Upon storage lithium spontaneously reacts with the atmospheric gases and a passivating surface film is formed. When assembled in a cell it further reacts with most of the aprotic solvents and commonly used salt anions (including PF$_6^-$) of the electrolyte, resulting in the formation of a secondary passivation layer, consisting of different lithium salts, such as LiF or Li$_2$CO$_3$ as well as organic compounds [18].

The main challenge with commercialization of Li metal batteries is related to the inhomogeneous metal plating upon cycling that leads to the formation of "dendrites" on the

lithium anode surface, whose formation mechanism is shown in Figure 5. This phenomenon poses serious safety concerns as the uncontrolled growth of dendrites results in the separator penetration, leading to internal short circuits. The latter may induce local heating, thermal runways and finally, in the worst case scenario, battery fire and explosion [18, 19]. Additionally, the continuous renewal of the lithium surface results in a low coulombic efficiency, which limits the cycle life of the battery. Moreover, SEI on the lithium surface is quite stiff and incoherent, which results in its cracking upon continuous cycling.
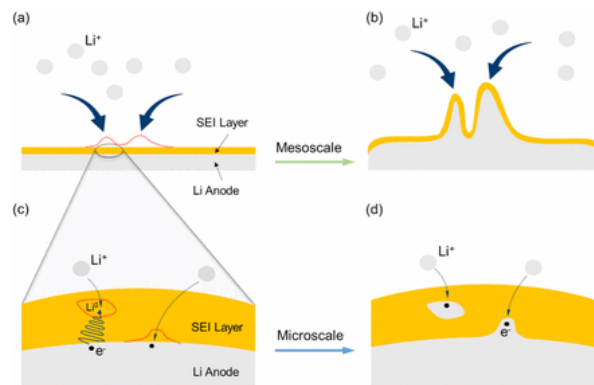

Figure 5. Schematic diagrams of the dendrites formation and growth: a) and b) Li plating at the anode surface, c) and d) nucleation and growth of Li dendrites at the anode surface upon discharge (taken with permission from Ref.[20]).

Several strategies have been developed to overcome the dendrite formation and growth via, for example, using particular electrolyte salts [21], solvents [22] or additives [23-27], enabling the formation of stable and flexible SEI. A possibility of forming an artificial SEI with desirable properties on the fresh lithium surface has also been evaluated in some of the recent studies [28, 29]. Finally, the substitution of the liquid organic electrolytes by solid polymer electrolytes was shown to effectively suppress but not completely prevent the dendrite growth on lithium metal, especially at higher current densities [30, 31]. Although solid polymer electrolytes are promising candidates for the commercialization of Li-metal batteries, they bring several issues, which will be further addressed in Section 2.4.2.

2.3.3 Graphitic carbon anodes

Carbon is a unique material, which is used for various applications: from jewelry to electronic gadgets and pencil leads. Since 20 years carbonaceous materials have been also employed as negative electrode in lithium-ion batteries. Carbonaceous materials have low redox potential *vs* lithium, high Li diffusivity and high electric conductivity. They also show moderate volume expansion upon lithium intercalation/deintercalation. Furthermore, their low cost and abundancy make them a state-of-the-art material, still unbeatable by other anode candidates (such as spinels, alloying or conversion materials) [32, 33]. Although graphitic carbon

possesses relatively high gravimetric capacities, the volumetric capacity is not high enough (~830 mAh cm^{-3}) to satisfy the growing needs on the increased energy densities for the wider driving range of the electric vehicles. Additionally, the low intercalation rate capability limits the use of this material for high power applications [34].

In general, carbon materials can be categorized into graphitic and non-graphitic carbons, as displayed in Figure 6. Graphitic carbon is a polycrystalline material, which consists of graphene sheets bonded together by weak van der Waals forces into ABAB… stacking order along the *c*-axis with a number of structural defects. Although in theory term "graphite" applies only to the material having a perfect stacking order of graphene planes, in practice any material comprised of aggregates of perfectly stacked crystallites with different orientations is also defined as graphite. Graphite lattice belongs to *P*6$_3$/*mmc* space group and comprises two types of characteristic surfaces: normal to (basal) and parallel to the *c*-axis planes (edge or prismatic). Non-graphitic (or disordered) carbons, in turns, also consist of hexagonal graphene layers, but without long-range crystallographic order, also defined as turbostratic disorder. In these materials amorphous regions cross-link the crystalline ones. Non-graphitic carbons can be further classified in graphitizing ("soft") or non-graphitizing ("hard") carbons. The soft carbons are mostly originating from the pyrolysis of liquid precursors (i.e., petroleum pitch) and are able to develop the graphitic structure at elevated temperatures (1500 – 3000 °C) as the cross-linking forces are weak and the graphene layers can freely move. Hard carbons, produced mainly by pyrolysis of solid precursors (such as chars or glassy carbons), show no graphitic ordering even during high temperature treatment as the motion of the layers is hindered by strong cross-linking.
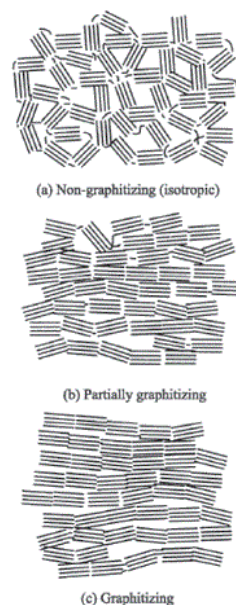

Figure 6. Graphene stacks in a)-b) non-graphitic and c) graphitic carbons (taken from Ref.[35]).

Both soft and hard carbons generally offer higher capacities as compared to graphite. Soft carbons are typically pyrolyzed at lower temperature, which results in the high amount of hydrogen in the carbon layers. Lithium intercalation is believed to occur at the sites close to the hydrogen atoms. Upon lithiation the modifications of C-H bonds occur due to (H-C)-Li bridging, resulting in carbon transformation from sp^2 to sp^3 hybridization [33, 36]. This leads to the large hysteresis and higher voltage required for lithium deintercalation [37], which lowers total (cell) voltage and reduces the volumetric capacity. Therefore, soft carbons are not considered as anode materials in LIBs. Hard carbons are generally heat-treated at high temperatures ($\geq$1000 °C); thus, the hydrogen content can be substantially decreased. On the contrary to soft carbons, hard carbons are believed to consist of two domains, including carbon layers and micropores. Both domains can accommodate lithium ions in accordance to the model, known as the "house of cards" [38-40], resulting in high Li^+ storage capability. However, hard carbons have low density, which negatively affects the volumetric energy density, and high surface area, leading to high irreversible lithium losses due to extended electrolyte decomposition. Therefore, in lithium-ion batteries hard carbons are rather employed as additives to increase the electronic conductivity of the electrode. Per contra, hard carbons have been widely employed as anode materials for sodium-ion batteries, in which the use of graphite is hindered due to the mismatch between the graphite interlayer spacing and the size of Na ions, and higher potential of Na (-2.7 V *vs* SHE) than that of Li [41, 42].

As mentioned above, since 20 years natural or synthetic graphite has been the most commonly used anode material for Li-ion batteries. Lithium intercalates in between the graphene planes, resulting in the storage of up to 1 Li atom per 6 C atoms, corresponding to the theoretical capacity of 372 mAh g^{-1}. Intercalation is only possible along the edge (or prismatic) planes (Figure 7), whereas at the basal planes the ion transfer can occur only through the defects [43]. Therefore, the electrochemical performance of the graphite varies depending on the ratio between the edge-plane to basal-plane area [44]. Upon the intercalation the stacking order of the layers is changing from A-B-A-B-A to A-I-A-I-A to accommodate the intercalant I, accompanied by the increase in the graphene interlayer distance by ~10%, resulting in the formation of the so called graphite intercalation compounds (GICs) [45, 46].
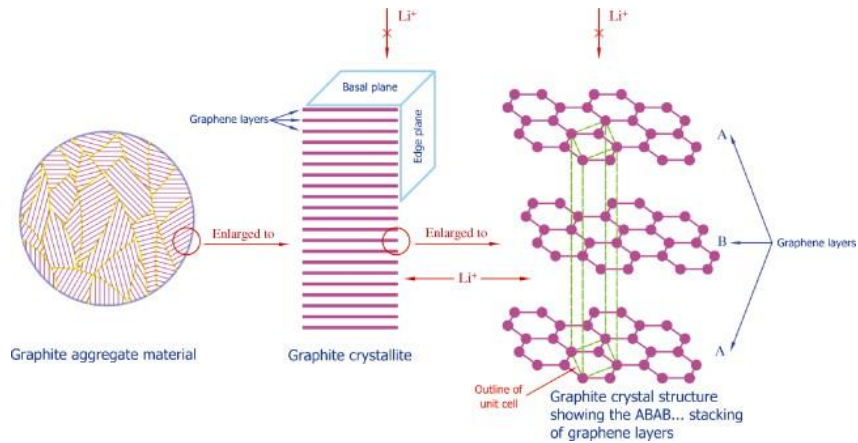
Figure 7. a) Graphite material and its crystallites (taken with permission from Ref.[44]).

The formation of GICs occurs via the staging mechanism, which is schematically shown in Figure 8. Staging denotes the number of intercalate layers in between the graphene sheets. Depending on the lithium concentrations, four stages of Li-GICs can be identified, each of those existing in a narrow concentration range, corresponding to a specific voltage. As displayed in the schematic voltage profile in Figure 8, through the whole concentration range the coexistence of the two stages is observed, indicated by the voltage plateaus. The stage *IIL*, which represents the liquid-like stage *II*, has a different lithium packaging density and no in-plane ordering [43, 47]. In reality the transitions between the stages in the voltage profiles are very smooth due to only slight variation in Li_xC_6 packing density. Moreover, the sloping of the plateaus is observed due to various overpotential occurring during the galvanostatic measurements.
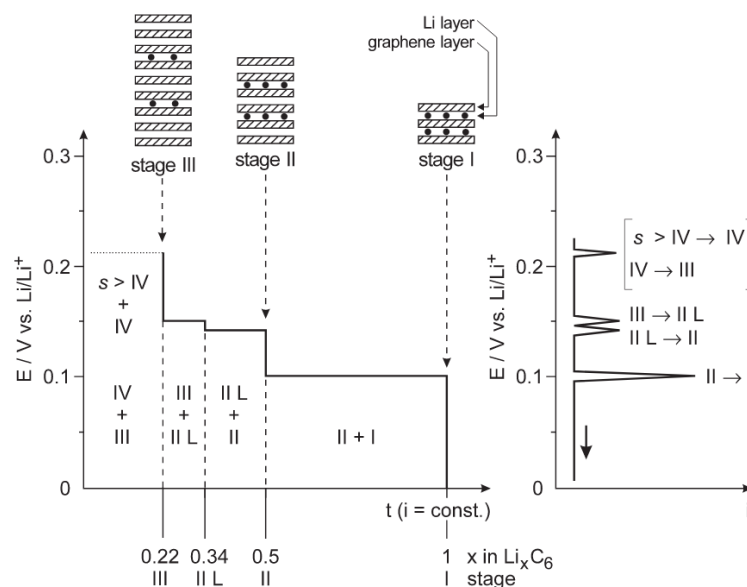

Figure 8. Li staging intercalation into graphite (taken with permission from Ref.[43]).

The reversible lithium intercalation into graphite is granted by the formation of the SEI (Section 2.3.1), composed of the electrolyte reductive decomposition products. As the ionic radius of

lithium ions is much smaller than that of the salt counter anion, lithium ions get solvated by the electrolyte solvent molecules, forming lithium solvation shells [48]. Due to the concentration gradient under the cathodic currents, solvated ions diffuse towards the graphite surface, where the formation of the passivation film is initiated. Despite the similarities in the chemical composition of the passivation films on lithium and graphite, SEI formation on graphite is only expected to start upon anode polarization.

Numerous experimental and computational studies are available on the chemical composition of the SEI on the graphite. However, its formation mechanism, especially the preferential reduction pathways of the electrolyte solvents, is still under debate. According to one theory, the molecule of organic solvents in the solvation shell is favorably reduced to radical anions on the graphite surface, whose further decomposition would form the SEI compounds [15, 49]. Another theory suggests that as the sp^2-hybridized graphene sheets in the graphite are kept together by the weak van der Waals forces, the co-intercalation of solvent molecules coordinating Li^+ is possible, leading to the formation of ternary GICs $Li^+(solv)_yC_n$ [50, 51]. As these GICs are thermodynamically unstable, their decomposition would yield the constituents of the SEI. Although there is no strict agreement in the scientific community on the most correct theory, it is believed that both processes are competing upon graphite polarization.

As mentioned above, poor charge (intercalation) rate capability is one of the significant drawbacks of graphite material. This has been attributed to the morphology of the graphite crystallites and unfavorable orientation of particles, limiting the diffusion rate. Furthermore, the formation of the SEI and its composition determine the kinetics in the cell [52]. For instance, Xu et al. [53] found that the disruption of the lithium solvation shell at the interface, rather than the Li^+ diffusion through the SEI, is the rate-determining step of the lithiation process, accompanied by the consumption of activation energy, and resulting in the lower rate capability (sensitivity towards change of current density) of graphite anodes (Figure 9).
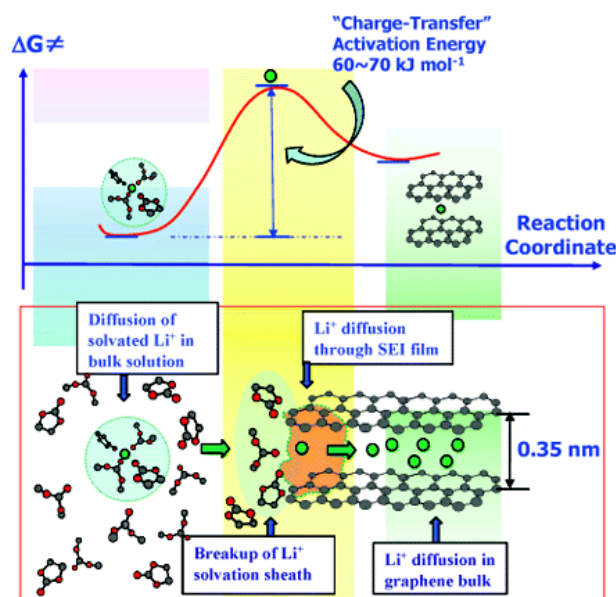
Figure 9. Scheme of the Li$^+$ transfer at the electrolyte/electrode interface (taken with permission from Ref.[53]).

As mentioned in the Section 2.3.1, a perfect SEI should have high electric resistivity, to prevent continuous electrolyte decomposition, and high ionic permeability, to allow fast charge transfer. In addition, SEI should present homogeneous morphology, a thickness of a few Å and a high tolerance towards the anode material volume changes to prevent the continuous exposure of highly reactive anode surface to the electrolyte. Therefore, SEI should be composed of stable and insoluble components like LiF and Li$_2$CO$_3$ rather than metastable organic ROCO$_2$Li and ROLi, which can undergo further decomposition [54, 55]. The fast formation of the SEI is essential to minimize the irreversible capacity losses in the initial cycles and ensure the high capacity retention upon long-term cycling.

Experimental evidences reveal that the SEI consists of two main parts. The outer part of the film is less dense, filled with electrolyte and mostly composed of organic species. In turns, the inner part of the SEI is mostly composed of inorganic species and has a denser morphology, thus protecting the anode surface and preventing continuous electrolyte decomposition. As graphite contains both edge and basal planes, the SEI formed on both kinds of planes is expected to be different in properties and morphology. In particular, SEI on the basal planes does not need to be permeable to ions, but it should be electronically resistive to prevent the electrolyte decomposition. As the lithium intercalation through basal planes is not possible, the SEI formation on these planes should be minimized to reduce the overall capacity losses. In reality, as schematically shown in Figure 10, the SEI structure is very complex and inhomogeneous with a variable thickness across the electrode surface.
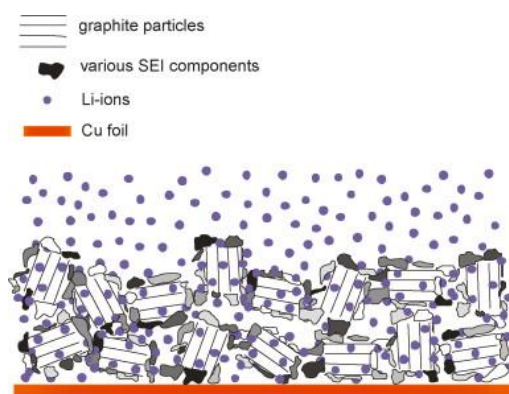
Figure 10. Graphical representation of the lithiated graphite covered by the SEI. The inorganic components are shown in darker color, whereas the organic components are displayed in lighter color (taken with permission from Ref.[54]).

It is generally accepted that the formation of the SEI on the graphite surface takes place between 0.8 and 0.2 V *vs* Li/Li$^+$, but if not complete, it can continue further in parallel with lithium intercalation into the host structure. The formation of the passive layer seems to occur in two stages. At higher potentials the SEI is mostly composed of low-density and loosely packed organic species with low ionic conductivity. These species originate from one-electron transfer reactions of the electrolyte. Upon potential decrease, the SEI becomes more compact and enriched with inorganic components, which have higher ionic conductivity. These inorganic components originate from the multi-electron transfer reactions.

2.3.3.1   *Importance of the formation step*

The process of the SEI construction and stabilization occurring on graphite during the initial cycles is called "formation process" or, simply, formation. The formation is an industrial bottleneck, as it requires specific instrumentation, and a large portion of the battery production plants. Additionally, the formation significantly influences the manufacturing costs of the batteries (up to 30 $/kWh of the total cell cost [5]). Furthermore, the formation duration can vary from 4-5 days up to several weeks, resulting in the additional energy consumption and further capital costs. Three main formation methods are presently used by the battery producers, which include the constant current formation in one or two steps [56], the pulse formation [57] and the elevated temperature aging [58]. On the industrial scale the formation usually presents a combination of the methods in a complex protocol. Due to the high competition between the batteries producers such protocols are often kept non-disclosed, resulting in a lack of scientific and technical literature, hindering the investigation and optimization of the formation step.

Usually relatively low current densities, corresponding to C-rates between C/20 and C/5, are used in the formation protocol. If the current density is low, then the resulting SEI has a higher ionic and lower electronic conductivities, but at the expense of higher plant capital expenses

and production costs associated with the time required for the formation. At higher current densities, the SEI is formed faster but is generally more porous with high ionic and electronic conductivities, leading to the reduced capacity retention [59]. Formation at elevated temperatures (~40 °C) creates a more compact SEI with higher amount of insoluble inorganic components on the surface [13]. One of the latest studies introduced a new formation protocol, consisting of short discharge/charge cycles at high state of charge (SOC), resulting in the reduced interfacial resistance, improved long-term cycling performance, and, most importantly, reduced formation duration by 6 times [60].

2.3.3.2   Carbon-coating of graphitic anode materials

As stated above, one of the significant limitations of graphite is its poor rate performance, especially at reduced (sub-ambient) temperatures. For this, reduced graphite particle size would positively affect the solid-state lithium diffusion, leading to higher delivered capacity at high rates [61]. However, the corresponding higher surface area would result in higher first cycle irreversible capacity loss associated with the SEI formation. Other factors, such as particle morphology, electrode thickness, porosity, choice of binder, and electrolyte composition also affect the rate capability of graphite [34, 62, 63]. Furthermore, surface properties (e.g., presence of defects and resistivity of the passivation layer) are also important as fast charge transfer at the interface is a key factor for high rate performance.

These considerations have driven the interest in graphite surface modification via polymers [64], metals [65], and carbon [66-69] coatings. Focusing on the latter case, it has been reported that amorphous carbon, being isotropic, allows random Li^+ intercalation, which may lead to a better rate capability of carbon-coated graphite [69]. Improved cycling performance in the electrolytes containing high amount of propylene carbonate (PC) has also been reported, showing the protective effect of the coating towards solvent co-intercalation [70].

Several research groups have been working on the use of polymers as carbon precursors. For example, Wang et al. [69] coated artificial graphite with a thin carbon layer derived from glucose. They concluded that the coating could increase the specific capacity and initial coulombic efficiency. The best results were obtained using an aqueous solution (5 wt%) of glucose. Nozaki et al. [68] rationalized the use of different thermoplastic polymers as carbon sources, dividing them into three categories, based on the amount of carbon residue, which directly influences the irreversible capacity loss during the first charge (lithiation) and cycling performance.

Based on the literature survey, the expected performance improvement upon carbon coating is not always observed as it strongly depends on the amount and nature of the carbon layer, the graphite characteristics, and the electrolyte composition [63, 70, 71]. This makes data comparison very difficult, and thus each case has to be evaluated individually via a systematic investigation. Besides the beneficial influence on the graphite rate capability, the coating process should be cost competitive and not detrimental to the environmental. Thus, the carbon precursor should be readily available and the process should employ a relatively low temperature and reduced organic solvent amounts.

2.3.4 Other kinds of anode materials

Although graphite is the state-of-the-art anode material for lithium-ion batteries, the scientific community is constantly investigating possible alternatives in attempt to overcome the drawbacks of graphite and to satisfy the demands of the automotive industry. This subchapter presents a brief overview of the materials, considered as potential negative electrodes for LIBs.

One of such alternative materials, already in use in some commercial batteries, is *spinel* lithium titanium oxide $Li_4Ti_5O_{12}$ (LTO). This material offers improved thermal stability, good cycle life and relatively high volumetric capacity (600 mAh cm^{-3}) [72] but at the expense of high Ti costs (\$661 of pure Ti *vs* \$0.005 of graphite per 100 g) and high working potential (~1.5 V *vs* Li/Li$^+$), resulting in overall low cell voltage. LTO can accommodate up to 3 lithium equivalents with only a small volume change (~0.2%) in the material, manifesting only a minor potential hysteresis [73, 74]. As the operating voltage of the material is above 1 V, the growth of lithium dendrites is hindered. However, the material has a low electronic conductivity and lithium diffusion coefficient, leading to poor rate performance. Moreover, the surface reactions cannot be completely avoided for LTO, leading to a severe gassing upon the reactions with the electrolyte [75]. Although coating of LTO with a carbon layer helps to reduce the gas evolution and the electronic resistance [76, 77], it catalyzes the formation of the SEI. All in all, despite its disadvantages, LTO is a material of choice with excellent long-term cycling stability for high power applications.

Alloying materials represent another class of promising negative electrodes. One of the most widely studied alloying materials is silicon (Si), forming a $Li_{15}Si_4$ alloy below 50 mV *vs* Li/Li$^+$, resulting in a very high theoretical specific capacity of 3579 mAh g^{-1} [78]. Furthermore, silicon is cheap and abundant, which would lead to significant battery cost reduction compared to graphitic carbons. One of the major problems related to the utilization of silicon in lithium-ion batteries is its huge volume expansion (up to 300 %) upon alloying/dealloying. Consequently, an unstable SEI is formed on its surface, leading to the material pulverization and capacity

fading upon cycling. Similar to LTO, silicon has relatively low electronic conductivity and slow lithium diffusivity, negatively influencing its rate performance and hindering the utilization of its full capacity. One of the common approaches to eliminate the disadvantages of this materials is to reduce its particle size to nanoscale [79], thus leading to a better accommodation of the volume change and increasing the surface area for a faster electron transfer and ion diffusion. However, this also results in the decrease of the volumetric capacity. Another opportunity to ameliorate the performance of Si anode is to limit the voltage window, avoiding the formation of crystalline $Li_{15}Si_4$ below 50 mV [78]. The incorporation of silicon nanoparticles in the carbon matrix, which can effectively buffer the volume expansion, has been extensively studied and reported in numerous publications [80-83]. To increase the total cell capacity batteries manufacturers already introduce small amounts of silicon (typically 10-12 wt%) but the implementation of silicon up to 50 wt% remains yet challenging.

Conversion materials utilize the reduction of transition metal (TM) oxides to metallic state with formation of nanograins in the lithium oxide matrix, which "glues" the particles together, following the reaction:

$$TM_xO_y + 2yLi^+ + 2ye^- \leftrightarrow xTM^0 + yLi_2O, \qquad (2.9)$$
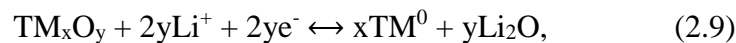
where TM is a transition metal (Co, Ni, Fe, Cu, Mn, Mo, etc.) [84]. The high delivered capacities of these materials are due to the multi-electron processes necessary to completely reduce the transition metal. The most significant drawbacks of conversion materials include high operating potential, large volume expansion and voltage hysteresis for the reaction to occur [85], resulting in a moderate energy density and efficiency. Furthermore, these drawbacks lead to a high first cycle irreversible capacity, originating from incomplete oxidation of Li_nX during anodic sweep [86]. Besides oxides also sulfides, nitrides, phosphides, or carbonates [87] show similar mechanism upon lithium insertion, opening new frontiers for next-generation anode materials. Recently, an interesting approach, combining the alloying and conversion processes in a unique material has been discussed as a possible solution of the individual drawbacks [88].

2.3.5 Overview of the common cathode materials

Since the main interest of the present work is related to the anode materials and negative electrode/electrolyte interphase, only a brief overview of the most commonly employed cathode materials will be presented in this section. Their crystal structures are displayed in Figure 11.
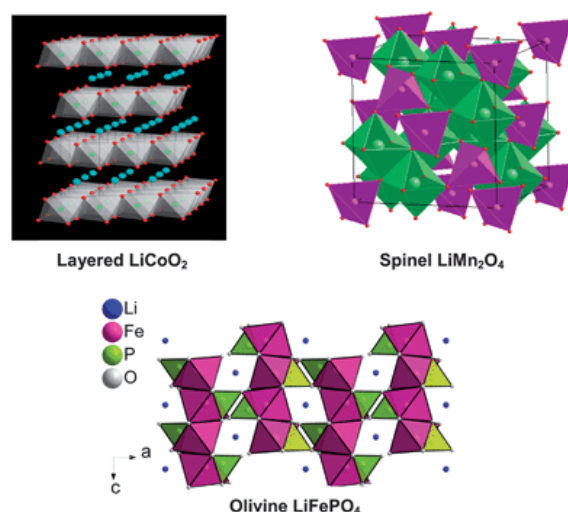
Figure 11. Crystallographic structures of the most commonly used cathode materials (taken with permission from Ref.[89]).

Olivine-type cathode material $LiFePO_4$ (LFP) offers several advantages such as flat voltage plateau, high theoretical capacity (170 mAh g^{-1}), and good thermal and chemical stability. The latter is related to the presence of covalent-bonded PO_4 groups and stable Fe^{2+}/Fe^{3+} redox couple [90]. Moreover, this material is cheap and offers high level of safety. On the other hand, LFP suffers from sluggish 1D lithium diffusion [91]. Furthermore, it has moderate working potential and low electronic conductivity. To address the latter issue, carbon-coating is usually applied to prevent the growth of the particles during synthesis and to enhance the conductivity [92]. Alternatively, Fe^{2+} is partially substituted by Mn^{2+}, resulting in $LiFe_{1-y}Mn_yPO_4$ (LFMP), allowing an increase of working potential by ~0.4 V compared to that of LFP [93]. This is due to the access to Mn redox couple, incrementing the energy density of LFMP compared to LFP. However, the capacity loss of LFMP, attributed to the material's structural instability and low electronic conductivity with increase of Mn content, is one of the main drawbacks of this material [94]. Therefore, a low-level Mn^{2+} content seems to be preferable.

Layered oxide cathodes, with 2D diffusion pathways generally deliver higher theoretical capacities compared to those of olivines. $LiCoO_2$ (LCO) was the first layered cathode material to be commercially available with relatively high theoretical capacity (274 mAh g^{-1}), low self-discharge and good cycling performance [95, 96]. The major drawbacks of LCO include lattice distortion upon deep delithiation (above 4.2 V), low thermal stability, and high cost. In attempt to reduce the cathode costs and substitute the toxic Co, $LiNiO_2$ and $LiMnO_2$ have been investigated as alternatives to LCO [96]. However, $LiNiO_2$ is difficult to synthesize using usual synthesis routes [97], whereas $LiMnO_2$ tends to transform into spinel during discharge [98]. Another issue of the latter material is the dissolution of Mn^{2+} due to the disproportionation reaction ($2Mn^{3+} \rightarrow Mn^{4+} + Mn^{2+}$) and its migration towards the anode [99, 100]. The effort

spent to ameliorate this class of materials led to the development of $LiNi_xCo_yMn_zO_2$ (NCM), which is a state-of-the-art cathode nowadays. NCM is one of the best performing materials with relatively high theoretical capacity (160 mAh g^{-1}) and enhanced thermal stability in charged state with a high operating voltage (3.0 – 4.5 V). However, at high charge voltage the transition metal dissolution issue persists, leading to a fast cell failure [101].

Finally, *spinel* $LiMn_2O_4$, allowing 3D lithium diffusion, is a low-cost, abundant and safe material with respect to LCO. However, similar to layered $LiMnO_2$ this material suffers from unsatisfactory long-term performance, oxygen loss from delithiated material, Mn dissolution and phase change during continuous charge/discharge [16, 102]. Reduction of the particle size [32], doping with other metals [103] and surface coating [104] have been shown to improve the rate performance and capacity retention of the spinel.

The actual offer of the cathode materials is wider than that presented here. Depending on the application needs, the proper selection of the available anode and cathode materials is necessary. Nevertheless, the constant development of the new materials is also essential to overcome the drawbacks of the present systems.

2.4   Electrolytes for lithium-ion batteries

2.4.1   Aprotic organic liquid electrolytes

An electrolyte is one of the most important and expensive components of the LIBs. The Li^+ ion mobility during charge/discharge process is regulated by the electrolyte characteristics (salt dissociation ability, viscosity, and liquid range). However, the amount of electrolyte in the cell should be carefully dosed to avoid "dead weight", which can diminish the gravimetric energy density [105]. Liquid aqueous electrolytes, employed in other batteries, like lead-acid, are very safe and non-flammable, but they have very narrow operating potential (~1.2 V), which is too scarce to offer high energy densities. Therefore, the development of nonaqueous electrolytes for Li-ion batteries started as early as in 1950s. The ideal electrolyte for lithium-ion battery should possess wide electrochemical stability window to avoid its continuous decomposition upon redox reactions and good ionic transport properties. Furthermore, it should provide electronic separation of the electrodes to avoid short-circuits and be chemically and electrochemically inert towards other battery components (e.g., packaging). Typical electrolyte for lithium-ion battery consists of a mixture of organic, aprotic solvents, in which a conducting salt is dissociated. To tilt the properties of the electrolyte (i.e., composition of the formed SEI or flame retardancy) additional components (salts, organic compounds or solvents) are included in relatively small amounts (typically below 5 wt%) in the electrolyte. As discussed above, the

combination of lithium metal with liquid electrolyte results in the growth of dendrites, which can be lowered by the use of solid polymer electrolytes, consisting of a high molecular weight polymer matrix, in which a lithium salt is dissociated. The detailed description of the state-of-the-art electrolyte components, both liquid and solid polymer ones, will be presented in the following subchapters.

2.4.1.1   Solvents

The ideal electrolyte solvent should have a high dielectric constant ε to ensure salt dissociation, and should also possess low viscosity η to enhance the ionic conductivity σ and wettability of the porous electrodes. Furthermore, its melting point T_m should be low, whereas its boiling point T_b should be high, so that the solvent remains liquid in a wide temperature range [106]. Finally, the ideal solvent should be cheap, non-toxic and non-flammable.

State-of-the-art electrolytes generally present a mixture of cyclic and linear aliphatic aprotic (as protic solvents are not stable at low potentials [105]) solvents. While cyclic carbonates offer high dielectric constants ($\varepsilon_{EC} > \varepsilon_{water} \sim 79$ [107]), assuring the dissociation of the conducting salt, they possess relatively high T_m, reducing the electrolyte liquid range and increasing its viscosity. On the other hand, linear or acyclic carbonates have low T_b, low dielectric constant and low viscosity, thus offering higher conductivity. Besides the abovementioned differences, cyclic and linear carbonates also show differences in electrochemical and thermal stability [106]. Therefore, the combination of both solvents results in the mixture with the balanced properties.

Propylene carbonate (PC) was one of the first esters to be employed in Li-ion batteries even before the commonly used ethylene carbonate [108]. This solvent has very low T_m, which is highly desirable for low-temperature applications, and a high dielectric constant. Nevertheless, its practical use with graphite anodes is hindered by its inability to form a stable passive layer [109]. Upon graphite lithiation in a PC-containing electrolyte the continuous solvent decomposition in graphite crevices occurs accompanied by the formation of propylene gas [110]. Furthermore, PC co-intercalates in between the graphene sheets, causing the exfoliation of the layers [50]. Overall, this results in a strongly decreased reversibility of the Li$^+$ intercalation process and fast loss of cell capacity. However, mixtures of PC with other carbonates [111], or coating of the graphite material with a thin carbon layer, which is further discussed in Section 2.3.3.2, allows the stable cycling of graphitic anodes.

Ethylene carbonate (EC) is a state-of-the-art electrolyte solvent with similar structure (only methyl group is absent) and physico-chemical properties of PC. It is worth mentioning that after

almost 4 unsuccessful decades of PC-containing electrolytes utilization, the introduction of EC catalyzed the fast development of the Li-ion technology as we know it today. Indeed, the main advantage of EC is its ability to form a stable SEI upon cathodic decomposition at 0.8 V *vs* Li/Li$^+$, protecting the anode surface from continuous decomposition [15]. Due to its high molecular symmetry, EC has a high T_m and remains solid at ambient temperature [112], but its use in combination with other solvents permits to overcome this problem.

Dimethyl carbonate (DMC) is a linear carbonate, which has a lower viscosity but higher volatility than EC. It is electrochemically unstable towards the graphite anode, which results in a large gas evolution and fast capacity decay [113]; thus, DMC is not used in a single-solvent electrolyte. On the other hand, mixtures of EC and DMC are widely used as they offer a well-balanced combination of the advantages of each solvent.

Fluoroethylene carbonate (FEC) is another cyclic carbonate, which is mostly used as an additive in the amount not exceeding 5 wt% [114, 115]. It seems to have a beneficial effect on both anode [116] and cathode materials [117]. In particular, FEC is at present emerging as an inevitable component of the electrolyte (in this case as a co-solvent in the amount of 10 wt%) to reach stable cycling of silicon anodes [118]. The decomposition mechanism of FEC is not completely clarified yet. Studying the silicon anode surface, Etacheri et al. [119] found that the decomposition of FEC on the silicon surface yields LiF and poly(VC), which further decomposes via radical polymerization (Figure 12a). Lucht and co-workers [120], on the other hand, introduced the de-fluorination mechanism via one-electron reduction with the formation of LiF and F loss radical (Figure 12b). Other groups, using experimental and computational methods, proposed alternative reaction pathways based on two-electron FEC decomposition and formation of LiF, CO_2 and vinoxyl, as shown in Figure 12c [121, 122].
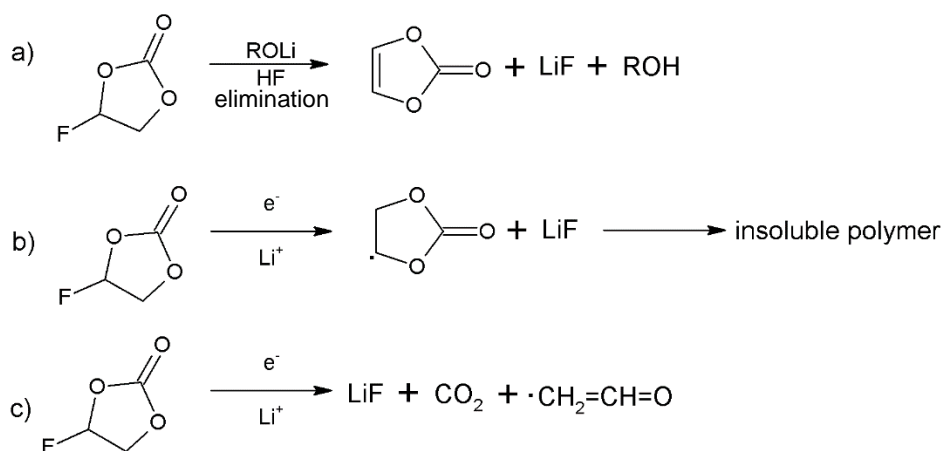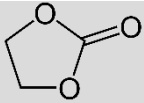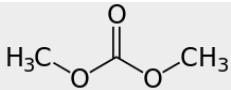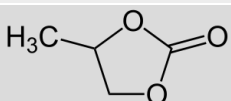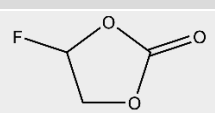

Figure 12. Possible decomposition routes of FEC (adapted from Ref. [119-121]).

Table 1 presents the summary of the physico-chemical and electrochemical properties of the solvents, used in the current work.

Table 1. Physico- and electrochemical properties of the selected cyclic and linear carbonates as electrolyte solvents (data taken from [6, 106]).

Solvent	Structure	Dielectric constant ε, 25 °C	Viscosity η, mPa s	T_m, °C	T_b, °C	Contribution to SEI
EC		89.78	1.90 (40 °C)	36.4	248	yes
DMC		3.107	0.59 (20 °C)	4.6	91	no
PC		64.92	2.53 (25 °C)	-48.8	242	no
FEC		~110	~3.5 (25 °C)	19-20	212	yes

2.4.1.2   *Conducting salts*

The available lithium conducting salts are quite limited due to the large number of requirements they have to fulfill. The salts should have a high dissociation constant and a high solubility even in low dielectric media, thermal and electrochemical stability, chemical inertness towards different cell components and non-toxicity [105, 106]. The challenge of finding a salt with high solubility is related to the small ionic radius of lithium ion, which hinders the dissolution of the halides (with Cl^- or F^- anions) in low polar media. Therefore, complex anions, comprising simple anion (i.e., F^-) and stabilizing Lewis acid (i.e., PF_5) have been successfully implemented as conducting salt anions. The structure of the Lewis acid, also known as superacid, permits the efficient delocalization of the negative charge due to its strong electron withdrawing properties. Thus, the resulting lithium hexafluorophosphate ($LiPF_6$) salt is soluble in EC/DMC unlike its parent salt LiF.

Other salts, such as lithium hexafluoroarsenate ($LiAsF_6$), lithium tetrafluoroborate ($LiBF_4$), or lithium perchlorate ($LiClO_4$) have been also investigated during the last decades. However, the high toxicity of $LiAsF_6$, the strong oxidative properties of Cl (VII), leading to explosion of practical batteries with $LiClO_4$, and moderate ionic conductivity and inability of a stable SEI formation in presence of $LiBF_4$ have prevented the commercialization of these salts. In turns, $LiPF_6$ offers a balanced combination of properties, such as good ionic conductivity, wide

electrochemical stability window and ability to passivate Al current collector. This is due to the reaction of salt anion with Al current collector and formation of AlF_3 and $Al_2(CO_3)_3$, which hinder the desorption of Al from the current collector [123]. Among the drawbacks related to the use of this salt, one can mention high sensitivity towards hydrolysis, resulting in release of toxic HF gas, and poor thermal stability (<70 °C).

Lithium imide salts, e.g., lithium bis(trifluoromethanesulfonyl)imide (LiTFSI), lithium bis(fluorosulfonyl)imide (LiFSI) or lithium (fluorosulfonyl)(trifluoromethanesulfonyl)imide (LiFTFSI), whose chemical structures are shown in Figure 13, have been proposed as alternatives to $LiPF_6$ due to their lower sensitivity to hydrolysis and their increased thermal and electrochemical stabilities [124-129]. However, being anodically more stable than $LiPF_6$, they are not able to form a protective layer on the surface of Al, leading to its anodic dissolution. This process, however, can be suppressed in presence of fluorinated solvents [130] or $LiPF_6$ as a co-salt [131].
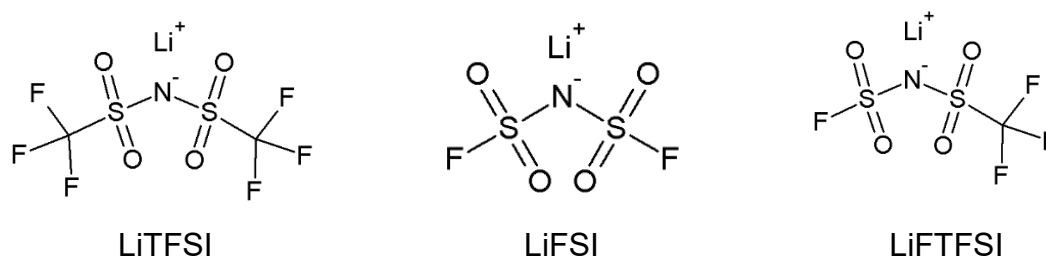

Figure 13. Chemical structures of the three imide Li salts.

2.4.1.3 *Electrolyte additives*

The additives in the electrolyte are used to facilitate the formation of the stable SEI on anode/cathode surface, protect cathode from overcharge or transition metal dissolution, increase the coulombic efficiency, reduce the gas generation, or improve the thermal stability, ionic conductivity, and wettability of the separator. Typically additives are categorized as SEI supporting, flame-retardant and overcharge protection additives. SEI supporting additives can be further divided in three groups: reduction-, reaction-type additives and SEI modifiers [132]. The reduction-type additives usually decompose prior to the electrolyte solvents and salt upon charge and participate in the SEI build-up. The reaction-type additives might not decompose on the electrode surface but they scavenge radical anions of the intermediate solvents decomposition products or combine with the final compounds. The SEI modifiers, such as tris(pentafluorophenyl)borane (TPFPB), are able to re-dissolve the inorganic SEI components (e.g., LiF, Li_2CO_3, Li_2O), which, although necessary for the stability of the SEI and prevention of its continuous growth, in high amounts generate high cell impedance.

Vinylene carbonate (VC) is a state-of-the-art reduction-type additive, and its beneficial effect on improving cycling performance, thermal stability, and on reduction of the irreversible capacity was reported for different Li-ion cell chemistries. According to the available literature [133], VC is reduced on the surface of the graphite material at ~0.9 V *vs* Li/Li$^+$ (thus, prior to EC), forming flexible films, consisting of poly(VC). The SEI formed in presence of VC effectively suppresses further electrolyte decomposition. In addition, reduced gas generation during formation and cycling was observed [133-135]. With respect to the positive electrodes, similar decomposition products as on the anode were found on the surface of layered oxide cathodes upon oxidation of VC [136, 137]. FEC, which was introduced in Section 2.4.1.1, is another reductive-type additive, which beneficially affects the cycling performance of both anode and cathode and is widely employed for the improved capacity retention of silicon-containing anodes.

Interestingly, the imide salts, briefly discussed in Section 2.4.1.2, were also considered as possible electrolyte additives. For example, Dahn et al. [138] investigated the combined use of LiTFSI and VC in different Li-ion cells by careful and precise measurement of the coulombic efficiency and end-point slippage rate. It was found that the addition of LiTFSI (2-4 wt%) did not have any impact on the cycle life, but rather on the reduction of the cell impedance (especially in combination with VC), and thus, on improving the rate capability and capacity retention at high rates. These authors also suggested that LiTFSI changed the electrode surface film composition, leading to a thinner but more protective film [126]. The same group reported that the combination of LiFSI with VC reduced the gas formation and the voltage drop at 60 °C [139]. However, presently it is not fully understood how low concentrations of LiTFSI salts in the electrolyte affect the SEI composition.

2.4.2 Solid polymer electrolytes

Lithium-polymer batteries (LPBs), comprising Li metal anode and polymer-salt complex, called solid polymer electrolyte (SPE), have gained significant attention among other types of Li batteries because of their high theoretical energy density due to the utilization of lithium metal and increased safety. Indeed, the risk of leakage of toxic and flammable components, affecting the conventional LIBs, is reduced if not completely eliminated in Li-polymer batteries. This, additionally, leads to a high thermal stability of the Li-metal batteries. As previously discussed, the SPE forms stable interface with lithium metal, significantly reducing the amount of the formed dendrites. Moreover, the SPE acts as a separator, leading to the possible cost reduction in the future (separator costs comprise up to 26% of total battery costs [5]). Furthermore, the high flexibility of battery components allows the production of batteries of

different forms and shapes. The main drawback of SPEs is their low ionic conductivity at ambient temperature (10^{-6}-10^{-5} S cm^{-1}), which until now, has hindered the mass production of LPBs. However, the remarkable example of Bolloré [140], which uses all-solid-state polymer batteries for their 3000 Bluecars, gives hope for the future use of such batteries in the automotive field. These LPBs operate over the wide temperature range of -20 to +60 °C with an internal operating temperature of +60 to +80 °C [141].

State-of-the-art solid polymer electrolytes typically contain poly(ethylene oxide) polymer as it possesses strong solvating ability for various lithium salts via the interaction between Li$^+$ and the ether oxygens [142, 143]. Lithium-ion transfer in PEO is closely related to the segmental motion of the polymer chains [144], occurring in the amorphous region of the polymer (above T_m = 60 °C), determining the limited ionic conductivity of the polymer-containing SPEs at ambient temperature.

The most common lithium salt used in the SPEs, is lithium bis(trifluoromethanesulfonyl)imide (LiTFSI), developed by the group of M. Armand [14] and briefly discussed in Section 2.4.1.2. The main advantage of this salt is a highly charge-delocalized anion of low lattice energy, which results in rapid salt dissociation. When mixed with PEO, the TFSI anion acts as a solid plasticizer, hindering crystallization of the polymer and providing charge carriers for the movement of Li$^+$ [145]. However, the conductivity of a solid polymer electrolyte is still below the 10^{-4} S cm^{-1} room-temperature threshold generally accepted for automotive applications.

One possibility to increasing the ionic conductivity of the solid polymer electrolytes is to use the so-called ionic liquids (ILs). ILs are low-temperature molten salts, consisting of ions only. Their low tendency to recrystallize is ensured by the weak interactions between large cation and charge-delocalized anion. ILs are considered as possible alternatives to the conventional organic-based electrolytes because of their negligible vapor pressure, high ionic conductivities, high solubility of other (low-lattice-energy) salts and non-toxicity.

In this work, the ionic liquid, comprised of N-butyl-N-methyl pyrrolidinium cation (Pyr$_{14}^+$) and bis(trifluoromethanesulfonyl)imide (TFSI$^-$) anion was used (schematically shown in Figure 14). This ionic liquid is one of the most frequently used plasticizers for the solid polymer electrolyte. In particular, cross-linked ternary SPE with Pyr$_{14}$TFSI had high ionic conductivity even at room temperature and showed stable performance upon lithium stripping/plating test [146]. The conductivity improvement of the ternary electrolyte, compared to the binary PEO-LiX system, is related to the considerably increases the amount of the amorphizing anion [147]. de Vries et al. [148] compared Pyr$_{14}$TFSI with 7 other ionic liquids, comprising combinations of

pyrrolidinium cations and different anions, but no significant improvements in terms of ionic conductivity or lithium/SPE interface resistance were achieved.
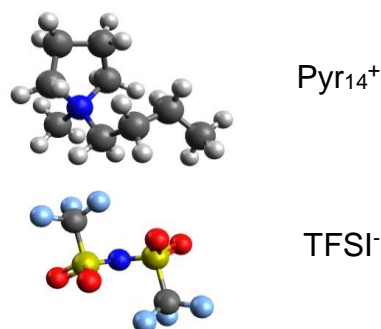

Pyr$_{14}^+$

TFSI$^-$

Figure 14. Structures of the ionic liquid components: pyrrolidinium cation and imide anion.

Inert fillers, mainly ceramics such as ferroelectric materials (BaTiO$_3$) [149], or oxides (Al$_2$O$_3$, TiO$_2$ or SiO$_2$) [144, 150, 151], have also been employed to increase the conductivity of the PEO-based electrolytes. These materials act as solid plasticizers hindering the crystallization of the polymer [150] and providing preferential pathways for Li$^+$ transport [151].

3. EXPERIMENTAL: MATERIALS, METHODS AND INSTRUMENTATION

3.1 Materials

For the study on solid polymer electrolytes (SPEs) poly(ethylene oxide) (PEO, M_w=250,000 g/mol, Sigma Aldrich) was dried under rotary vane pump vacuum at 50 °C for 48 h. The ionic liquid N-butyl-N-methyl pyrrolidinium bis(trifluoromethanesulfonyl)imide (Pyr$_{14}$TFSI, 99.9%, Solvionic) was dried under turbomolecular pump vacuum at 120 °C for 24 h. The water content in the ionic liquid after drying, determined by Karl Fischer titration (Mettler Toledo) was below 10 ppm. Silica (SiO_2, particle size <7 nm, Sigma Aldrich) was dried under rotary vane pump vacuum for 48 h at 170 °C. Benzophenone (for synthesis, ≥99.0%, Merck) was dried under rotary vane pump vacuum at 40 °C for 48 h. Lithium iron phosphate $LiFePO_4$ (LFP, particle size 10 µm, Süd Chemie) utilized as cathode active material in the study on SPEs was used as received. Conductive carbon (Ketjenblack EC-300J, AkzoNobel) was dried under rotary vane pump vacuum at 120 °C for 24 h.

Sucrose (VWR Chemicals, D(+) anhydrous), glucose (Sigma Aldrich, purity ≥99.0%), citric acid (CA, Sigma Aldrich, purity ≥99.5%), poly(acrylic acid) (PAA, Sigma Aldrich, average M_w~450,000), poly(vynil alcohol) (PVA, Sigma Aldrich, average M_w~130,000, purity ≥99.0% hydrolyzed), sodium carboxymethyl cellulose (CMC, average M_w~30,000, degree of substitution 0.9, Walocel), styrene butadiene rubber (SBR, ~50% of water solution), and conductive carbon (Super C45, Imerys) were used as received.

Commercial synthetic graphite, calendered graphite and LFP electrode tapes for the study on additives and formation step investigation were kindly provided by CEA-LITEN.

Ethylene carbonate (EC), dimethyl carbonate (DMC), propylene carbonate (PC), fluoroethylene carbonate (FEC), commercial electrolyte LP30 (1M $LiPF_6$ in EC:DMC (1:1, v/v)), obtained from UBE, as well as lithium hexafluorophosphate ($LiPF_6$, Sigma Aldrich) and vinylene carbonate (VC, Solvionic) were used as received. Lithium bis(trifluoromethanesulfonyl)imide LiTFSI (>99% battery grade, 3M), lithium bis(fluorosulfonyl)imide LiFSI and lithium fluorosulfonyl(trifluoromethanesulfonyl)imide LiFTFSI (both from Provisco CS Ltd.) were pre-dried under a rotary vane pump vacuum for 12 hours, followed by the drying under the turbomolecular pump vacuum (<10^{-7} mbar) for at least 20 h.

3.2   Synthesis of carbon-coated graphite

Carbon-coated graphite was synthesized using three different mixing methods. In Method 1 the precursor (sucrose) was first dissolved in ultra-pure water, followed by the addition of graphite, subsequent mixing for 8 h and finally solvent evaporation in the oven at 80 °C. In Method 2 the precursor and graphite powders were mixed in an agate mortar for 10 min prior to carbonization. In Method 3 both components were pre-mixed in ultra-pure water, and ball-milled (two periods of 45 min at 400 rpm, with 10 min rest step between), followed by the solvent evaporation in the oven at 80 °C. Next, each mixture was ground and carbonized at 500 °C for 4 h, following previous work [152]. The carbonized materials were then ground in mortar and used for the slurry preparation.

3.3   Electrodes preparation

LFP polymer cathode tapes were prepared following the procedure described in [153]. First, the LFP powder (43 wt%) was thoroughly mixed with conductive carbon (7 wt%) in agate mortar. Then PEO (22 wt%), LiTFSI (7 wt%) and $Pyr_{14}TFSI$ (21 wt%) were added to the mixture of powders to form the LFP polymer bulk blend. It was subsequently sealed under vacuum in a pouch bag, annealed at 100 °C for 12 h, hot-pressed at 100 °C and cold-calendered to obtain the films of 40-50 µm thick. Active material loading comprised 3.5-4.5 mg cm^{-2}.

The electrodes with pristine and carbon-coated graphite were prepared using the following procedure. First, CMC binder was dissolved in ultra-pure water (4% H_2O solution), followed by the addition of conductive agent (Super C45) and subsequent stirring for 2 h. Then the active material was introduced stepwise, and the stirring continued for additional 2 h before SBR was added. The dispersion was then mixed using a blade mixer (Dremel) for 10 min and casted on the 20 µm thick dendritic Cu foil (Schlenk). After casting the electrode tapes were dried in the oven at 80 °C for 12 h. The electrode disks with 12 mm in diameter were punched from the tape and finally dried under rotary vane pump vacuum for at least 4 h at 120 °C.

The graphite electrodes from CEA-LITEN comprising 95% of active material (average loading of 7-8 mg cm^{-2} or 2.75 mAh cm^{-2}) were calendered to obtain the porosity of 39%. The LFP electrodes from CEA-LITEN with 90% of active material and the loading of 17-18 mg cm^{-2} (~2.5 mAh cm^{-2}) were calendered to reach the porosity of 35%. The anode/cathode capacity ratio was set to 1.1.

The electrodes with Super C45/CMC ratio of 80/20, used for the electrochemical stability window test, were prepared using similar procedure and had an average loading of 4-5 mg cm^{-2}.

Table 2 summarizes the compositions of the electrodes, used in the current study.

Table 2. Summary of the compositions and loading of the used electrodes.

Electrode composition	Ratio of components	Solvent	Loading, mg cm^{-2}
Graphite/Super C45/CMC/SBR	95:1:2:2	Ultra-pure H$_2$O	7-8
CMC/Super C45	80:20		4-5
LFP/Super C65/PVdF	90.5	NMP	17-18
LFP/KJB/PEO/LiTFSI/Pyr$_{14}$TFSI	43:7:22:7:21	-	3.5-4.5

3.4   Electrolytes preparation

Three different solid polymer electrolytes (SPEs), A: PEO$_{20}$-LiTFSI + 10 wt%$_{PEO}$ SiO$_2$, B: PEO$_{20}$-LiTFSI-(Pyr$_{14}$TFSI)$_2$, and C: PEO$_{20}$-LiTFSI-(Pyr$_{14}$TFSI)$_2$ + 10 wt%$_{PEO}$ SiO$_2$, were prepared in the dry room (dew point <-60 °C), following a similar procedure to the one reported in [154]. The molar ratio of PEO:LiTFSI was fixed to 20:1. In the sample with the ionic liquid the ratio of LiTFSI:Pyr$_{14}$TFSI was set to 1:2. SiO$_2$ and benzophenone weights were calculated based on the weight of PEO. For electrolytes A and C, PEO was first pre-mixed with silica in an agate mortar. For the electrolytes B and C benzophenone was first dissolved in the ionic liquid. Next, all components were hand-mixed together until the formation of the bulk material. Then each electrolyte was placed in a pouch bag, sealed under vacuum and annealed at 100 °C for 12 h. Small pieces of each electrolyte were then sandwiched between two Mylar foils (PPI) and subsequently hot-pressed (Servitec Polystat 200T) at 100 °C to obtain the films with the thickness below 100 µm. The electrolytes, comprising ionic liquid (B and C) were then cross-linked in a UV chamber (Uvacube 100) for 6 min [146].

All liquid electrolytes were prepared by mixing the components (solvents, salts and additives) and stirring them inside the Ar-filled glove-box (water and air content <0.1 ppm) for at least 12 h prior to use.

The electrolyte compositions and preparation methods are summarized in Table 3.

Table 3. Summary of the electrolyte compositions and their preparation methods.

Salt	Solution	Additive	Preparation method
1M LiTFSI		10 wt%$_{PEO}$ SiO$_2$	Annealing→hot-pressing
1M LiTFSI, 2M Pyr$_{14}$TFSI	20M PEO	5 wt%$_{PEO}$ Benzophenon	Annealing→hot-pressing→UV irradiation
1M LiTFSI, 2M Pyr$_{14}$TFSI		10 wt%$_{PEO}$ SiO$_2$, 5 wt%$_{PEO}$ Benzophenon	
1M LiPF$_6$	EC:DMC (1:1)	-	Commercial
		2 wt% VC	
		2 wt% FEC	Mixing on a magnetic plate for 12 h
		2 wt% LiTFSI	
		2 wt% LiFSI	
		2 wt% LiFTFSI	
	EC:DMC:PC (1:3:1)		
0.9M LiPF$_6$, 0.1M LiTFSI		-	
0.8M LiPF$_6$, 0.2M LiTFSI	EC:DMC (1:1)		
0.7M LiPF$_6$, 0.3M LiTFSI			

3.5 Cell assembly

The assembly of the pouch cells was always conducted in the dry room. The pouch cells, used for the conductivity tests were assembled by placing the piece of SPE (area 3-4 cm²) between two Cu current collectors (50 µm, Schlenk). For the time evolution of impedance, limiting current and lithium stripping-plating tests symmetrical Li/SPE/Li cells comprising SPEs placed between two lithium foils (50 µm, Rockwood Lithium) were assembled. Full-cell galvanostatic cycling tests were conducted on pouch cells consisting of LFP polymer cathode disk (area 1.13 cm²), SPE and Li foil as counter electrode. For the pouch cells, used for the formation step investigation, the electrodes with the area of 16 cm² were used. As the electrodes, provided by CEA-LITEN, were double-coated, they required preliminary washing. Therefore, the anode and cathode tapes were cleaned with water or NMP, respectively, and dried at 80 °C for at least 1 h. The anode and cathode tabs were then ultrasonically welded (ULTRASONIC weldsolutions) with Ni or Al current collectors, respectively. Celgard 2325 was employed as a separator. The electrolyte (1.2 mL) was inserted as a blister inside the cell prior to its vacuum sealing and opened applying the external pressure after the cell was hermetically closed.

Two-electrode coin cells (type 2032), which were used for the galvanostatic cycling both in half and full cell configurations with pristine and carbon-coated graphite as well as LFP, were assembled by sandwiching the anode and cathode disks (area 1.13 cm²) with a glass fiber separator (Whatman GF/D, GE Healthcare) in between. In case of half-cell configuration, Li metal disk (1.53 cm², 0.5 mm thick, Rockwood Lithium) was used as a counter electrode. The amount of electrolyte per cell was 100 µL.

For several measurements, including cyclic voltammetry (CV) and electrochemical stability window test (ESW) via Linear Sweep Voltammetry (LSV), three-electrode Swagelok-type T-cells were used. In these cells Li was used as a counter and a reference electrode. For the CV test, the pristine or coated graphite working electrodes were used. Pt (0.0078 cm^2) or carbon electrode (Super C45/CMC=80/20, 1.13 cm²) served as working electrodes for the ESW measurements. The same glass fiber separator was used, while the amount of electrolyte injected in the cell comprised 120 µL.

The electrochemical impedance spectroscopy (EIS) measurements for study on the additives and formation step were realized using the three-electrode EL-cells (type ECC-PAT-Core, EL-CELL). The assembly of the EL-cell is schematically shown in Figure 15. A negative electrode (graphite electrode 18 mm in diameter) was inserted into the insulation sleeve with the pre-assembled Li-reference ring and the glass-fiber separator (Whatman GF/A), followed by the lower plunger. A positive electrode (LFP or Li disk) was placed on the other side of the insulation sleeve after the electrolyte injection (130 µL), followed by the upper plunger. The insulation sleeve was placed into the EL-cell base. The PE-seal was mounted on top, followed by the lid with integrated spring. Subsequently, the cell was placed inside the bracket and closed with the wing nut. Finally, the feed wire assy was screwed to connect with the reference.
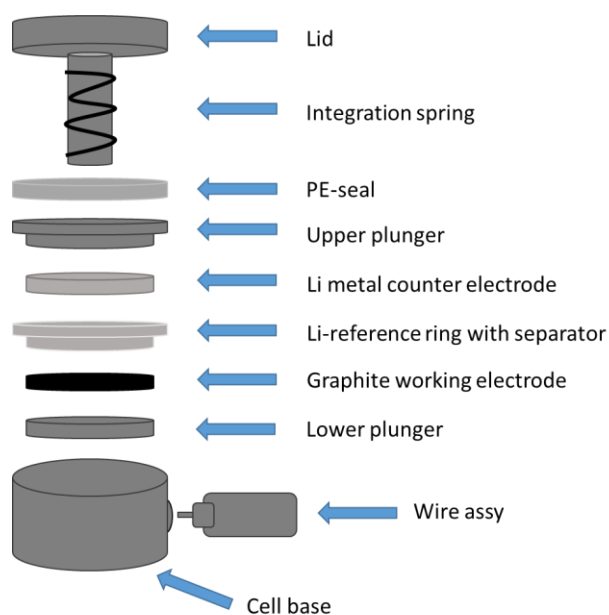
Figure 15. Schematic of the EL-cell assembly.

3.6   Electrochemical methods

3.6.1   Chronopotentiometry

Chronopotentiometry refers to the electrochemical technique, in which typically a constant current is applied between the working and counter electrodes, and the potential of a working electrode is monitored with respect to the reference electrode as a function of time.

In the constant current chronopotentiometry, the applied cathodic/anodic current causes the electroactive species to get oxidized/reduced at a constant rate, following the electron transfer reaction:

$$O + ne^- \leftrightarrow R \qquad\qquad (3.1)$$

The potential upon reduction/oxidation process can be determined using the Nernst equation:

$$E = E^0 + \frac{RT}{nF} \ln\left(\frac{C_O}{C_R}\right), \qquad (3.2)$$

where E is the electrode potential (V), E^0 is the redox potential for the redox couple O/R (V), R is the gas constant (R=8.315 J K^{-1} mol^{-1}), T is the temperature (K), n is the number of electrons transferred during the redox reaction, F is the Faraday constant (F=96,485 C mol^{-1}), and C_O or C_R are the concentrations of the oxidized or reduced species (mol L^{-1}), respectively. The concentrations C_O and C_R change with time, and so changes the potential. The time τ required for electroactive species to get fully reduced/oxidized on the surface of the electrode in a chronopotentiometric test depends on the applied current and can be expressed using the Sand equation:

$$i\tau^{1/2} = \frac{nFAC\pi^{1/2}D^{1/2}}{2}, \qquad (3.3)$$

where D is the diffusion coefficient of the reactant (cm² s^{-1}), C is the initial concentration of the reactant (mol cm^{-3}), A is the electrode area (cm²).

The applied current can also be varied (linearly decreased or increased) with time or even reversed when the certain potential is reached. The latter technique is often used in battery tests and is called galvanostatic cycling.

3.6.1.1   Galvanostatic cycling

Galvanostatic cycling is used to estimate the battery's specific capacity and cycling stability. The voltage profile, obtained in this measurement is used to characterize the multistep redox reactions upon the insertion of lithium ions into the electrode host structure. Depending on the shape of the voltage profile it is possible to distinguish two types of the reactions. When the potential varies continuously, this reaction type is called a solid solution. On the contrary, the appearance of the plateaus at a constant potential upon time refers to the occurrence of multi-phase reactions.

The galvanostatic cycling tests were performed using the Maccor 4300 Battery Tester. The cycling of the full pouch cells, comprising Li/SPE/LFP cathode tape, was performed at 40 °C in the climatic chamber (Binder). After the thermal aging at 40 ±1 °C for 10 h, the cells were cycled using a current rate of C/20=8.5 mA g^{-1} in the first cycle, followed by long-term cycling at C/10. The cut-off voltages were set between 4.0 and 2.0 V.

The half and full coin cells were first stored at 20 or 40 ±1 °C for 16 or 24 h, respectively. The protocols for cycling of half Li/graphite (also applies for Li/carbon-coated graphite), Li/LFP and full graphite/LFP cells can be found in Table A2b,c of APPENDIX 1. For the half and full cells used for the study on formation step, the protocols are described in Sections 4.3.1. The cycling rate of 1C for graphite and LFP corresponds to 372 and 170 mA g^{-1}, respectively. The cut-off voltages were fixed between 1.0 and 0.01 V for graphite and between 3.65 and 2.5 V for LFP. The same theoretical current density of 170 mA g^{-1} was used for the full graphite/LFP cells, thus determining the cells as cathode-limited with the cut-off voltage fixed between 3.6 and 2.5 V. The delivered capacity for carbon-coated materials was calculated based only on the graphite loading through the subtraction the amount of carbon in coating, determined by TGA. The cycling of upscaled pouch cells, comprising graphite and LFP electrodes (area 16 cm²) was done in several steps. First, the cells were aged for 24 h at 40 °C, followed by one cycle at C/20. After the initial charge/discharge the cycling was suspended and the cells were subjected to impedance measurement. Then the cells were cycled at C/10 for 5 additional cycles, followed

by another impedance measurement. Subsequently, the cycling was resumed, using current density, corresponding to 1C. The impedance measurements were repeated after 106, 506 and 1006 cycles.

To avoid possible misunderstanding when referring to charge/discharge processes in half Li/graphite cells, "charge" is the process of cathodic reaction at the anode (lithium intercalation into graphite). Accordingly, the opposite process is denoted as "discharge".

3.6.1.2 Li stripping-plating test

The polarization experiment (lithium stripping-plating test) can be used as a reliable indicator of the effectiveness of the lithium deposition process as well as the stability of the passive layer at the Li/SPE interface upon long-term cycling under DC conditions. The stability of the interface is linked to the high reactivity of the freshly deposited lithium, which is readily participating in decomposition reactions, leading to the formation of the passivation film on its surface and lithium consumption [148]. Such experiments are usually conducted in galvanostatic conditions reversing the current flow after a certain time and recording the overvoltage. While the evolution of the overvoltage can be used to track the change in the passive layer, the total number of cycles is limited by the irreversible lithium loss and possible short-circuits due to the dendrite growth.

In the current work symmetrical Li/SPE/Li cells were first thermally equilibrated at 40 $\pm$1 °C for 12 h. Subsequently, the current of $\pm$0.078 mA cm^{-2} was applied and reversed every hour, and the resulting overvoltage was measured.

3.6.2 Linear sweep and cyclic voltammetry

Both voltammetry techniques are generally used to study the processes in the electrodes by varying the potential with a certain scanning rate (V s^{-1}) to the working electrode and recording the faradaic current (reactions on the electrode) with a capacitive contribution (double layer charging upon potential sweep). In the linear sweep voltammetry (LVS) test the potential is swept only in one direction (either towards reduction or oxidation), whereas in the cyclic voltammetry (CV) test the sweep direction is inverted after reaching a specific potential (known as switching potential).

CV can provide the information about the thermodynamics and kinetics of the electrode reactions, as well as mass transport. In this experiment the potential sweep initiates the electrode-electrolyte reaction, leading to a current increase in the solution-based system. Further sweep leads to the formation of a concentration gradient and the consumption of the electroactive species. After the maximum current (peak current) is reached, the current

decreases due to the depletion of the electroactive species. Reversing the sweep potential leads to the appearance of a similar peak for the inverted reaction. Combining Fick's first law and Faraday's law the peak current can be determined, using Randles-Sevchik equation:

$$i_p = 0.4463nFAC\sqrt{\frac{nFvD}{RT}}, \qquad (3.4)$$

where i_p is the peak current (A), and v is the scan rate (V/s). As follows from Equation 3.4 the peak current is proportional to $v^{1/2}$. If upon the change of the scan rate the position of the peak maxima does not change, such system is called reversible. If the potential of the peak maxima shifts with the variation of the scan rate, such system is called irreversible.

Li-ion batteries present more complicated systems that the solution-based ones. The ideally reversible behavior in LIBs is rarely observed due to the kinetic limitations and reactions of the electrode material upon the transport of Li ions into and out of the electrode. Still, CV is widely used to study the redox and surface reactions in Li-ion batteries.

In this work CV tests were conducted to analyze the cyclability of the pristine and carbon-coated graphite materials in propylene carbonate (PC) electrolytes. Three-electrode Swagelock cells with Li as a reference and counter electrode were tested by means of VMP-3 potentiostat (BioLogic Science Instruments). Whatman GF/D separator was soaked with either 1M $LiPF_6$ in PC:DMC (1/1, w/w) or 1M $LiPF_6$ in EC:DMC:PC (1/3/1, w/w/w). The measurements were performed with a scan rate of 0.1 mV s^{-1} between 0.01 and 1.0 V vs Li/Li$^+$ for 10 cycles.

LSV is similar to CV technique, but instead of reversing the current when the switching potential is reached, the measurement is stopped. In this work LSV was used to measure the electrochemical stability window (ESW) of the liquid electrolytes. The ESW represents the voltage range in which the electrolyte does not undergo reductive or oxidative decomposition. Therefore, it is calculated by subtracting the reduction (cathodic limit) potential from the oxidation (anodic limit) potential of the studied substance. The scan begins at the equilibrium state (open circuit voltage, or OCV), when no current is flowing. When the certain voltage, above/below (for anodic and cathodic sweeps, respectively) which the electrolyte components are not stable is reached, the electrolyte decomposition is initiated, resulting in the faradaic reactions. The voltage, corresponding to a current density value below ± 0.1 mA cm^{-2} is generally used to define the stability boundaries of the electrolyte [127]. The cells with Pt or carbon working electrodes were subjected to a LSV using the VMP-3 potentiostat from OCV to either -1.0 V or 6.0 V vs Li/Li$^+$, using a fresh cell for each cathodic or anodic scan, with a scanning rate of 0.1 mV s^{-1}.

Additionally, LSV was used to determine the limiting current density of the SPEs. This test is generally used to characterize the mobility of the electroactive species (Li ions in our case) at the Li/SPE interphase. For the measurements the symmetrical Li/SPE/Li pouch cells, were thermally equilibrated for 10 h at 40 $\pm$1 °C. LSV tests using the VMP3 potentiostat were conducted in the voltage range of 0.00 – 0.75 V *vs* Li/Li$^+$ with the scan rate of 0.01 mV s^{-1}. The measurements were reproduced on a few cells for each electrolyte.

3.6.3   *Electrochemical impedance spectroscopy*

In the electrochemical impedance spectroscopy (EIS) a small sinusoidal perturbation (current or potential) is applied to the system, and the sinusoidal (pseudo-linear) response is obtained, which is deviating from the applied signal in phase and amplitude. The technique allows analysis of the processes in the electrodes, including the contributions from kinetics, double layer, diffusion, etc.

The perturbation signal (potential) as a function of time, has a form stated in equation:

$$E_t = E_o \sin(\omega t) , \qquad\qquad (3.5)$$

where E_t is the potential at time t, E_o is the amplitude of the signal, and ω is the radial frequency ($\omega = 2\pi f$, f is the frequency in Hz) in rad/s.

The response will then have a different amplitude (I_o) with a shift in phase (ϕ) as in the equation:

$$I_t = I_o \sin(\omega t + \phi) \qquad\qquad (3.6)$$

Then the proportionality factor between the potential E_t and the current response I_t is the impedance. Following Ohm's Law (Resistance=Voltage/Current), the total impedance of the system can be expressed in the following way:

$$Z = \frac{E_t}{I_t} = \frac{E_o \sin(\omega t)}{I_o \sin(\omega t + \phi)} = Z_0 \frac{\sin(\omega t)}{\sin(\omega t + \phi)} \qquad (3.7)$$

It is also possible to express the impedance as a complex number, using the following equation:

$$Z(\omega) = Z_0 \exp(j\phi) = Z_0 (cos\phi + jsin\phi) \quad (3.8)$$

Impedance in equation (3.9) consists of a real and an imaginary part. If then the real part is plotted on *x*-axis, and imaginary on *y*-axis, the complex plot (Argand diagram or "Nyquist plot") in the form of a semicircle can be obtained, in which each point represents the impedance at one frequency (Figure 16a). Although in the electrochemical literature the name "Nyquist plot" is commonly used, it is not fully correct, as this plot only describes the stability of the system, which is providing feedback [155]. However, herein, for simplicity the complex plot will be designated as "Nyquist plot". One of the obvious limitations of Nyquist plots is the absence of

frequency values in the graph. Another way to represent the impedance graphically is to use "Bode Plot" (Figure 16b), in which frequency is plotted on *x*-axis, and both log of absolute impedance ($|Z| = Z_o$) and phase shift are plotted on *y*-axis.
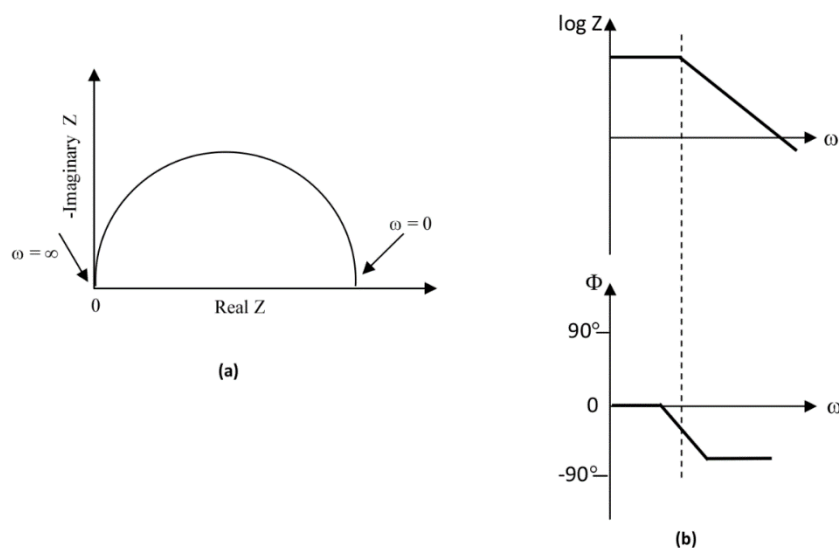

Figure 16. a) Nyquist and b) Bode plots (taken from Ref.[156], open access).

The EIS data is typically analyzed by comparing the experimental spectrum with the equivalent circuit model, which includes the use of common electrical circuit elements such as resistor R (Z=R), capacitor C (Z=1/jωC), and inductor L (Z= jωL). The latter one is seldom included in the equivalent circuit, as it can typically be observed at very high frequencies (> 1 MHz) above the resolution of the most instruments. Additionally, a special Warburg element is typically used to model the mass transfer processes ($Z= 1/Y_0\sqrt{j\omega}$).

The spectrum, appearing in the Nyquist plot in Figure 17b can be modelled using the so-called simplified Randles circuit in panel *a*. This circuit consists of a resistor, ascribed for the solution resistivity, connected in series with a R|C element, including charge transfer resistor (R_{ct}) and double layer capacitor (C_{dl}) in parallel. This circuit describes the flat metal electrode, immersed in a liquid electrolyte.

In the porous electrodes the diffusion processes take place on the electrode surface, resulting in the appearance of a straight line with 45° angle at low frequencies (panel *d*). The diffusion impedance appears only in a low-frequency range as at high frequencies the reactants would not move to the electrode surface from the bulk. In this case the additional Warburg element is added to Randles cell to model the spectrum (panel *c*). The combination of charge transfer and Warburg impedances is called faradaic impedance. If no faradaic reactions take place on the electrode, the double layer is getting charged, resulting in the appearance of straight line almost parallel to the imaginary axis at low frequencies. This behavior is then attributed to the blocking electrode. It should also be noted that a constant phase element (CPE) is often used in the model

instead of a capacitor or a Warburg element to compensate for the non-homogeneity in the investigated system.
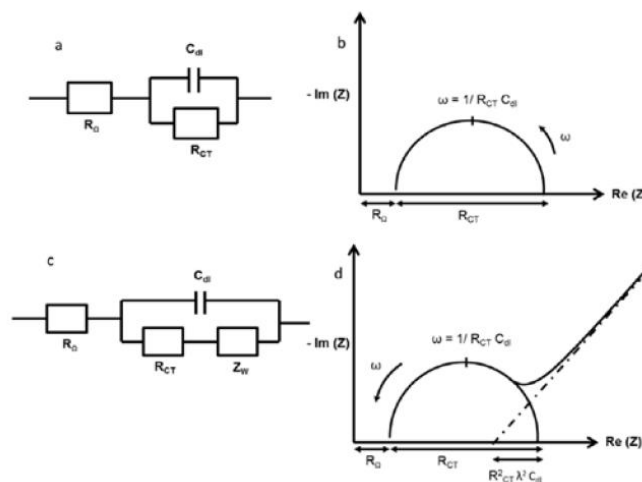

Figure 17. Nyquist plot and the equivalent circuit model (taken from Ref.[157], open access).

EIS is frequently used to characterize the changes at the interface between Li and solid polymer electrolyte under steady-state conditions. In this work symmetrical Li/SPE/Li cells comprising SPEs sandwiched between two lithium foils (50 µm, Rockwood Lithium) were assembled in vacuum-sealed pouch bag cells and stored in the dry room or in the climatic chamber for 20 ±1 °C and 40 ±1 °C tests, respectively. Time evolution of the cell impedance was recorded using the Impedance/Gain Phase Analyser 1260 (Solartron Analytics) with an AC amplitude of 10 mV in the frequency range of 100,000 – 1 Hz. The same procedure and the device were used for the EIS measurements on the full graphite/LFP pouch cells (16 cm²), suspending the cells after certain cycles.

Alternatively, EIS can also be used during cycling to monitor the impedance changes upon reactions occurring at the electrodes. In this work the changes in the impedance using organic electrolytes with different additives and different ratios between $LiPF_6$ and LiTFSI were investigated in three-electrode EL-Cells with graphite as working, and Li as counter and reference electrodes. The cell assembly procedure and scheme are described in detail in Section 3.5. The cells were subjected to a rest period (12 h at 20 °C) prior to cycling of the graphite electrode at a rate of C/20 (using a Modulab XM ECS potentiostat equipped with frequency response analyzer, BioLogic Science Instruments). The cycle was interrupted at different cell potentials (0.7, 0.5, and 0.01 V vs Li/Li$^+$ upon lithiation) and the cell was let to rest for 2 h at open circuit potential (OCP) prior to impedance measurements made using an AC amplitude of 5 mV in the frequency range of 10 kHz – 0.1 Hz. The same cell configuration and measurement set-up was used for the impedance measurements after the first charge and discharge in the full graphite/LFP cells with Li reference electrode using three different formation protocols. The

cycling and EIS measurements with lab standard and dual-current protocols were conducted at 20 °C, whereas for the industrial counterpart the temperature was increased to 40 °C after the initial pre-charge.

3.6.3.1 Conductivity determination using electrochemical impedance spectroscopy

One of the other possible applications of the EIS is the determination of the ionic conductivity of an ionic solution, which was used in this work for the liquid and solid electrolytes. Ionic conductivity of the solution can be expressed using the equation:

$$\sigma = \frac{t}{R \cdot A},\qquad\qquad(3.9)$$

where σ is the ionic conductivity of the solution (S cm^{-1}), R is the measured ionic resistance of the solution in a steady-state condition, A is the active electrode area (cm^2), and t is the distance between two electrodes (thickness of the electrolyte for SPEs, cm). The values A and t are depending on the electrolyte and cell setup and define the cell constant k, used for the measurement, whereas R (same as R_Ω) can be determined by fitting the intercept of the Nyquist plot with real axis at high frequency.

For the liquid electrolytes the temperature dependence of conductivity was measured by the means of an automated conductimeter equipped with a frequency response analyzer and a thermostatic chamber (Materials Mates and BioLogic Science Instruments). Each sample was injected in the specifically designed air-tight conductivity cell with two platinum electrodes. The cell constant was determined using a 0.01M KCl standard solution (1.41 mS cm^{-1}). The ionic conductivity was then measured as a function of temperature applying a 5 °C h^{-1} step and stabilizing the cell at each temperature (from +5 to +55 °C) for 1 h.

To measure the conductivity of the solid polymer electrolytes each membrane (area 3-4 cm^2) was sandwiched between two Cu current collectors (50 µm, Schlenk), placed in the pouch cell and closed after applying vacuum in the dry room (relative humidity below 0.1%). The cells were then thermally equilibrated in the climatic chamber (KB 23, Binder) for at least 8 h at each temperature (from +20 to +80 °C). Impedance measurements were conducted using the Impedance/Gain Phase Analyser 1260 (Solartron Analytics) with an AC amplitude of 10 mV in the frequency range of 100,000 – 0.1 Hz.

3.7 Thermal analysis

Thermal analysis (TA) is a branch of material science techniques, in which the properties of the materials are studied upon the temperature change. Among the most commonly used techniques are thermal gravimetric analysis (TGA) and differential scanning calorimetry (DSC).

TGA is a technique, in which the sample is thermally treated (heated up or cooled down) with a specific temperature scanning rate (K/min), depending on the desired resolution of the transition. The change in the sample's weight is monitored as a function of temperature increase. Upon the measurement the sample environment is controlled by the purge gas. While the air or oxygen are often used to simulate the sample burning (to trace water/solvent impurities, quantify the oxidative mass losses/gains or carbon residue during combustion), the heating in inert gas (i.e., nitrogen), or pyrolysis, gives a representation of the sample decomposition rate during this reaction.

Discovery TGA (TA Instruments) was used to conduct the measurements, presented in this thesis. For the analysis of the carbon content in the coated graphite the samples were placed in the open alumina pans and thermally equilibrated at 40 °C for 30 min, followed by the heating to 800 °C at a rate of 5 °C/min under oxygen flow. To determine the thermal stability of the SPEs the samples were placed in sealed Al pans, which were opened by the TGA device right before the experiment. The isothermal step described above was followed by the heating in oxygen atmosphere with a 10 K min^{-1} heating rate up to 600 °C.

DSC is another thermal technique, in which the difference in the heat flow into and from a sample and a reference (usually an empty Al pan) is measured as a function of temperature, which is changing at a constant rate. Since the measurement is conducted at a constant pressure, the heat flow is equal to the change of enthalpy. The measurement provides the qualitative and quantitative data on the endothermic (heat adsorbed) and exothermic (heat released) processes. These processes can include, for example, glass transition temperature, melting point, heat of fusion, crystalline phase transition temperature, specific heat or heat capacity. The schematic DSC curve in Figure 18 shows the shapes, associated with the possible phase transitions.
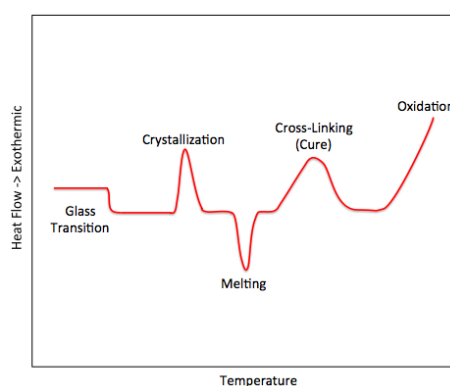
Figure 18. A schematic DSC curve with the shapes of possible phase transitions (taken from Ref. [158]).

In the present work Discovery DSC (TA Instruments) was used to perform the measurements. Thermal stability of the SEI using different electrolyte additives, was investigated using the electrodes from Li/graphite coin cells (type 2032). The graphite electrodes were subjected to a

single lithiation at C/20 down to 0.01 V. The cells were then carefully disassembled in the glove-box (water and oxygen contents below 0.1 ppm). The lithiated graphite (Li_xC_6) powders, obtained by scratching the material from the current collectors, were directly placed in hermetic, high-pressure DSC pans.

In the study of solid polymer electrolytes DSC was used to track the changes in glass-transition and melting points of the electrolytes when a ceramic filler, an ionic liquid, or both components were present. Each sample in a sealed Al pan was thermally equilibrated at 40 °C for 30 min, followed by cooling to -140 °C (rate: 45 K min^{-1}) from where the heating step to +140 °C (rate: 10 K min^{-1}) started. The reverse cooling step was performed after the sample was stabilized for 5 min at switching temperature. This heating-cooling cycle was repeated three times.

3.8   Brunauer-Emmett-Teller surface area analysis

The Brunauer-Emmett-Teller (BET) surface area analysis is based on the adsorption principle, which describes the possibility of atoms or molecules of gas to adhere to a surface. The amount of the adsorbed gas depends not only on the surface area of the solid, but also on the gas pressure, temperature and interaction strength between solid and gas. In typical BET measurement samples are placed in the glass cells for the degassing to remove the traces of water and other impurities before the actual measurement of the surface area can start. After the degassing, whose duration and temperature depend on the properties of the material, the sample is moved to the analysis port. Nitrogen is usually used as the gas to be adsorbed, as it is widely available in highly pure state and interacts with most of the solids. As the interactions between gas and solid are weak, the surface of the sample is cooled using liquid N_2. This results in the detectable by the instrument amounts of adsorbed gas. In the next step the known amount of nitrogen is stepwise released into a glass cell. The relative pressure less than atmospheric is then achieved by creating the conditions of the partial vacuum. When the saturation pressure (pressure of the vapor, which is in equilibrium with its liquid) is achieved, no more gas can enter the solid. After the formation of the adsorption layers is completed, the nitrogen flow is stopped, and the sample is heated up. During this step nitrogen is released from the sample and its amount is quantified. The analysis data is graphically depicted in the form of isotherm with the amount of adsorbed and desorbed gas as a function of relative pressure, as shown in Figure 19 below.
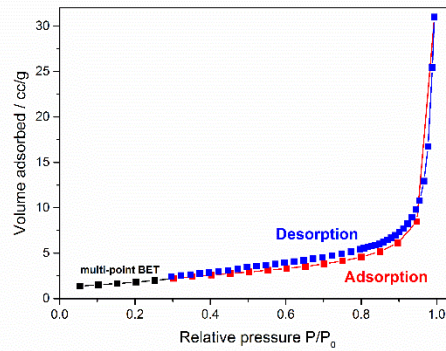
Figure 19. Isotherm of the commercial synthetic graphite.

To determine the surface area using multi-point BET, 3-5 data points in the range between 0.025 and 0.3 of relative pressure (P/P$_0$) of the isotherm are typically used. The total surface area can be then calculated, using the following formula:

$$S = \frac{X_m L_{av} A_m}{M_v},$$ (3.10)

where L_{av} is the Avogadro number (L_{av}= 6.022140857×10^{23} mol^{-1}), A_m is the cross-sectional area of the adsorbate (A_m=0.162 nm²), M_v is the molar volume (M_v=22414 mL mol^{-1}), and X_m is the monolayer capacity (volume of adsorbed gas at standard pressure and temperature).

Additionally, when the saturation pressure (P/P$_0$~1) is approached, the total pore volume can be identified, assuming that the density of the bulk nitrogen is the same as in the pores of the investigated material. Furthermore, using the desorption curve and applying Barrett-Joiner-Halenda (BJH) theory the determination of the pore size is possible.

In this work BET method using Autosorb-iQ (Quantachrome) was employed to determine the surface area of the pristine and carbon-coated graphite materials. Prior to the measurement the samples were degassed for 16 h at 200 °C.

3.9 X-ray photoelectron spectroscopy

X-ray photoelectron spectroscopy (XPS) is one of the most commonly used techniques to study the surface of a solid non-volatile sample (1-12 nm). XPS provide the information about the elemental composition and chemical or electronic state of each element. Furthermore, the uniformity of composition across the top surface of the solid materials can be characterized. XPS spectra can be obtained by irradiating the surface of the sample with the monoenergetic beam of X-ray photons (Mg-Kα or Al-Kα). As the surface atom is not surrounded by other atoms on all sides, it has a higher bonding potential and is, therefore, more reactive than the atom in the bulk of the material. Since photons represent mass- and chargeless energy packages,

their annihilation with electrons on the surface of solid will lead to the energy transfer. The energy is defined by Einstein relation

$$E = h\upsilon, \tag{3.11}$$

where h is the Plank constant ($h = 6.62\cdot10^{-34}$ J s) and υ is the radiation frequency (Hz). If this energy is enough, the photoelectron will be emitted from the solid. It should be noted that Auger electrons are also emitted from the sample and observed in XPS spectra. Both photoelectron emission and subsequent Auger de-excitation processes are schematically presented in Figure 20.
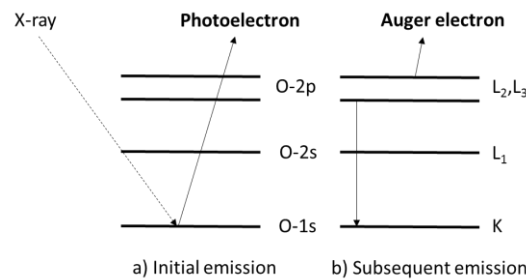
Figure 20. Scheme of a) photoelectron and b) Auger de-excitation processes.

The kinetic energy (KE_{ph}) of the emitted electron can then be measured and used to calculate the binding energy (BE), which is the element-specific energy needed to remove the electron from the surface, according to the following photoelectric equation:

$$KE_{ph} = h\upsilon - \phi - BE, \tag{3.12}$$

where ϕ is the work function of the instrument (represents the minimum energy required to remove the electron from the device). The energies of the Auger electrons are not directly related to the incoming photon energy but rather represent the difference between the energy levels after the electron perturbation has occurred, following the equation:

$$KE_{Aug} = E(K) - E(L_2) - E(L_3) \tag{3.13}$$

Therefore, the change in the energy of the X-ray beam would give different values of Auger electron energies and a subsequent shift along the BE scale, which is useful when the peak assignment is complicated.

When analyzing the spectra from p, d and f core levels, it is important to note that these orbits give a rise to a doublet with two possible states and different values of binding energies in the XPS spectrum. This effect is commonly referred as spin-orbit splitting and is expressed using the equation:

$$j = l + s, \tag{3.14}$$

where l is the angular momentum quantum number, s is the spin angular momentum number ($s =\pm\frac{1}{2}$), and j is the possible state. If, for example, $l =1$ as for 2p spectra, then j will be 1/2 or 3/2. Then the area ratio between $2p_{1/2}$ and $2p_{3/2}$ would be 1:2, which corresponds to 2 and 4 electrons at each level, respectively.

Except for hydrogen and helium, all elements can be identified via the determination of their binding energy. Furthermore, the binding energy of the electron does not only depend on the electron's level, but also on the formal oxidation state of an atom and the local environment. Therefore, the atom with a higher positive oxidation state would have a higher binding energy, also known as "chemical shift", related to the extra coulombic interactions between the photoelectron and the atom's core.

Angle-resolved XPS allows the variation of the emission angle, thus enabling the detection of the electrons from different depths (see the set-ups in Figure 21). This can be achieved by tilting the sample to limit the angular acceptance of the detector. In the field of batteries XPS is commonly used to identify the components of the passive film, formed on the surface of the anode or cathode during the first (or initial few) cycles. Depth profiling is conducted using an ion beam of a neutral gas (i.e., Ar) to etch the surface layers. Combination of ion sputtering with XPS can give the information about the composition of the subsurface layers and the layer thickness. The sputter yield depends on many factors, including the material itself, ion energy, the mass and nature of the primary ion and the incidence angle.
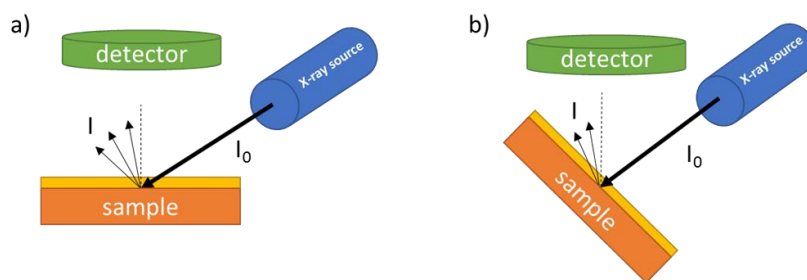
Figure 21. Scheme of a) conventional and b) angle-resolved XPS set-ups.

To analyze the SEI composition formed in presence of different electrolyte additives, Li/graphite half cells were subjected to one lithiation-delithiation cycle as described in Table A2a (APPENDIX 1). To investigate the SEI evolution upon cycling, some cells were exposed to additional 50 cycles at C/2, also including the constant voltage step in the fully lithiated state. For the study on the formation step full graphite/LFP cells were charged, following the procedure in Table A2c (APPENDIX 1). After cycling the cells were disassembled in the glove-box. The extracted graphite electrodes were carefully rinsed with 200 µL of DMC and dried in vacuum. The electrodes were then placed in an airtight vessel and transferred to the XPS sample

chamber. The measurements were performed using a PHI 5800 MultiTechnique ESCA System with monochromatized Al-Kα (1486.6 eV) radiation. The detection angle of the measurement was 45° and pass energies of 93.9 and 29.35 eV were used for survey and detailed spectra, respectively. XPS spectra were also collected after sputtering the electrodes for 3 and 10 min. The binding energies were calibrated to the C1s signal of graphite at 284.6 eV and analyzed using CasaXPS software.

3.10 X-ray diffraction

X-ray diffraction (XRD) is a commonly used technique to determine the structure and purity of the crystalline materials. The main components of the X-ray diffractometers include an X-ray tube, a sample holder and an X-ray detector. X-rays are generated when the electrons emitted from the heated cathode filament and accelerated by applying high voltage collide with the anode made from a metal of high purity (i.e., Cu or Mo). The X-rays are then monochromated, collimated and directed to the sample. The interactions between the X-ray beam and the atomic planes of the crystalline sample will produce the interferences, which can be destructive and constructive. Bragg's law defines the conditions, in which the constructive interferences occur, resulting in the diffraction event:

$$n\lambda = 2d\ sin\theta, \hspace{2cm} (3.15)$$

where n is the integer, λ is the wavelength of the electromagnetic radiation, θ is the diffraction angle, and d is the lattice spacing in the crystalline sample. The intensity of the diffracted X-rays is recorded and processed by the X-ray detector. The generated diffraction pattern (or a diffractogramm) then provides the information about the crystalline structure of the sample.

In this work XRD was used to determine the possible changes in crystallinity (or "amorphization") of the carbon-coated graphite materials. The diffractogramms were recorded in 2θ range between 15° and 80° using a Brucker D8 Advance ($\lambda_{Cu\ K\alpha}$=0.154 nm) diffractometer with a Bragg-Brentano geometry.

3.11 Scanning electron microscopy

Scanning electron microscopy (SEM) provides the information about the topography of the material by tracing its raster pattern. One of its main advantages is the possibility to obtain much higher resolution (few nanometers) compared, for example, to optical microscopy. In SEM the electrons are generated in vacuum by an electron gun, passed through a combination of lenses and apertures and focused onto a sample. When the beam hits the sample, the electrons and X-rays are released from it and collected by the detectors (Figure 22). The black and white

3D images are usually produced combining the data from different detectors, which provide the information about the crystalline structure and elemental composition of the sample, respectively.
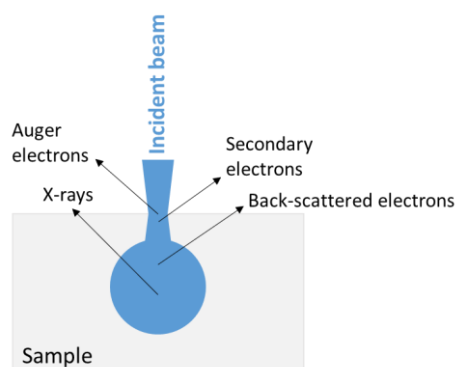
Figure 22. Scheme of the interaction volume in a sample with an incident beam and the origin of detectable signals.

Secondary electrons are widely used for the imaging due to their surface sensitivity. They are produced from inelastic scattering interactions from primary electrons. As they possess low energy (~50 eV), the escape depth is limited only to a few nanometers, thus providing the information about the surface topography.

Backscattered electrons have much higher energies than the secondary electrons, and are produced due to the elastic scattering of the incident electrons with the atoms of the sample. The production of backscattered electrons depends on the element's atomic number. Therefore, the detection of backscattered electrons provides the compositional contrast, in which the elements with higher atomic number appear brighter.

Auger electrons are emitted due to the sample de-energization after the production of secondary electrons. These electrons have low energy, as they are only emitted from the interaction volume. Auger electrons have element-specific energy, hence they are collected to provide the composition of the sample.

Characteristic X-rays are ejected from the atoms upon the interaction with the primary beam at a depth up to a micrometer. The emission of the X-rays is due to the deactivation of the excited state in the atom after the photoelectron ejection. To analyze the emitted X-rays the electron microscope must be equipped with the energy dispersive X-ray detector (EDX).

In the current work SEM was used to characterize the morphology of the carbon-coated and pristine graphite samples using a Zeiss LEO 1550 VP Field Emission Scanning Electron Microscope.

3.12 High-resolution transmission electron microscopy

High-resolution transmission electron microscopy (HRTEM) allows imaging of the samples on the atomic scale, which makes it possible to analyze the crystal structures, grain boundaries and lattice imperfections. The HRTEM images are interference patterns of the electron wave with itself after it diffracted from the sample. The image formation is obtained using the objective lenses, placed below the sample. Therefore, these lenses define the quality of the microscope's resolution and of the final image. However, the real lenses often suffer from different aberrations (i.e., spherical and chromatic aberrations, defocus and astigmatism), significantly hampering the image analysis.

The graphite electrodes used for the study were extracted from the full coin cells after the 1st and 104th cycles (3 cycles at C/2, 100 cycles at 1C, 1C = 170 mA g^{-1}), using different formation protocols, washed with 200 µL of DMC in the glove-box and dried under vacuum for 30 min. The graphite powders were scratched from the current collector, ground in the agate mortar, placed on the grid and transported inside the microscope without exposure to air. HRTEM images were recorded using the JEOL 3010 microscope at CEA-LITEN.

3.13 Raman spectroscopy

Raman spectroscopy is a technique, which can be used to determine the vibrational and electronic properties of the materials. The Raman effect occurs when photons are scattered by atoms or molecules. The energy-level diagram representing different scattering processes is shown in Figure 23. Generally, when incident monochromatic light (i.e., laser) interacts with a molecule, it can distort the electron cloud around it to form a virtual state. However, this state is not stable, so the excited electrons will immediately fall back to the ground state. The energy of the scattered light is the same as the energy of the incident light, so this process is called elastic (or Rayleight) scattering. However, some small part of the illuminated light (10^{-5}% of incident light intensity) is scattered inelastically or Raman scattered, losing (Stokes Raman scattering) or gaining (anti-Stokes Raman scattering) energy. At room temperature the amount of molecules in an excited vibrational state is generally much lower (but not zero) than that in the ground state. Upon temperature rise the amount of molecules in a higher vibrational state is increasing, but as both Stokes and anti-Stokes scatters contain equivalent frequency information, in most experimental systems only Stokes scattering is recorded.
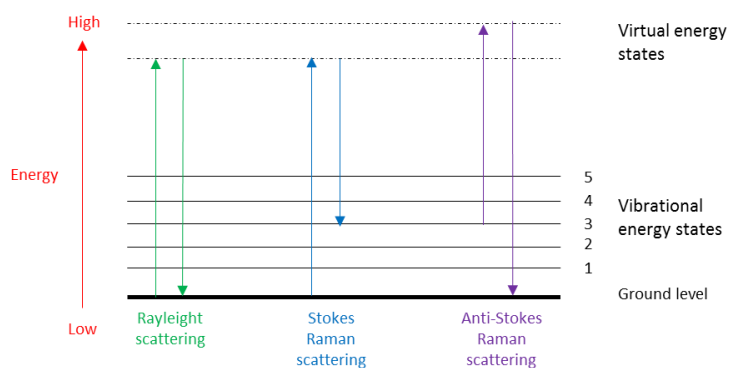
Figure 23. Energy-level diagram of the Rayleight and Raman scattering processes.

Raman spectrum can be presented in a form of intensity of the scattered light plotted against the Raman shift $\bar{\nu}$ in wavenumbers (cm^{-1}), which can be calculated using the equation:

$$\bar{\nu} = \frac{1}{\lambda_{incident}} - \frac{1}{\lambda_{scattered}}, \qquad (3.16)$$

where $\lambda_{incident}$ and $\lambda_{scattered}$ are the wavelengths (cm) of incident and Raman scattered photons, respectively. The use of wavenumber and not wavelength is usually preferred as it is linearly related to the energy and is independent of the wavelength of the excitation signal.

The energy of a vibration depends on various factors, including atomic mass, bond order, and geometry of the molecule. Moreover, the vibrations of the crystal lattice and other motions of solids are Raman-visible. The position of the peak in Raman spectrum provides the information about the molecular structure. The change of the peak width can be used to track the change in the material's crystallinity. The shift of the peak position is used to evaluate the residual stresses of the distorted crystalline structure. Furthermore, the height of the peak can be used for quantitative analysis.

In the current work Raman spectroscopy was used to investigate Li$^+$ coordination in the solid polymer electrolytes. The measurements were carried out on a Vertex 70v IR spectrometer equipped with the RAM II module (Bruker Optics). The samples were sealed in glass tubes under vacuum. The laser wavelength was 1064 nm. The collected spectra comprised the average of 1000 scans with an optical resolution of 2 cm^{-1}. The curve intensities were scaled to PEO or TFSI$^-$ modes depending on the spectral region of interest.

Additionally, Raman confocal microspectrometer, which is coupled with an optical microscope, allowing higher magnification via a microscopic laser spot, was used to identify the changes in the crystallinity due to the formation of an amorphous carbon layer on graphite surface. The spectra were collected using a confocal InVia Raman microspectrometer (Renishaw) with a laser wavelength of 633 nm.

4. RESULTS AND DISCUSSION

The following chapter consists of four sections. In Section 4.1 the individual and combined use of the ceramic filler (SiO₂) and the ionic liquid (Pyr₁₄TFSI) on the properties of the PEO-LiTFSI based solid polymer electrolyte are evaluated. Although the effect of each material independently has been evaluated in several studies, not much literature is available on the synergetic effect of the ceramic filler and the ionic liquid on the conductivity at ambient temperature and stability of the lithium metal/electrolyte interface. The work presented in Section 4.1 is based on the manuscript [159].

Formation of a stable SEI on the graphite surface has also been addressed by numerous research groups. Still, the mechanism of its formation and the composition are debated. To obtain a stable SEI one cost-effective approach is to use the electrolyte additives, which will either decompose at higher potentials than solvents and salts or incorporate in the SEI. Herein, the use of imide salts (LiTFSI, LiFSI and LiFTFSI) as additives was evaluated. Their influence on the SEI composition and cycling in half and full cells, using the electrodes with practical loadings, was compared with a state-of-the-art additive – vinylene carbonate. The results of this investigation are presented in Section 4.2 and are based on the manuscript, which was submitted for the revision during the preparation of the thesis.

Among other factors, influencing the composition and stability of the SEI, is the so-called formation, which refers to the initial cycles, necessary for the SEI build-up. The formation protocol includes a sequence of steps and requires a proper design. Due to the confidentiality of formation protocols, only little literature is available on this topic. In Section 4.3 the three formation protocols are investigated, focusing on the influence of such parameters as current density and temperature on the performance of both small coin and upscaled pouch cells.

Finally, due to the structural characteristics of graphite lithium intercalation occurs only along the edge plains. This significantly reduces the rate capability of this material. One of the elegant approaches is the introduction of the surface carbon-coating, which may provide additional diffusion pathways and enhance graphite's tolerance towards higher rates. Despite the numerous literature on this topic, the comparison of different methods and precursors is frequently complicated. Therefore, Section 4.4 presents a systematic study on the physico-chemical and electrochemical properties of carbon-coated graphite materials, focusing on non-toxic and cheap precursors. The work in Section 4.4 is based on the manuscript [160].

4.1 Quaternary solid polymer electrolytes comprising an ionic liquid and a ceramic filler for Li-polymer batteries

This section presents the study on the individual and combined influence of the ionic liquid N-butyl-N-methylpyrrolidinium bis(trifluoromethanesulfonyl)imide ($Pyr_{14}TFSI$) and the ceramic filler fumed silicon dioxide (SiO_2) on the lithium ion transport. The properties of the selected ionic liquid have been briefly discussed in Section 2.4.2. SiO_2 was chosen as electrochemically inert filler due to its low density and particularly large surface area, thus allowing a more pronounced crystallization inhibition as compared to the other fillers.

Three solid polymer electrolytes were examined: electrolyte A, containing PEO-LiTFSI with addition of the ceramic filler (SiO_2), electrolyte B, consisting of PEO-LiTFSI and the ionic liquid ($Pyr_{14}TFSI$), and electrolyte C, composed of PEO-LiTFSI with the addition of both $Pyr_{14}TFSI$ and SiO_2.

Although typically polymers with high molecular weight (M_w~4,000,000 g/mol) were used in similar studies [154, 161, 162], herein, poly(ethylene oxide), or PEO, with M_w~250,000 g/mol was chosen. Indeed, as the ions' motion only occurs along the polymer chains due to the interactions of Li^+ with the ether oxygen of PEO, the molecular weight of the polymer influences the transport mechanism. While in the high molecular weight PEO the transport is prevailed by the ion hopping, in the low molecular weight polymer rather the diffusion of the whole chain dominates the transport mechanism [163, 164]. The SPEs with low molecular weight polymers were reported to have higher lithium transference number and diffusion coefficient D_{Li}^+. The ratio PEO:LiTFSI:$Pyr_{14}TFSI$ was chosen to be 20:1:2, although the better conductivity and cycling results were achieved with 10:1:2 mixtures [154, 165] due to higher Li^+ and ionic liquid content. However, the latter composition resulted in a gel-like electrolyte, which was mechanically unstable and difficult to handle. The amount of the ceramic filler was set to 10 wt% based on the polymer weight. Higher amount of the ceramic filler, as shown by Ji et al. [166], led to higher crystallization temperatures, which in turns hindered the ionic conductivity of the SPEs. Benzophenone was used to improve the mechanical properties of the electrolytes [146, 167], and its amount was set to 5 wt% based on the polymer weight. The electrolytes were prepared, following the solvent-free procedure described in Section 3.4 and characterized in terms of chemical, physical and electrochemical properties.

4.1.1 *Thermal properties of the SPEs*

The thermal stability of the solid polymer electrolytes was determined by thermogravimetric analysis (TGA) performed in oxygen atmosphere. The weight change upon time increase is shown in Figure 24.
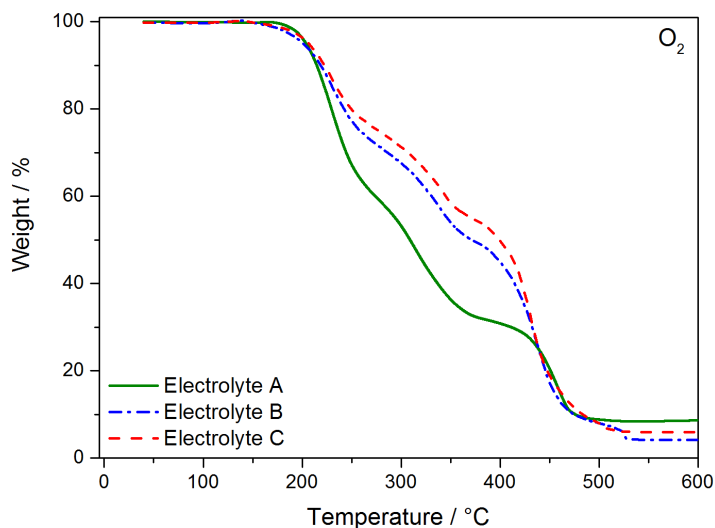
Figure 24. TGA profiles of the three solid polymer electrolytes in oxygen atmosphere with a heating rate of 10 K min^{-1}. Electrolyte A: PEO$_{20}$-LiTFSI + 10 wt%$_{PEO}$ SiO$_2$, electrolyte B: cross-linked PEO$_{20}$-LiTFSI-(Pyr$_{14}$TFSI)$_2$, electrolyte C: cross-linked PEO$_{20}$-LiTFSI-(Pyr$_{14}$TFSI)$_2$ + 10 wt%$_{PEO}$ SiO$_2$.

All electrolytes are thermally stable up to 150 °C. However, the decomposition of the electrolyte A occurs faster than for the other electrolytes. This is, however, only related to the higher total polymer content in electrolyte A, as compared to the other counterparts. From the TGA profiles it is possible to see that the electrolytes decompose in a similar manner upon the temperature increase. The first two decomposition steps (at 200 and 250 °C) of electrolytes B and C refer only to the decomposition of the polymer, whereas the plateau above 350 °C is ascribed to the decomposition of the ionic liquid and TFSI anion. This is in line with the literature reports [148, 162, 165], in which the decomposition of the ionic liquids and the salt anion was found to start at 350 °C and 400 °C, respectively. Above 500 °C for electrolytes A and C the plateau, corresponding to the remaining silica content is observed, as this ceramic filler decomposes at 1600 °C. Interestingly, in the case of SiO$_2$-free electrolyte B the small residue (~4%) is observed, which might be attributed to the formation of such inorganic decomposition species, as Li$_2$O, Li$_2$SO$_4$ and LiNO$_3$.

As discussed in Section 2.4.2, the lithium ion movement in the solid polymer electrolyte is only possible in the fully amorphous region, i.e., above its melting point (T_m). Glass transition temperature (T_g) is another important parameter, which characterizes the transition from

crystalline to amorphous state. Therefore, the lower T_g and T_m are, the higher is the conductivity of the electrolyte. The influence of individual or combined addition of the ionic liquid and the ceramic filler on these temperatures was examined via differential scanning calorimetry (DSC), shown in Figure 25. Compared to PEO$_{20}$-LiTFSI complex, the T_g of the electrolyte A is only 2 °C smaller [165]. Instead, a significant decrease in glass transition temperature is observed for electrolytes B and C, resulting in -57.7 °C and -58.4 °C, respectively. This shift of T_g towards lower temperatures is mainly attributed to the presence of the ionic liquid, which acts as a liquid plasticizer and effectively hinders the crystallization of PEO polymer [168]. The ceramic filler interacts with the ionic species, thus weakening the coordination of Li$^+$ with the ether oxygens of the polymer [144, 151]. However, the DSC traces reveal that this effect for electrolyte A is limited.
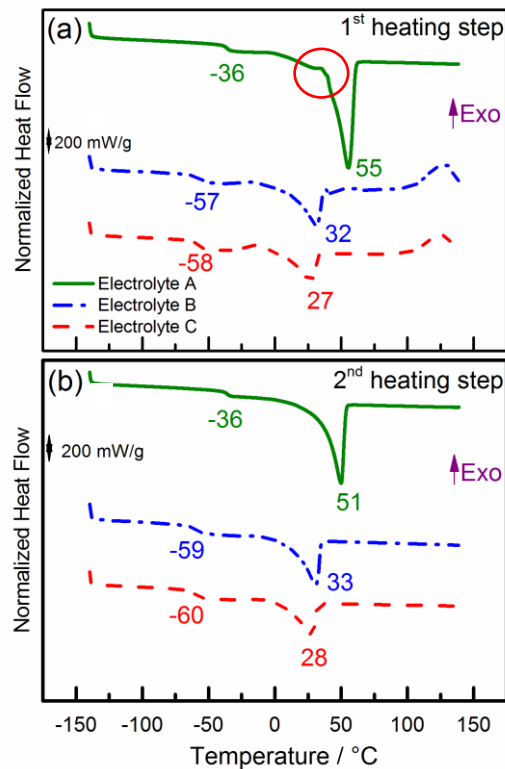
Figure 25. (a) First and (b) second differential scanning calorimetry (DSC) heating scans with a scan rate 10 K min^{-1}. Electrolyte A: PEO$_{20}$-LiTFSI + 10 wt%$_{PEO}$ SiO$_2$, electrolyte B: cross-linked PEO$_{20}$-LiTFSI-(Pyr$_{14}$TFSI)$_2$, electrolyte C: cross-linked PEO$_{20}$-LiTFSI-(Pyr$_{14}$TFSI)$_2$ + 10 wt%$_{PEO}$ SiO$_2$.

The trend is retained for the T_m and its values decrease in the order A>B>C. The melting enthalpy (ΔH_m, J g^{-1}) follows the same trend. This suggests that the electrolytes B and C had initially lower degree of crystallinity as compared to electrolyte A. The summary of the T_g, T_m and melting enthalpies (ΔH_m) in the 1st and 2nd scans is shown in Table 4.

Table 4. Summary of T_g, T_m and ΔH_m for ternary and quaternary electrolytes.

SPE	T_g, °C		T_m, °C		ΔH_m, J·g⁻¹	
	1st	2nd	1st	2nd	1st	2nd
A	-36.2	-36.3	55.4	51.3	55.8	63.4
B	-57.7	-59.8	31.9	32.6	32.8	32.5
C	-58.4	-60.5	27.3	28.3	25.7	23.4

Below the melting point of electrolyte A the small and broad feature (marked with red circle) can be ascribed to the melting of the crystalline $P(EO)_6$:LiTFSI phase [142, 169]. This peak, however, disappears in the 2nd heating scan, suggesting the slow recrystallization kinetics of the polymer-Li salt complex. At the same time T_m peak shifts to the lower temperatures. The effect of the ionic liquid on the size of the amorphous fraction in the polymer has been investigated by various groups [154, 161, 167, 170]. Initially, it was proposed that the TFSI anion from the ionic liquid decreases the interactions of Li^+ with ether oxygens in the PEO chains. However, Diddens et al. [171] showed that the ionic liquid, acting as plasticizer, mostly increases the segmental motion of PEO chains and, thus, enhances the dynamics of the interacting cations. In the first heating scan two endothermic peaks at 100 °C are most likely attributed to the reaction of residual intermediates/products of the cross-linking. As these peaks disappear in the following scan, the annealing step is sufficient for their elimination.

4.1.2   Coordination of Li^+

Raman spectroscopy is an effective technique to examine the Li ion coordination in solid polymer electrolytes. Since cross-linking can significantly hinder the crystallization of the polymer [167], the non-cross-linked samples were additionally investigated. This allowed the study of the influence of the ionic liquid and ceramic filler on Li^+ coordination independently. Additionally, the binary PEO-LiTFSI solid polymer electrolyte was added for the better comparison.

The expansion/contraction mode of the TFSI anion, which includes the motion of SN, NSO, SCF_3, and CF_3 groups [172] is shown in Figure 26. For the pristine ionic liquid this peak usually appears at 741 cm⁻¹ and it is generally attributed to the "free" TFSI anions, which are not coordinated to the cations [172, 173]. In the binary ionic liquid-Li^+ systems a shoulder typically appears at 748 cm⁻¹, which is attributed to the strong interaction between the cation and anion [173]. However, in the spectra in Figure 26 no shoulders due to the possible coordination of Li^+ and $TFSI^-$ are seen. The minor shift to lower wavenumbers for several materials is rather related to the resolution of the instrument than to the change in the molecules interactions.
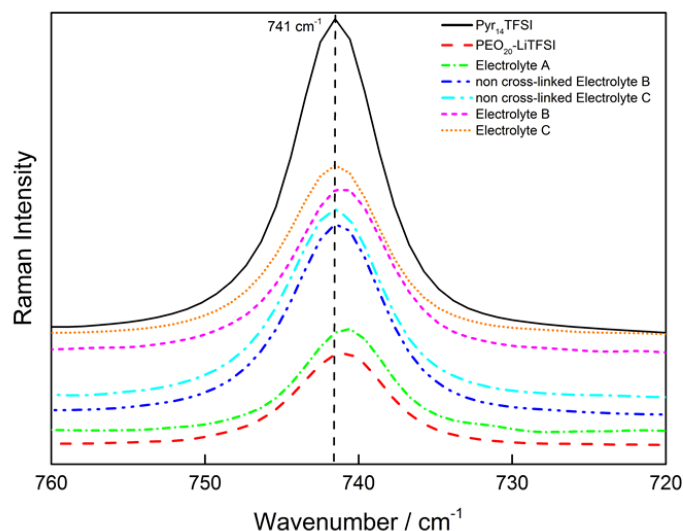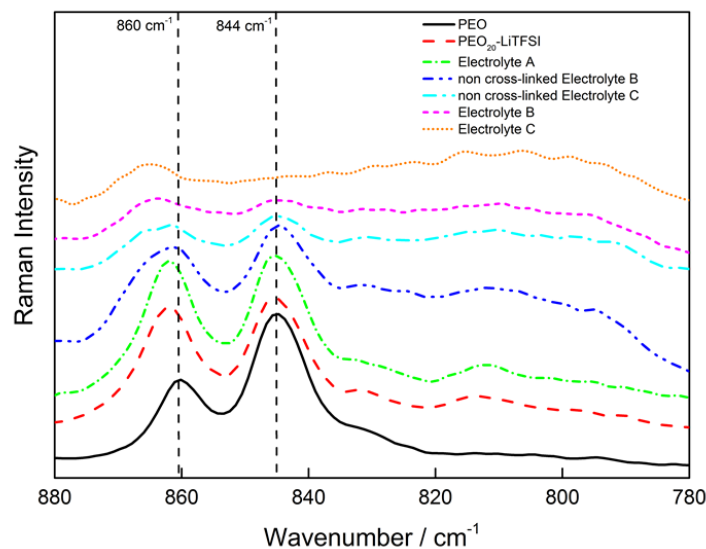
Figure 26. Raman spectra of the SPEs. Wavenumber region: 720 – 760 cm^{-1}. Electrolyte A: PEO$_{20}$-LiTFSI + 10 wt%$_{PEO}$ SiO$_2$, electrolyte B: non or cross-linked PEO$_{20}$-LiTFSI-(Pyr$_{14}$TFSI)$_2$, electrolyte C: non or cross-linked PEO$_{20}$-LiTFSI-(Pyr$_{14}$TFSI)$_2$ + 10 wt%$_{PEO}$ SiO$_2$.

The typical PEO bands, ascribed to the mixed modes, including CH$_2$ rocking and CO stretching modes [172, 174] with the peaks at 844 cm^{-1} and 860 cm^{-1}, respectively, are shown in Figure 27. The peak at 844 cm^{-1} is mostly attributed to the CH$_2$ motion, whereas the contribution of CO is small. Therefore, this signal is more sensitive to the structure of PEO. On the contrary, the peak at 860 cm^{-1} is primarily associated with the CO motion with lower contribution from CH$_2$. Thus, it is more sensitive to the interactions between Li$^+$ and ether oxygens [172].

Figure 27. Raman spectra of the SPEs. Wavenumber region: 820 – 880 cm^{-1}. Electrolyte A: PEO$_{20}$-LiTFSI + 10 wt%$_{PEO}$ SiO$_2$, electrolyte B: cross-linked PEO$_{20}$-LiTFSI-(Pyr$_{14}$TFSI)$_2$, electrolyte C: cross-linked PEO$_{20}$-LiTFSI-(Pyr$_{14}$TFSI)$_2$ + 10 wt%$_{PEO}$ SiO$_2$.

The shift of the peak from 860 cm^{-1} to 862 cm^{-1} (red line) is observed, when the salt is mixed with the polymer due to the coordination of lithium ions with PEO. The reduced intensity of the low frequency peak (844 cm^{-1}) for binary PEO-LiTFSI and electrolyte A is most likely related to the presence of the salt or salt with a ceramic filler (red and green lines, respectively), which reduces the crystalline fraction of the polymer. A further decrease in the intensities of both non- (blue line) and cross-linked (purple line) electrolyte B peaks is ascribed to the addition of the ionic liquid as compared to PEO-LiTFSI mixture and ternary SPE with SiO$_2$. A drastic decrease in the signals is observed when silica is added to the ternary electrolyte, both non- and cross-linked (light blue and orange lines, respectively). Joost et al. [165] obtained similar spectra with higher content of the ionic liquid. This might indicate that the ceramic filler can be as efficient as the higher ionic liquid content towards the reduction of the PEO crystallinity. In case of non-cross-linked ternary electrolyte, containing the ionic liquid and both quaternary electrolytes (non- and cross-linked) the peak at higher frequencies has a shoulder at 865 cm^{-1}. This might indicate that two populations of ether oxygens in PEO co-exist in presence of the ionic liquid. One of these populations has stronger interactions with Li ions, whereas another one has very weak or no interactions with the ions. The 865 cm^{-1} signal is the strongest in the region of examination for the cross-linked quaternary electrolyte, suggesting that the joint presence of the ionic liquid and the ceramic filler results in both reduced polymer crystallinity and enhanced coordination of Li ions with ether oxygens. This might, in turns, improve the

mobility of the polymer and the Li^+ in the quaternary electrolyte, which was then further investigated using the conductivity and limiting current density measurements.

4.1.3 Electrochemical properties of the SPEs

4.1.3.1 Ionic conductivity measurements

The ionic conductivity is an important parameter of each electrolyte, as it characterizes the speed of motion of the electrochemically active species. The measurements were conducted in the temperature range between 20 and 80 °C with a 10 °C step using the electrochemical impedance spectroscopy. The Arrhenius plot of the conductivity values plotted *vs* the temperature for different SPEs is shown in Figure 28.
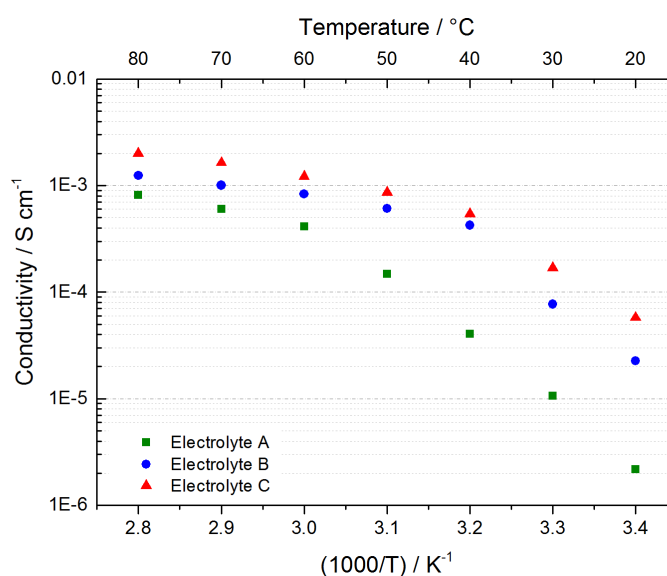
Figure 28. Arrhenius conductivity as a function of temperature of the SPEs. Electrode area: 4 cm². Electrolyte A: PEO_{20}-LiTFSI + 10 wt%$_{PEO}$ SiO_2, electrolyte B: cross-linked PEO_{20}-LiTFSI-(Pyr$_{14}$TFSI)$_2$, electrolyte C: cross-linked PEO_{20}-LiTFSI-(Pyr$_{14}$TFSI)$_2$ + 10 wt%$_{PEO}$ SiO_2.

Ternary electrolyte A, containing a ceramic filler exhibits a clear slope change above 50 °C, attributed to the crystalline-amorphous transition and, thus, to the enhanced ion mobility. This is in agreement with the DSC results, which have revealed the melting of the polymer to occur at ~55 °C. Similar behavior has been observed with a binary PEO_{10}-LiTFSI mixture [154]; however, the slope change occurred at lower temperature due to the higher salt fraction, which had a higher plasticizing effect than addition of 10 wt%$_{PEO}$ of the ceramic filler. In case of ternary electrolyte B with ionic liquid, the curve follows the Vogel-Tamman-Fulcher behavior, exhibiting a continuous conductivity increase without any notable slope change. This indicates that the polymer is present in the amorphous state also below the melting point. The conductivity threshold, needed for the real applications ($\sigma > 10^{-4}$ S cm^{-1}) is overcome for the

electrolytes B and C at 35 °C and 30 °C, respectively. The conductivity difference between electrolytes B and C indicates that the ionic liquid rather than the ceramic filler contributes more to the total conductivity increase. However, it is well-known that the addition of the ionic liquid leads to the conductivity increase up to 3 times due to the presence of additional mobile ions (i.e., Pyr_{14}^{+}). Above 60 °C the quaternary electrolyte C shows a change in the conductivity slope, which can be related to the specific interactions between the ceramic filler and the ionic liquid. It has been reported [175] that such interactions of the ionic liquid on the surface of the ceramic filler lead to the emersion of the ionically conductive pathways, which improve Li ion transport.

4.1.3.2 Limiting current density measurements

As mentioned above, the conductivity represents the mobility of all ionic species in the electrolyte. Therefore, to investigate the mobility of only the electroactive Li ions, which is of interest for practical battery applications, the limiting current density test was applied using linear sweep voltammetry. The test was conducted via applying a linear potential ramp to the symmetrical Li/SPE/Li pouch cells, and recording the current at 40 °C. The current response curves of the cells with three SPEs are shown in Figure 29. The determination of the limiting current density was adopted from [176], making a linear fit of the current response above 500 mV and taking the value of the intercept with y axis.
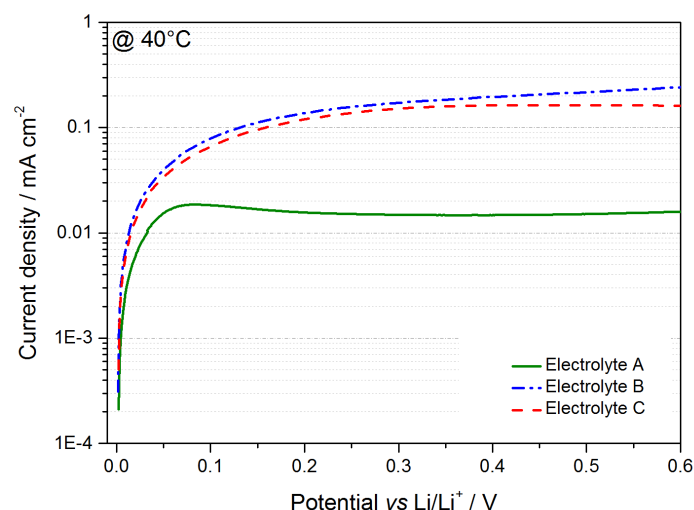
Figure 29. Current density as a function of the potential plot of symmetrical Li/SPE/Li cells at 40 °C. Electrode area: 2-3 cm². Potential step: 0.01 mV s^{-1}. Electrolyte A: PEO_{20}-LiTFSI + 10 wt%$_{PEO}$ SiO_2, electrolyte B: cross-linked PEO_{20}-LiTFSI-$(Pyr_{14}TFSI)_2$, electrolyte C: cross-linked PEO_{20}-LiTFSI-$(Pyr_{14}TFSI)_2$ + 10 wt%$_{PEO}$ SiO_2.

As follows from Figure 29, the current flowing through the electrolyte A is significantly smaller than that of B and C. The enhanced Li$^+$ diffusion of the electrolytes B and C can be correlated with the lower T_m of these electrolytes, as detected by DSC. Within the investigated potential

range, the current density of the electrolyte B is continuously increasing, whereas the current densities of A and C reach a plateau. Although the reason for such behavior of the electrolyte B needs to be further clarified, one possible explanation could be the continuous growth of the interphase layer between the polymer and Li metal, which does not reach the equilibrium within the studied voltage range. The current density response of the electrolyte B is slightly higher than that of electrolyte C. However, the linear fitting of the plateau results in the lower value of the current density for the electrolyte B due to the steeper slope. The fitted limiting current densities are 0.02, 0.09 and 0.11 mA cm^{-2} for electrolytes A, B and C, respectively. These results are in agreement with the conductivity measurements. All in all, it should be noted that the correlation of the current densities of the SPEs is more important than the absolute values.

4.1.3.3   *Lithium stripping/plating test*

To determine the efficiency of lithium deposition process and the stability of interfacial layer between Li metal and SPE upon long-term cycling, lithium striping/plating (or polarization) test was conducted on symmetrical Li/SPE/Li cells. The experiments were conducted in galvanostatic mode, reversing the current (0.078 mA cm^{-2}) every hour and recording the overpotential [177]. The current density, applied during the experiment, was set to a value slightly below the limiting current density of the ionic liquid-containing electrolytes B and C. This allowed to obtain the information about the electrolytes' long-term performance undergoing high stresses. However, since the applied current density was higher than the limiting current density for electrolyte A, the cell immediately failed, as marked with a red oval in the upper left part of Figure 30. The cells with electrolytes B and C, on the contrary, show excellent cycling stability upon long-term cycling. While with the electrolyte B the cell overvoltage is slightly increasing during the experiment, the overvoltage with quaternary electrolyte slightly decreases upon cycling, in line with the limiting current density measurements. These results confirm that the passive layer, formed spontaneously on the surface of Li metal, is unstable in case of electrolyte B as it is constantly growing, whereas in case of electrolyte C the passivation film stabilizes after some cycles.
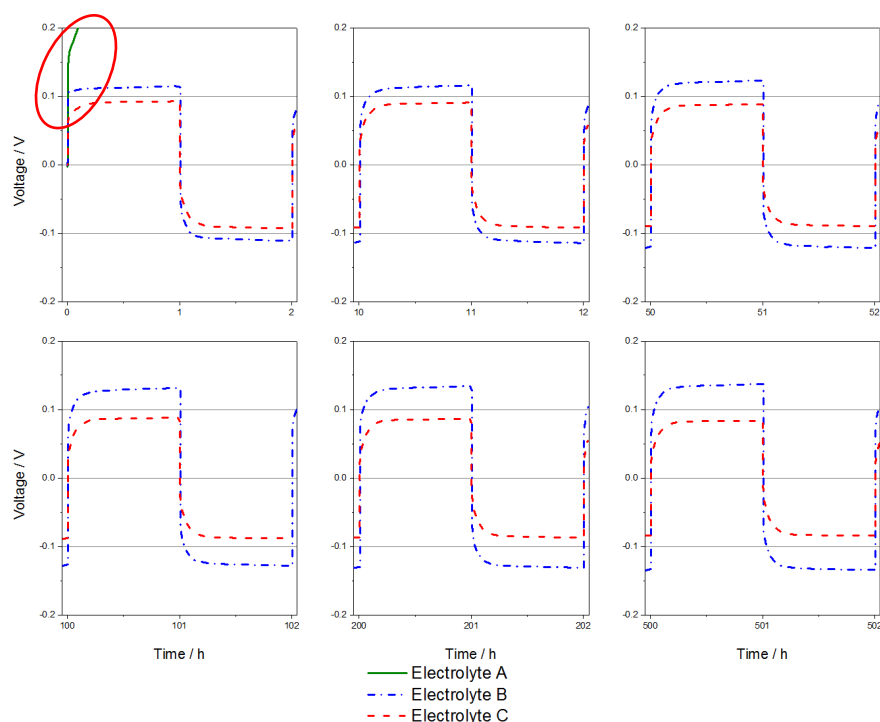
Figure 30. Polarization (Li stripping/plating) test of the symmetrical Li/SPE/Li cells at 40 °C. Stripping/plating time: 1 h. Applied current density: 0.078 mA cm^{-2}. Lithium foil thickness: 0.05 mm. Contact area: 1.7 - 2.4 cm². Electrolyte A: PEO$_{20}$-LiTFSI + 10 wt%$_{PEO}$ SiO$_2$, electrolyte B: cross-linked PEO$_{20}$-LiTFSI-(Pyr$_{14}$TFSI)$_2$, electrolyte C: cross-linked PEO$_{20}$-LiTFSI-(Pyr$_{14}$TFSI)$_2$ + 10 wt%$_{PEO}$ SiO$_2$.

4.1.3.4   *Time evolution of impedance*

To better understand the compatibility of the SPEs with Li metal and monitor the changes in the passive layer at the Li/SPE interface, the electrochemical impedance measurements were conducted at OCV conditions on symmetrical Li/SPE/Li cells at 20 °C and 40 °C. The resulting Nyquist plots are shown in Figure 31.
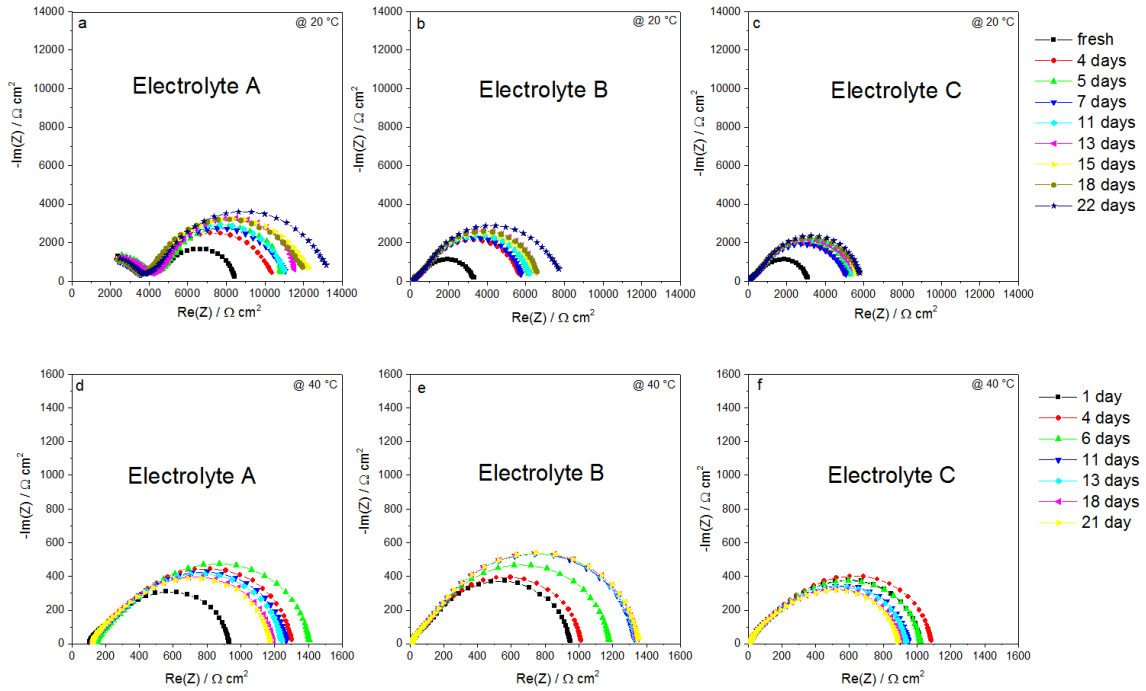
Figure 31. Nyquist plots, representing time evolution of impedance of symmetrical Li/SPE/Li cells at 20 °C (a-c) and 40 °C (d-f). Contact area: 1.5 - 2.5 cm². Electrolyte A: PEO_{20}-LiTFSI + 10 wt%$_{PEO}$ SiO_2, electrolyte B: cross-linked PEO_{20}-LiTFSI-$(Pyr_{14}TFSI)_2$, electrolyte C: cross-linked PEO_{20}-LiTFSI-$(Pyr_{14}TFSI)_2$ + 10 wt%$_{PEO}$ SiO_2.

The time evolution of impedance upon storage at 20 °C is shown in the upper panels (a-c) of Figure 31. The plots represent typical impedance spectra of the SPEs, where high frequency intercept with real axis (Z') is ascribed to the bulk resistance of the electrolyte, which remains constant upon storage. The semicircle in the middle-to-high frequency domain is ascribed to two contributions. These include the formation of the passive layer on the surface of Li metal and the electronic charge transfer. As the time constants of these processes are very close, they are not easily distinguishable. Therefore, they are treated as a whole and recognized as interfacial impedance. For the electrolyte A an additional semicircle at high frequency is observed (Figure 31a) due to the high bulk electrolyte resistance at 20 °C, which, shifts the frequency range towards lower values. Among three electrolytes, electrolyte C shows the lowest resistance upon storage at room temperature.

As expected, at 40 °C there is a considerable decrease of the total impedance with all electrolytes, as can be seen in lower panels (d-f) of Figure 31. Interestingly, at this temperature different trends in cell impedance upon aging are observed. In case of electrolyte A, the interfacial impedance initially increased and then dropped down after 6 days. For the electrolyte B the impedance increased during 11 days and then stabilized. Quaternary electrolyte C exhibited similar behavior to electrolyte A with the initial rise of the impedance, followed by

its decrease after, in this case, only 4 days of aging. Interestingly, after 21 days of aging the interfacial impedance was even lower than that after 1 day.

From the observation of the impedance evolution at the Li/SPE interface some conclusions can be derived. The impedance behavior of electrolyte A can be explained by assuming the presence of impurities (i.e., liquids) trapped by the ceramic filler and contributing to a stable SEI with low resistance as found by other authors [151]. The behavior of electrolyte B is due to the presence of $Pyr_{14}TFSI$ that also participates in the formation of the protective layer promoting the movement of ionic species but at the expense of the time required for surface stabilization. The combined presence of the ceramic filler and the $Pyr_{14}TFSI$ in electrolyte C might result in the formation of a thin SEI that rapidly grows and likewise rapidly stabilizes with improved Li^+ transport.

4.1.3.5   *Galvanostatic cycling in Li/SPE/LFP cells*

The cycling behavior and the voltage profiles of full Li/SPE/LiFePO$_4$ cells at 40 °C are shown in Figure 32. The composite cathode polymer tape contains LiFePO$_4$ (43 wt%), conductive carbon (7 wt%), PEO (21 wt%), LiTFSI (7 wt%) and $Pyr_{14}TFSI$ (22 wt%). The electrochemical performance of the cell with electrolyte A is not shown as the migration of the ionic liquid from the composite electrode into the electrolyte affects the cycling performance.

As shown in Figure 32a, the cells deliver relatively high discharge capacities in the first cycle (130 and 120 mAh g^{-1}, respectively). However, the irreversible loss in the first cycle is high as well, determining the abrupt drop of the capacity. The coulombic efficiency reaches ~100% only by the 10th cycle. The discharge capacity of the cell with electrolyte B slightly decreases during cycling, whereas the cell with electrolyte C shows stable cycling and the capacity of ~70 mAh g^{-1}.
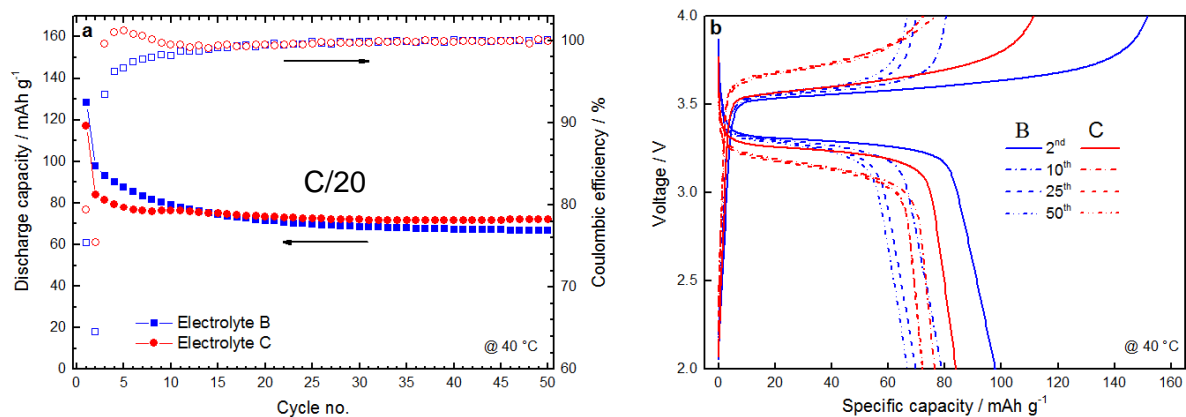
Figure 32. Cycling performance (a) and voltage profiles (b) of the Li/SPE/LFP cells, with electrolytes B and C at 40 °C. Electrolyte B: cross-linked PEO_{20}-LiTFSI-$(Pyr_{14}TFSI)_2$, electrolyte C: cross-linked PEO_{20}-LiTFSI-$(Pyr_{14}TFSI)_2$ + 10 wt%$_{PEO}$ SiO_2.

Figure 32b shows the voltage profiles of the 2nd, 10th, 25th and 50th cycle for the cells with electrolytes B and C at 40 °C. A notable decrease in the voltage plateau is observed for both cells. This can be linked with the formation and growth of the passive layer on the Li metal surface observed during the impedance measurements. Upon cycling the length of the voltage plateau of the cell with electrolyte B is continuously decreasing while the cell polarization is increasing. In case of the cell with electrolyte C, the initial voltage plateau is shorter than that of the cell with electrolyte B. However, after the passive layer is formed, the plateaus length remain stable and the voltage profiles of the 25th and 50th cycles are overlapping.

4.1.4 Conclusions

In this section SPEs containing an ionic liquid and a ceramic filler were investigated. It was shown that the ceramic filler alone has a minor influence on the T_m of the electrolytes, which, instead, is significantly reduced by $Pyr_{14}TFSI$. Therefore, the addition of $Pyr_{14}TFSI$ increases the low temperature ionic conductivity more efficiently than the ceramic filler. However, all electrolyte properties are further improved when both $Pyr_{14}TFSI$ and the ceramic filler are present. The resulting SPE has the lowest T_g and T_m, and the highest conductivity. The results of Raman spectroscopy suggest that the presence of both $Pyr_{14}TFSI$ and the ceramic filler in the quaternary SPE lead to a more effective hindering of PEO crystallization and to an enhanced coordination of Li^+ to the ether oxygens. Additionally, the quaternary SPE shows a higher limiting current density, i.e., Li^+ mobility. For this electrolyte, the stripping/plating experiment and the interface impedance measurements show the growth of a stable thin SEI at the Li/SPE interface after some days, whereas a continuous growth of the SEI is observed for the ternary electrolyte containing only $Pyr_{14}TFSI$ (electrolyte B). Despite a lower initial capacity, the

presence of both additives in electrolyte C leads to the best long-term cycling performance in Li/SPE/LiFePO$_4$ cells.

4.2 Comparative study of imide-based Li salts as electrolyte additives for Li-ion batteries

LiTFSI has been widely used as a conducting salt in the Li-polymer batteries due to its bulky anion and delocalized charge, which enable its fast dissociation in the polymer. Furthermore, the substitution of the state-of-the-art lithium hexafluorophosphate ($LiPF_6$) by this imide-based salt in organic liquid electrolytes has been considered by various research groups. The main advantages of LiTFSI compared to $LiPF_6$ include its negligible sensitivity towards hydrolysis and wider electrochemical stability window. However, such drawback as the anodic dissolution of the Al current collector, which is not passivated in presence of LiTFSI, requires the addition of specific additives, like fluoroethylene carbonate (FEC), or even $LiPF_6$. Additionally, the other imide-based salts, like LiFSI and LiFTFSI have gained considerable interest in the past years.

Although the use of LiTFSI or LiFSI as electrolyte additives has been previously investigated, it is not fully understood what is the impact of the salts on the SEI formation on graphite and how it correlates with the performance in the half and full cells. In the next chapter, the use of imide-based Li salts as electrolyte additives (2 wt%) and their effect on the formation of the SEI and cell performance will be compared to that of the state-of-the-art vinylene carbonate (VC) additive or additive-free electrolyte. The results reported in the following subchapter were also included in the manuscript, which was submitted during the preparation of the thesis. The XPS spectra acquisition as well as their fitting was done by Dr. Thomas Diemant (University of Ulm, Germany).

4.2.1 Electrochemical performance in half and full cells

The effect of the additives on the electrochemical stability window (ESW) of the electrolytes was determined via linear sweep voltammetry (LSV), using freshly assembled cell for each anodic and cathodic sweep. Several authors have pointed out that the working electrode used for the measurement affects the results, e.g., platinum is more sensitive to degradation reaction than glassy carbon [178, 179]. Therefore, we compared the results obtained using Pt and carbon (Super C45/CMC=80/20) working electrodes (Figure 33, panels *a* and *b*, respectively). Using Pt, all electrolytes appear to be stable between 0.5 and 5.0 V *vs* Li/Li$^+$. Instead, when using carbon a narrower ESW (about 3 V) was obtained as shown in Figure 33b. Indeed, the electrolyte degradation occurs readily on the high surface area of the carbon electrode (at both high and low potentials), where the latter is also a better model than Pt for the conditions in a real Li-ion cell. Below 1.5 V *vs* Li/Li$^+$, as highlighted in the inset of Figure 33b, all electrolytes

display reduction peaks related to the SEI formation on the carbon surface. The bare electrolyte shows the typical ethylene carbonate (EC) reduction peaks at 0.65 V *vs* Li/Li$^+$, which is shifted to higher potential (~0.8 V *vs* Li/Li$^+$) when vinylene carbonate (VC) is added. The latter decomposes at about 1.0 V *vs* Li/Li$^+$, as indicated by the broad peak in Figure 33b and already reported in literature [134]. On the other hand, addition of imide salts to the electrolyte does not prevent the reduction of EC. Indeed, the voltammograms of the bare LP30 electrolyte and those with imides are very similar.
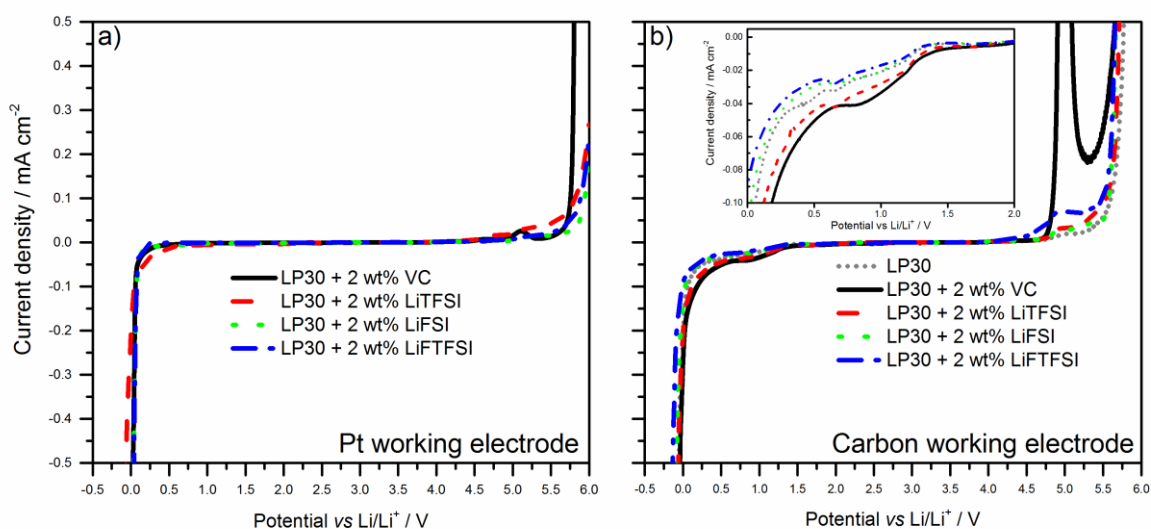
Figure 33. Linear sweep voltammetry of various electrolytes using (a) Pt and (b) carbon working electrodes (at the inset enlarged portion of the cathodic sweep).

In the anodic scan on Pt, the electrolytes with LiFSI and LiFTFSI show an increased stability compared to that of LiTFSI and VC (Figure 33a). In case of the carbon working electrode all electrolytes display current flow above 4.5 V *vs* Li/Li$^+$ due to the degradation of the solvents and LiPF$_6$. A strong, well defined peak is displayed only by the VC-containing electrolyte at about 4.8 V *vs* Li/Li$^+$, which is related to the decomposition of this additive and formation of polyvinyl carbonate species [133]. The electrolytes with imide additives display higher current densities between 4.5 and 5.3 V *vs* Li/Li$^+$ than the bare electrolyte. This effect may originate from inhomogeneity in the loading of carbon electrodes that, influencing the total surface area, affects the extent of the decomposition reaction at electrode/electrolyte interface. However, further and more detailed investigations on the anodic behavior of the electrolytes with imide salts additives are necessary, if their combination with cathode materials working at potential higher than 4.0 V *vs* Li/Li$^+$ needs to be exploited.

Figure 34 shows the electrochemical performance of graphite electrodes in the different electrolytes, comparing the 1st cycle voltage profiles. The first cycle efficiency determines

(mostly) how much lithium is consumed for the SEI build-up. This is a rather important characteristic, because the inefficiency must be balanced by extra cathode material in the Li-ion cell. For the additive-free electrolyte the efficiency is 93.3%; and the electrolyte doped with LiTFSI shows exactly the same value, whereas LiFSI and LiFTFSI offer slightly higher efficiencies (93.6% and 93.8%, respectively). On the other hand, the 1st cycle efficiency using VC is only 91.5%, indicating that a higher amount of Li$^+$ is depleted upon VC polymerization [136].

As reported in Figure 34a, the cells with pure and imide-doped electrolytes show higher capacities than that with VC in the following cycles at C/2 and 1C rates. However, when the cycling rate further increases, a drop in capacity is observed for those cells employing LiFSI or LiFTFSI. The "fingerprint" cycles at C/2 show the same capacity for all cells, thus degradation of graphite electrodes due to high cycling rates can be excluded. In the last part of the test (Figure 34b), i.e., when the cells are cycled at C/2, the cell with VC shows a capacity decrease (partially recovered upon cycling), while a very stable cycling behavior is achieved with imide salts.
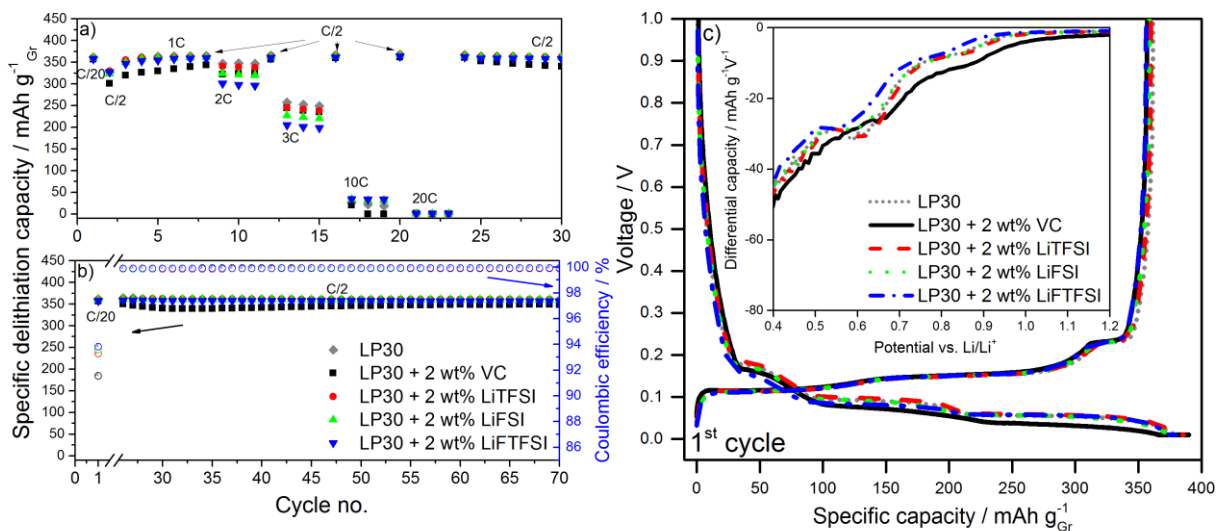
Figure 34. a) Rate capability test, b) cycling performance and c) voltage profiles of graphite half-cells with different electrolyte additives. The inset in panel c shows a differential capacity plot.

Figure 34c shows that graphite displays a higher polarization below 0.2 V upon lithiation when VC is used, indicating a more resistive SEI than that obtained with other additives. The inset of Figure 34c reports a portion of the differential capacity plots during the 1st cycle. In agreement with the ESW results in Figure 33b, a series of reduction peaks can be distinguished below 1.0 V. At around 0.9 V, the passivation of the graphite electrodes begins with decomposition of LiPF$_6$, as shown by the bare electrolyte trace [180]. For the electrolyte containing VC, this

process is preceded by the decomposition of the additive, which results in the peaks overlapping [133, 134]. Between 0.7 and 0.65 V the reduction of EC takes place. This is little affected in presence of the Li-imide salts, but is almost suppressed for VC-containing electrolyte. Also for LiFSI- and LIFTFSI-containing electrolytes the intensity of this feature is lowered, suggesting that the decomposition of EC is, at least, reduced.

Upon cycling, the trend in the higher polarization with VC-containing electrolyte is maintained, as shown in Figure 35b. However, a slightly higher polarization also emerges after 60 cycles for the LiFTFSI-added electrolyte (Figure 35e). Moreover, at the beginning of the delithiation a sharp voltage increase is observed for the cell containing VC. This phenomenon has been ascribed to the prevention of Li$^+$ deintercalation by the SEI upon cell discharge, which leads to the increased resistance between the electrolyte and electrode interface and lower delivered capacity [181].
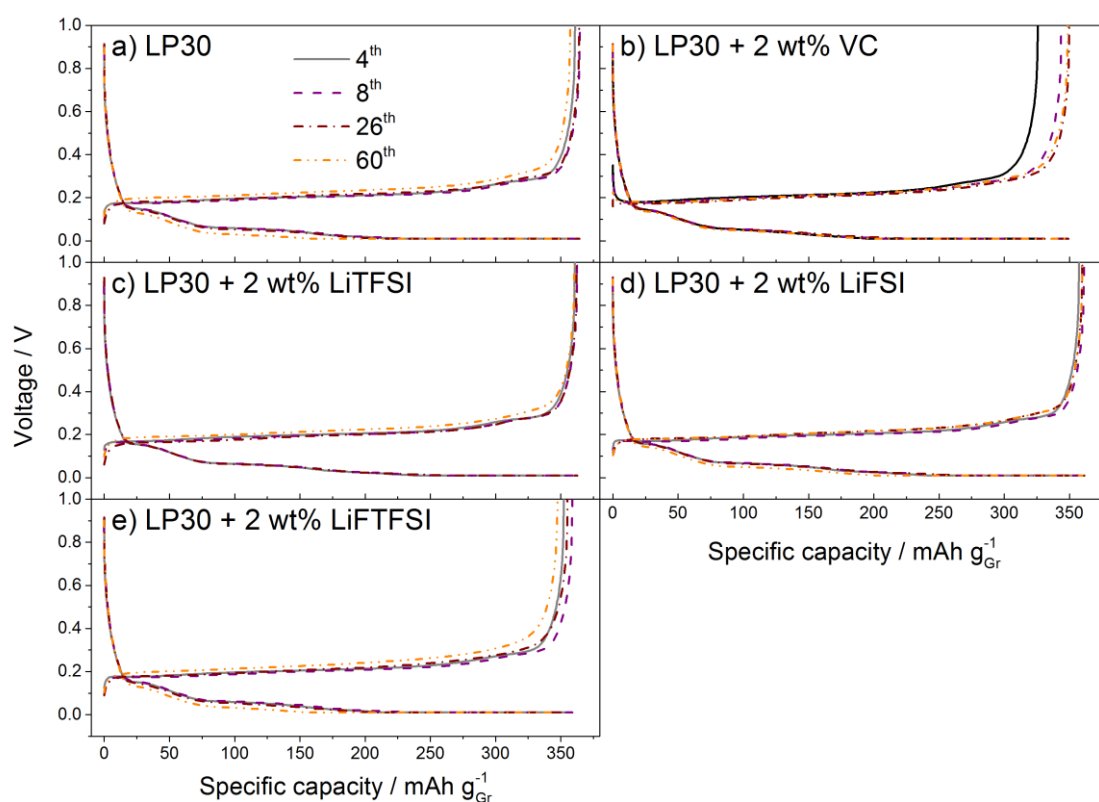
Figure 35. Voltage profiles of Li/graphite half-cells at C/2 with the various electrolytes (see legends).

In order to study the impact of imide salts on the performance of full Li-ion cells, the performance of LiFePO$_4$ (LFP) electrodes in these electrolytes was also tested. As shown in Figure 36, LFP electrodes display a better rate performance (especially at 3C) and more stable cycling when the imide salts are added to the electrolyte as compared to VC. The 1st cycle

efficiencies are comparable with different electrolytes, comprising 99.0%, 98.6%, 97.3% and 96.8% for LiTFSI, VC, LiFSI and LiFTFSI, respectively.
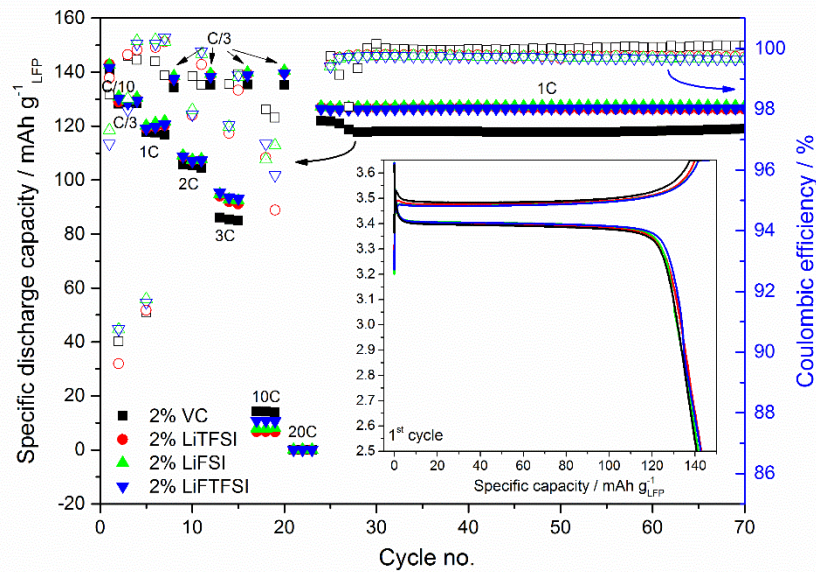
Figure 36. Cycling performance with inset (voltage profile) of the LFP half-cells with the various electrolyte additives.

To evaluate the influence of the additives on the long-term cycling performance, full cells comprising graphite anodes and LFP cathodes were assembled and tested. The cycling behavior at 20 and 40 °C is shown in Figure 37 and summarized in Table 5.
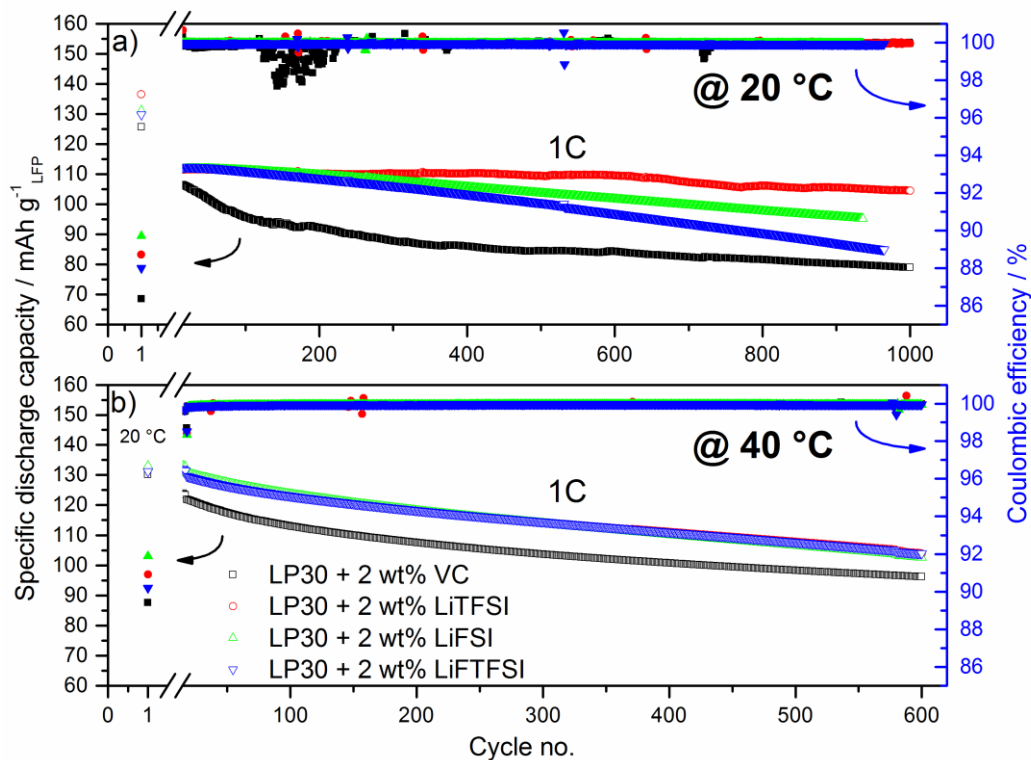
Figure 37. Cycling performance of full graphite-LFP cells at a) 20 °C and b) 40 °C.

As reported in Table 5, at 20 °C (Figure 37a) the cell with the electrolyte doped with LiTFSI shows the highest 1st cycle efficiency and the most stable cycling performance in agreement with the half cell results (the voltage profiles of the full cells are shown in Figure A1 of the APPENDIX 2). When LiFSI or LiFTFSI are used as additives, the long-term cycling stability is poorer than that obtained for the electrolyte with LiTFSI. At 40 °C, as follows from Figure 37b, higher capacities are generally obtained. However, the temperature increase has a detrimental effect on the cycling stability, especially for the cells with imide salts, displaying at 40 °C capacity retentions comparable to that of the cell with VC.

Table 5. Summary of the first cycle efficiency and capacity retention of the full cells with four electrolytes.

Electrolyte	1st cycle efficiency at 20 °C, %	Capacity retention (600th *vs* 20th cycle) at 20 °C, %	Capacity retention (600th vs 20th cycle) at 40 °C, %
LP30 + 2 wt% VC	86.3	79.6	78.7
LP30 + 2 wt% LiTFSI	88.7	98.1	79.7
LP30 + 2 wt% LiFSI	89.7	90.9	78.6
LP30 + 2 wt% LiFTFSI	88.0	86.3	79.9

The electrochemical results presented so far confirm the beneficial effect of the use of imides salts, especially LiTFSI, as additives. Recently the reactivity of carbonate-based electrolytes containing lithium imides as main salts has been reported [182, 183]. It has been shown that LiFSI and LiFTFSI are more prone to electrochemical reduction than LiTFSI at about 1 V *vs* Li/Li$^+$ due to the easier cleavage of the F-S bond than the F$_3$C-S bond. To understand if the origin of the improved half and full cell performance is related to the SEI layer characteristics, X-ray photoelectron spectroscopy (XPS) analysis was performed on the delithiated graphite electrodes extracted from the cells after the 1st or the 50th cycle.

4.2.2 Ex-situ surface analysis of the cycled graphite electrodes

Figure 38 compares the C1s spectra of the delithiated graphite electrodes extracted from the cell after the 1st or the 50th cycle. The dominant peak at 284.6 eV originates mainly from the sp^2 hybridized graphite, but also includes contributions from the CMC binder and conductive carbon added into the electrode composites. The peak at 282.5 eV is attributed to lithiated graphite species (i.e., Li$_x$C$_6$), suggesting that the delithiation was not fully completed. As these species refer to the graphite substrate and are not the SEI components, their appearance in the

spectra suggests that the SEI is not very thick, especially on the electrode taken from the cell with LiFSI as additive. The broad feature at 286.6 eV is assigned mainly to the C atoms of the C-O-C groups in PEO, which is formed upon solvent polymerization [184-187]. The formation of PEO is also confirmed by the peak at 533.6 eV in the O1s XPS spectra in Figure 38c. The rather broad peaks at 288.6 eV and 290.3 eV in Figure 38a are assigned to carbon in C=O groups in organic lithium alkyl carbonates (ROCO$_2$Li) and lithium carbonates (Li$_2$CO$_3$) [185], respectively. The corresponding peak of the oxygen atoms in these groups is detected in the O1s spectra (Figure 38c) at 531.8 eV. In the presence of imide salts in the electrolyte, the latter one is the dominant peak in the O1s spectra, in contrast to the case of the electrolyte containing VC. In this electrolyte the formation of polymeric species resulting from the additive decomposition is indicated by the weak peak at 291.1 eV. In the O1s spectra this species should give a signal at 534.5 eV [134], which overlaps, however, with the C-O-C peak.
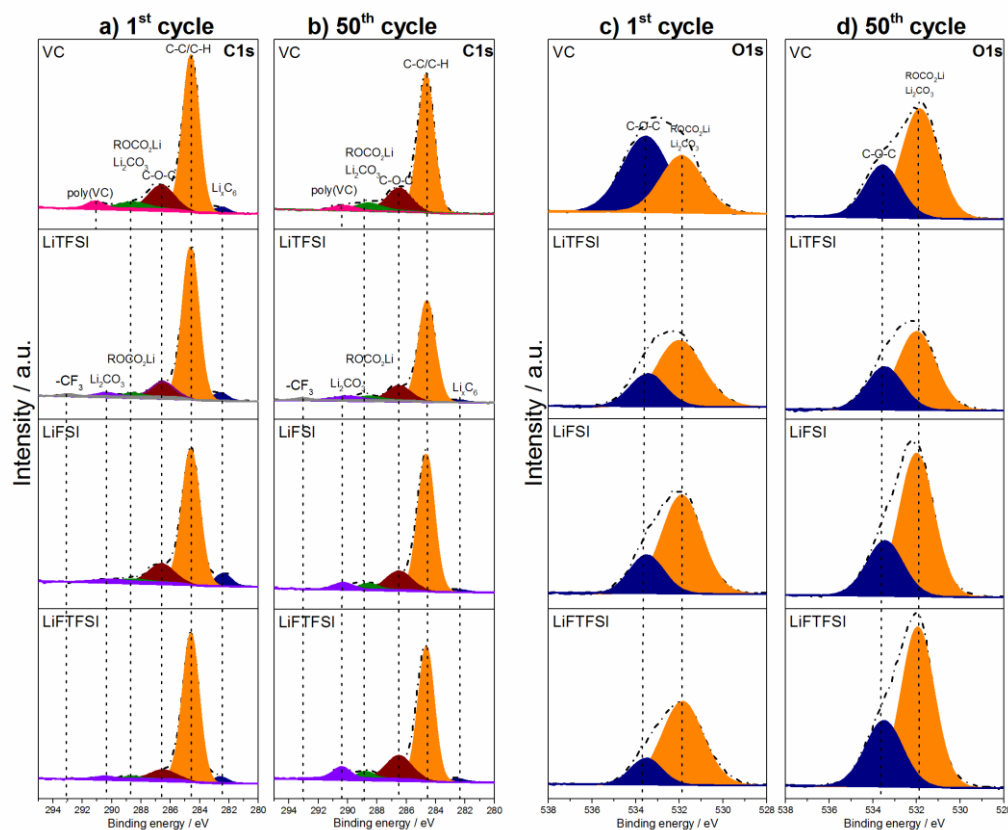
Figure 38. C1s (a and b) and O1s (c and d) XPS spectra recorded on the graphite electrodes after the 1st or the 50th cycle with different electrolyte mixtures (cf. description in the figures).

The main difference arising from the use of the three Li-imide salts is the peak at 293.2 eV detected only for LiTFSI. In literature this peak is attributed to the –CF$_3$ group in the pristine salt, indicating that TFSI$^-$ is present on the electrode surface [185-188]. After 50 cycles (Figure 38b) the C1s spectrum of LiTFSI remains almost unchanged and the characteristic peak of

pristine TFSI anion at 293.2 eV is retained. On the other hand, with all other electrolytes, the graphite surface becomes richer in carbonate species as confirmed by the increasing intensities of the corresponding peaks in the C1s and O1s spectra (Figure 38b and d), indicating a pronounced SEI formation upon cycling. It is also interesting to note that the intensity of the lithiated graphite species in Figure 38b decreases in all cases, due to a growth of the SEI layer with increasing charge/discharge cycle number.

The F1s spectra of graphite electrodes cycled in the various electrolytes are reported in Figure 39 (panels *a* and *b*). The peak at 686.8 eV is assigned to residual $LiPF_6$ from incomplete salt removal during the electrode rinsing and/or intermediate decomposition products (Li_xPF_y), whose binding energies are close to that of $LiPF_6$ [185]. The peak at 684.9 eV is attributed to LiF, the main decomposition product of $LiPF_6$ [182]. In the presence of Li-imide salts additional peaks are seen at 688.6 eV for LiTFSI and LiFTFSI and at 687.8 eV for LiFSI. These peaks are attributed to the pristine salts or their incomplete decomposition products [182, 183]. In the case of LiTFSI this peak is more pronounced, which is also supported by the detection of the –CF$_3$ peak in the C1s spectra. This indicates that this salt does not decompose completely. The electrochemical reduction of LiFSI via S-F bond cleavage with LiF formation has been already reported by Philippe et al. [183]. This can, therefore, explain the high amount of LiF in the SEI when LiFSI is introduced in the electrolyte. Surprisingly, upon cycling the electrode surface is enriched in LiF in the presence of LiTFSI, but not with LiFSI and LiFTFSI (Figure 39b).
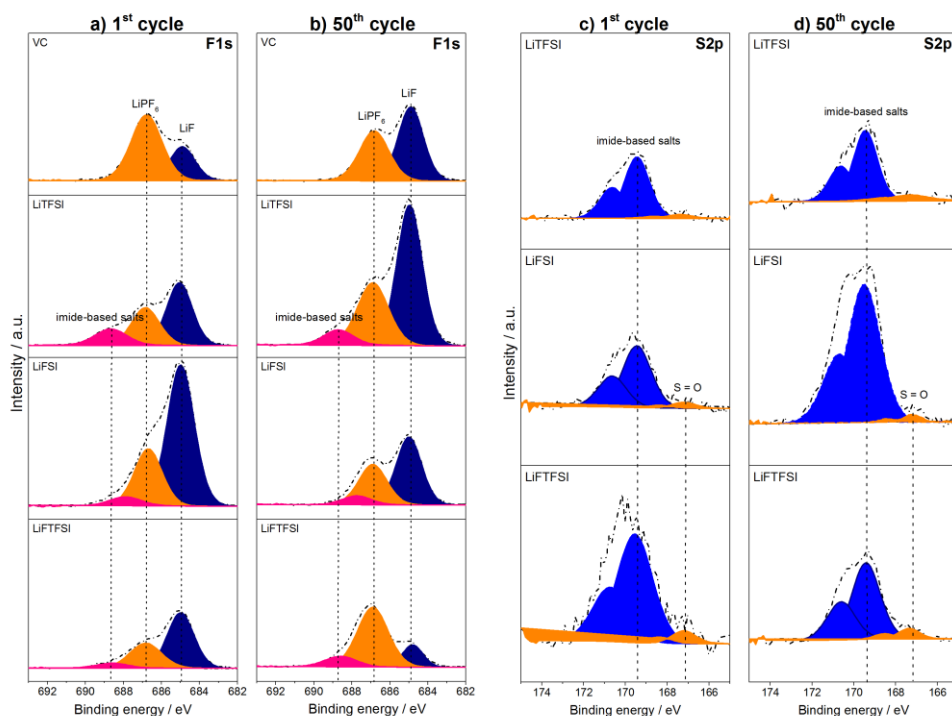
Figure 39. F1s (a and b) and S2p (c and d) XPS spectra of graphite electrodes after the 1st and the 50th cycle.

The P2p spectra of the cycled graphite electrodes after one lithiation-delithiation cycle are shown in Figure 40a. The doublet at 137 eV is assigned to the residual $LiPF_6$ and Li_xPF_y species, while the one at 134.2 eV is attributed to $Li_xPF_yO_z$ decomposition products. For the VC-added electrolyte no significant changes of the electrode XPS spectra are seen upon prolonged cycling (spectra after 50 cycles are shown in Figure 40b). For LiTFSI an increase of the $LiPF_6$ and Li_xPF_y contribution is observed after 50 cycles. When using LiFSI, the signal of $Li_xPF_yO_z$ is predominant after 1 cycle, indicating that a more pronounced salt degradation occurs with this electrolyte after the 1st cycle. However, after prolonged cycling both signals appear reduced. In the case of LiFTFSI, the peak associated with $LiPF_6$ at 137 eV increases upon cycling.

The signal in N1s spectra at 399.8 eV (Figure 40c), is attributed to the imide salts. After prolonged cycling (Figure 40d) an increased intensity is observed for LiFSI, which might further indicate its extended decomposition compared to other imide salts.
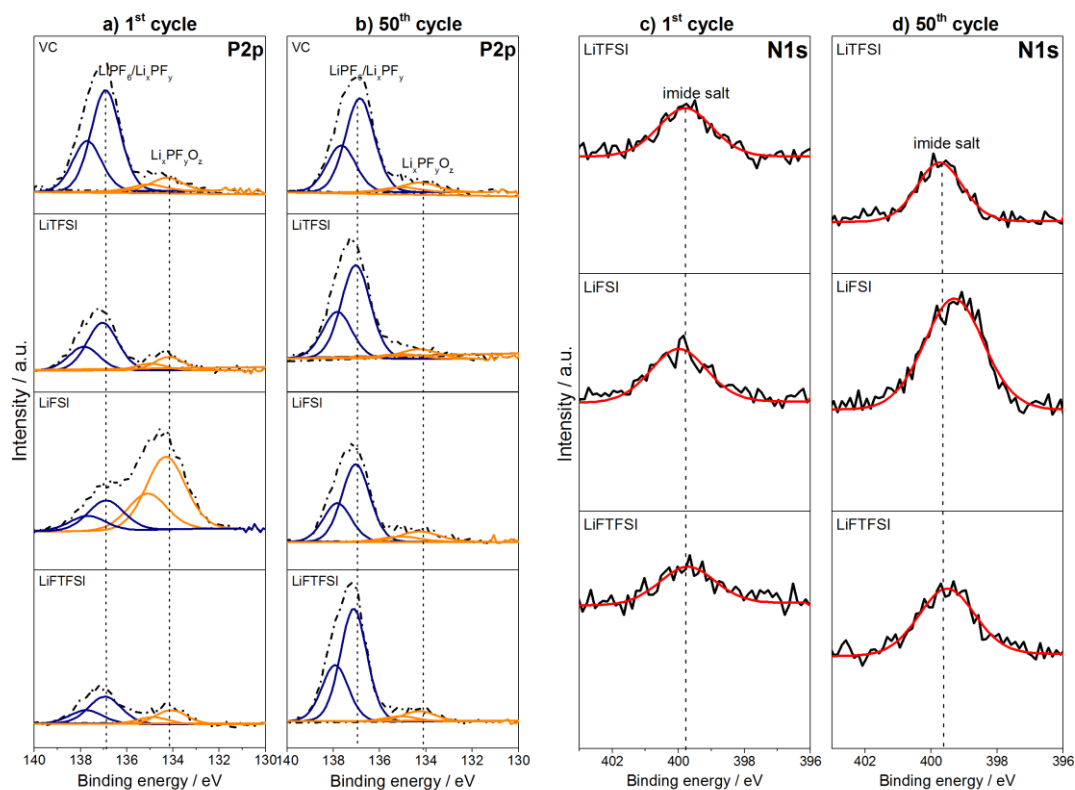
Figure 40. P2p (a and b) and N1s (c and d) XPS spectra of graphite electrodes in contact with the various electrolytes (see legend) after the 1st or 50th galvanostatic cycle.

The values of atomic concentrations of the chemical elements, present in the SEI, are reported in Figure A2 in APPENDIX 2, including their evolution upon sputtering. It should be noted that the signal at 282.5 eV in the C1s spectra is attributed to the lithiated graphite species (Li_xC_6) and, thus, is mostly related to the electrode active material (graphite) rather than to the SEI, as mentioned above. Therefore, the value of this signal was subtracted from the overall atomic

concentration of carbon. Additionally, a corresponding fraction of the Li concentration (calculated assuming a LiC_6 stoichiometry) was also removed.

The atomic content (%) of the SEI components (Figure 41) is useful to give an overall picture of the surface composition. The amount of carbonate species (both organic and inorganic ones) and PEO on the SEI after the 1st cycle decreases in the order VC>LiFSI>LiTFSI>LiFTFSI, while, in agreement with the previous discussion, LiF decreases in the order LiFSI>LiFTFSI>LiTFSI>VC. This indicates that the initial SEI formed in the presence of imide salts is richer in LiF as compared to that formed in the presence of VC. However, it should also be noted that besides anions, which can undergo the decomposition, Li^+ available from the imide salts dissociation can react with main salt anion PF_6^- or its decomposition products (such as PF_5 or POF_3) [182] and contribute to the total amount of LiF.

In fact, the SEI formation is not completed after one cycle, but continues during further cycling. After 50 cycles, the electrodes exposed to Li-imide salts have a higher amount of carbonates on their surface than that with VC. Furthermore, with respect to the 1st cycle, a decrease of LiF by 12% and 43% is found for LiFSI and LiFTFSI, respectively, while 9% more LiF is present when using LiTFSI. Still, except for the LiFTFSI-containing electrolyte, the main component of the SEI layer is LiF also after 50 cycles.

The variation of the atomic concentrations upon sputtering gives additional information about changes in the SEI composition with increasing depth. For the electrodes subjected to the 1st cycle only the Li_xC_6 beneath the SEI layer gives a more intense signal in the case of imide salts than for VC after 3 minutes of sputtering (Figure 41a). This suggests that the passivation layer with VC additive is initially thinner. Upon cycling the SEI is growing and after 3 min of sputtering all electrodes, subjected to 50 cycles, show almost the same atomic concentration of Li_xC_6 (Figure 41b). The carbonates and PEO contents decrease, showing that they are present in the most outer part of the passivation layer. Although it seems that the inner part of the SEI is rich in LiF, as its content increases after 3 minutes of sputtering, it should be kept in mind that LiF can be also formed upon Ar^+ etching [189].
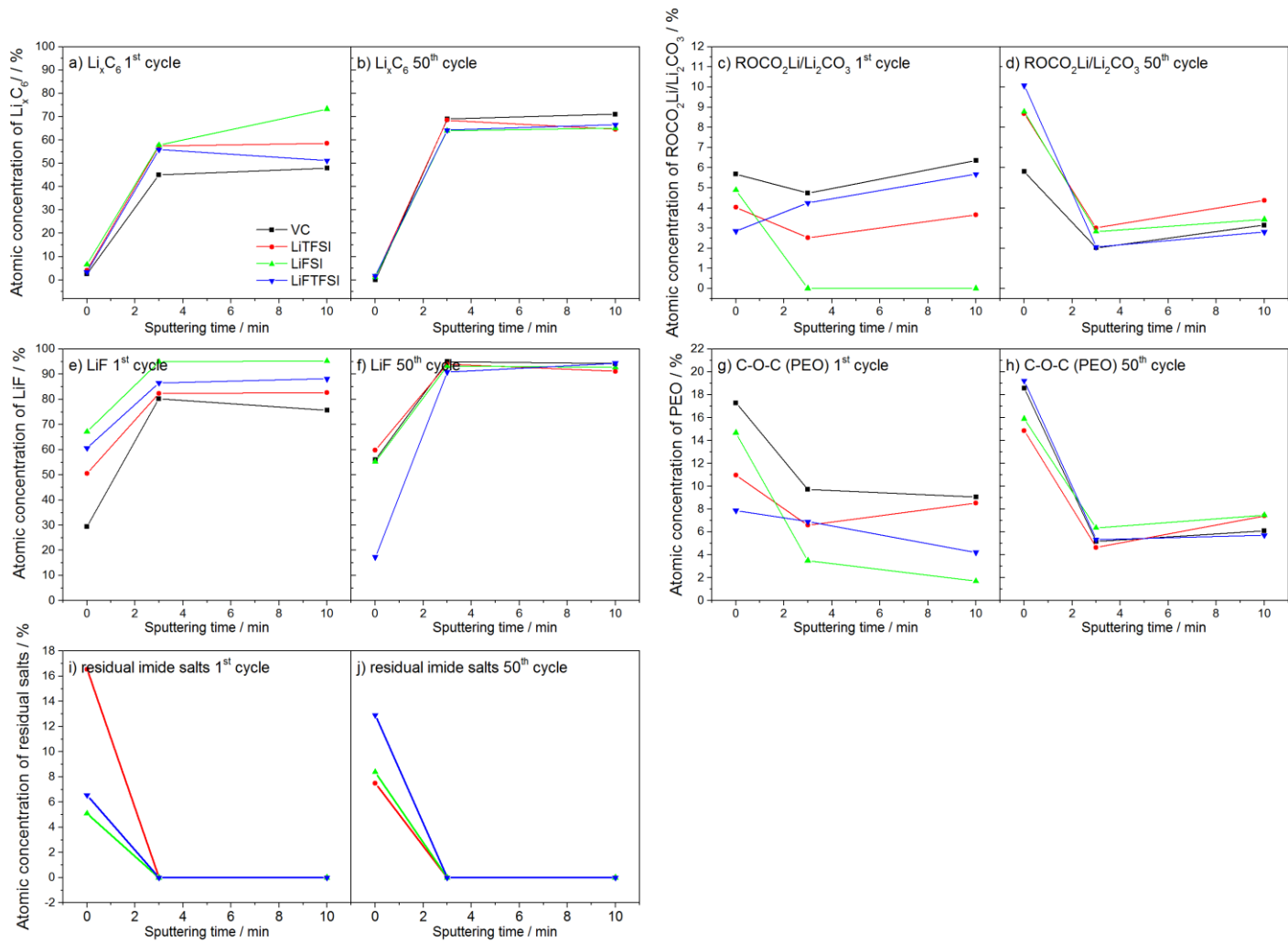
Figure 41. Evolution of the atomic concentrations of the SEI components on graphite electrodes in contact with the various electrolytes (see legend) as a function of sputtering time after the 1st or 50th galvanostatic cycle.

It is known that insoluble LiF and Li_2CO_3 are rather stable SEI components, however, providing insufficient Li^+ ion conduction. Recently, the synergetic effect of LiF and Li_2CO_3 in the SEI of Si anodes has been reported by Zhang et al. [190]. In particular, albeit LiF and Li_2CO_3 have relatively low intrinsic ionic conductivity, charge accumulation occurs at their grain boundaries, which promotes Li^+ ion conduction and further stabilizes the SEI itself. Interestingly, the higher was the LiF content (up to 15%), the lower was the 1st cycle irreversible capacity and the better was the rate capacity and the long-term capacity retention of the Si anode, in line with our results.

To summarize, the XPS results revealed that the SEI obtained on the graphite surface after one cycle is thinner and richer in LiF when Li-imide salts rather than VC are used as additives. In all cases the passivation layer grows upon cycling, however, containing more organic and inorganic lithium carbonates in the topmost layers when the imide salts are added to the electrolyte.

4.2.3   *Electrochemical impedance spectroscopy of Li/graphite cells*

The SEI composition and thickness obviously affect the impedance of the graphite electrodes. The EIS spectra, recorded at specific potentials, are shown in Figure 42. The graphite electrodes were subjected to slow (C/20) lithiation. The impedance measured at open circuit potential (OCP), 0.7 V *vs* Li/Li^+ (after reduction of the additive/salt), 0.5 V *vs* Li/Li^+ (after solvent reduction) and in the fully lithiated state are illustrated in Figure 42a-d.
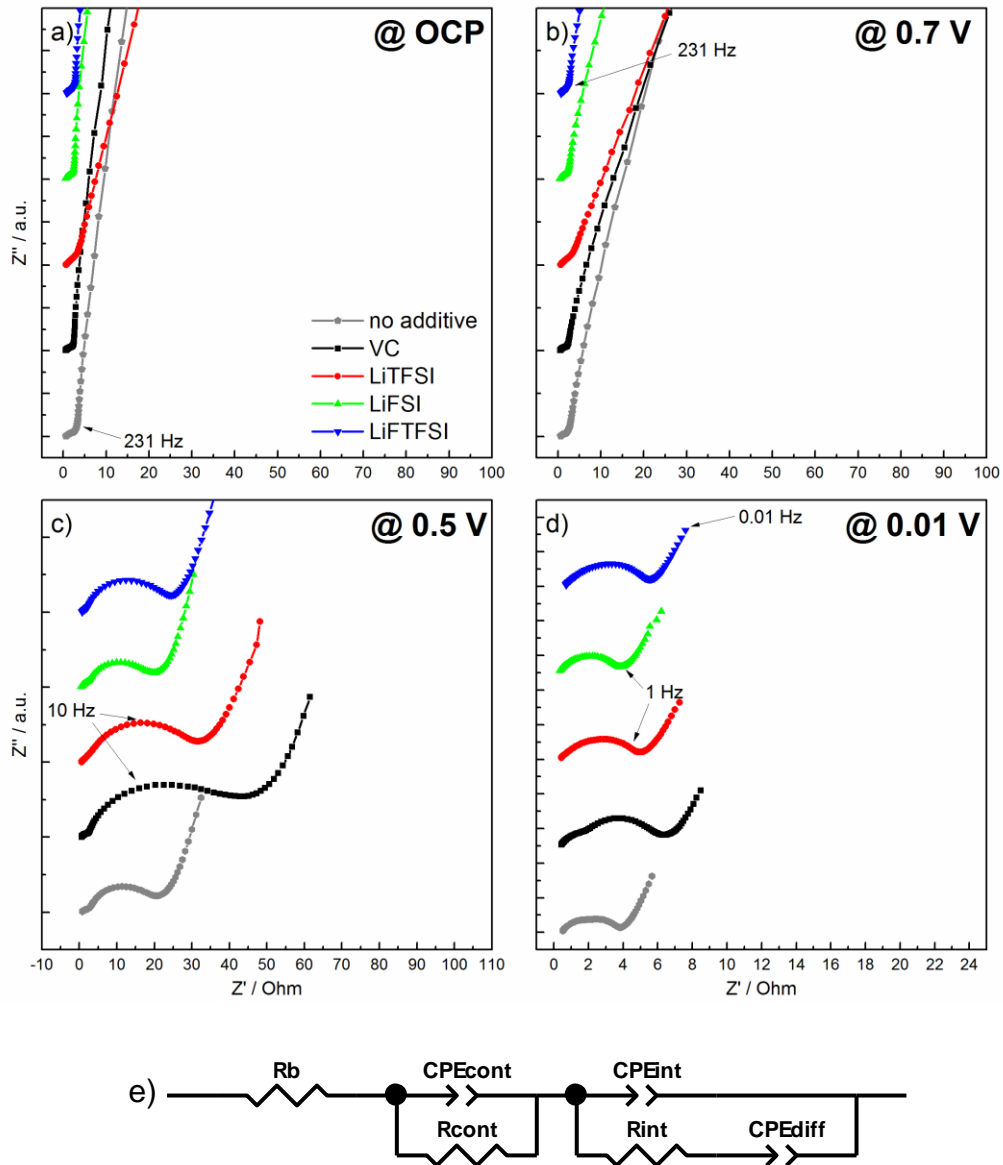
Figure 42. Nyquist plots of graphite electrodes at a) OCP, b) 0.7 *vs* Li/Li$^+$, c) 0.5 *vs* Li/Li$^+$, d) 0.01 V *vs* Li/Li$^+$ and e) equivalent circuit model used for the fitting at 0.5 and 0.01 V *vs* Li/Li$^+$. The measurements were performed on three-electrode EL-cells with Li metal as RE and CE. Electrode area: 2.54 cm^2.

At the OCP (Figure 42a) only one open semicircle is observed in the high-to-middle frequency range. As previously proposed in literature, this depressed semicircle arises from the resistances which can be linked, for example, to particle-particle and particle-current collector contacts [191, 192]. The depressed shape of the semicircle might, furthermore, arise from electrode porosity and inhomogeneous surface roughness. In the lower frequency range, where likely no faradaic reactions occur at this potential (ca. 3 V *vs* Li/Li$^+$), the graphite electrode approaches the blocking-electrode behavior [193, 194].

At 0.7 V *vs* Li/Li$^+$ (Figure 42b), the reductive decomposition reactions are initiated by electrolyte solvents and LiPF$_6$, as indicated by the broad peak in the differential capacity plot in the inset of Figure 34c. Furthermore, VC decomposition takes place at this potential [134].

Here, the impedance response of graphite electrodes cycled with different electrolytes does not substantially differ from those recorded at the OCP indicating that, if formed, the SEI is very porous and permeable to the electrolyte.

At 0.5 V *vs* Li/Li$^+$ (Figure 42c), besides the high frequency semicircle associated with contact resistance, a new element in the middle-frequency range appears for all electrodes. At this potential, according to the differential capacity plot, the electrolyte reduction should be mostly completed, but the typical staging intercalation into graphite has not started yet. Therefore, it is reasonable to attribute this new semicircle to the freshly formed SEI and Li$^+$ (charge) transfer at the interface. The separation of these contributions is, unfortunately, hindered by the considerable overlapping of the two semicircles probably due to their very similar time constants.

In the fully lithiated state (at 0.01 V *vs* Li/Li$^+$), the same semicircles can be observed in Figure 42d. The semicircles related to the interfacial resistance are smaller for all electrolytes as compared to the responses at 0.5 V *vs* Li/Li$^+$. This might be related to the reconstruction of the SEI upon further graphite electrode polarization with formation of the inorganic species, which have high ionic and low electronic conductivity [13, 193]. Additionally, charge transfer through the completed SEI is faster, also contributing to the shrinkage of the spectra in the fully lithiated state [195].

Figure 42e shows the equivalent circuit model used for fitting the spectra at 0.5 and 0.01 V *vs* Li/Li$^+$. It consists of a resistor (intercept with the real axis Z') describing the bulk resistance of the cell (R$_b$), mostly accounting for the electrolyte contribution [193, 194] and two R|Q elements connected in series. The first R|Q element is constituted by a resistor (R$_{cont}$) in parallel with a constant phase element (CPE$_{cont}$), accounting for the various contact issues described above. The second R|Q element, also consisting of a resistor (R$_{int}$) and a constant phase element (CPE$_{int}$) in parallel, is attributed to the interfacial processes previously mentioned (SEI and charge transfer). To compensate for the non-ideal behavior, the straight line at low frequencies attributed to the lithium ion diffusion into graphite is also modeled with a constant phase element (CPE$_{diff}$) rather than with a Warburg element.

As shown in Table 6, at 0.5 V *vs* Li/Li$^+$ the VC-containing electrolyte shows the highest R$_{int}$, which is related to the formation of the polymeric surface film upon the additive decomposition, confirming the prediction of a more resistive SEI from the voltage profile in Figure 34c. Interestingly, the interfacial resistance of the bare electrolyte at this potential is comparable to that of the LiFSI-containing one, thus indicating the formation of a more ionically conductive SEI. In the fully lithiated state a sharp decrease in the impedance is observed, which is mostly

related to the higher electronic conductivity of the Li-intercalated graphite [196], and reconstruction of the SEI. The smallest interfacial resistance of the bare electrolyte at 0.01 V *vs* Li/Li$^+$ might be related to the high amount of carbonates on the surface, as determined by XPS, which are known to possess higher ionic conductivity than LiF [190]. In case of imide salts the interfacial resistances are comparable to that obtained in presence of VC with slightly lower value for LiFSI-containing electrolyte.

Table 6. The interfacial resistances determined by EIS at 0.5 and 0.01 V *vs* Li/Li$^+$ with various electrolytes.

Electrolyte	R$_{int}$ at 0.5 V *vs* Li/Li$^+$, Ohm	R$_{int}$ at 0.01 V *vs* Li/Li$^+$, Ohm
LP30	19	2.8
LP30 + 2 wt% VC	39	4.6
LP30 + 2 wt% LiTFSI	30	4.6
LP30 + 2 wt% LiFSI	18	3.7
LP30 + 2 wt% LiFTFSI	22	4.8

4.2.4 Thermal behavior of lithiated graphite in contact with electrolytes

The thermal stability of the SEI is of great importance for the battery safety. The thermal decomposition of the SEI may lead to uncontrolled exothermic reactions between the anode and the electrolyte, possibly resulting in a thermal runaway of the cell. Figure 43 shows the DSC profiles of the pristine and electrochemically lithiated in the presence of the various electrolytes graphite electrodes. The pristine electrode is stable up to 300 °C, which is related to the small amount of CMC binder and SBR (4% in total), which are degrading above ~240 °C [197, 198]. For the bare electrolyte a weak exothermic peak is observed at around 140 °C with a slight change of the baseline (marked as "1"). This peak has been attributed to the rupture of the SEI layer, leading to further reactions between the electrolyte and the lithiated graphite [40-42]. Using VC as additive, this peak becomes broader. In the case of LiTFSI, the onset of SEI cracking is almost unchanged, while for LiFSI and LiFTFSI it occurs at slightly lower temperatures. Furthermore, in the case of LiFTFSI, two distinct thermal events can be distinguished at this temperature. Above 230 °C, a broad exothermic peak (marked as "2"), followed by a sharp intense peak (marked as "3") are observed, which are related to the thermal decomposition of the electrolyte and SEI breakdown [41]. Using VC, the intensity of peak "3" is lower, which is in line with the results of other studies reporting that VC-derived SEIs are more thermally stable than those formed in the VC-free electrolytes [10, 11]. When LiTFSI is used, the onset of these reactions is shifted to lower temperatures. Furthermore, the intensity of peak "2" increases for the electrolytes containing imide salts compared to pure LP30 and VC-

containing ones. Overall, this behavior indicates that the thermal stability of the lithiated graphite anode is slightly reduced by the addition of Li-imide salts in the electrolyte with respect to the pristine or VC-doped electrolytes. The total heats reported in Table 7 show that more energy is released above 230 °C using the imide salts as compared to VC. However, additional investigations are necessary to explore in-depth the synergetic effect of including simultaneously VC and Li-imide salts in the electrolyte formulation to balance the beneficial properties of these additives.
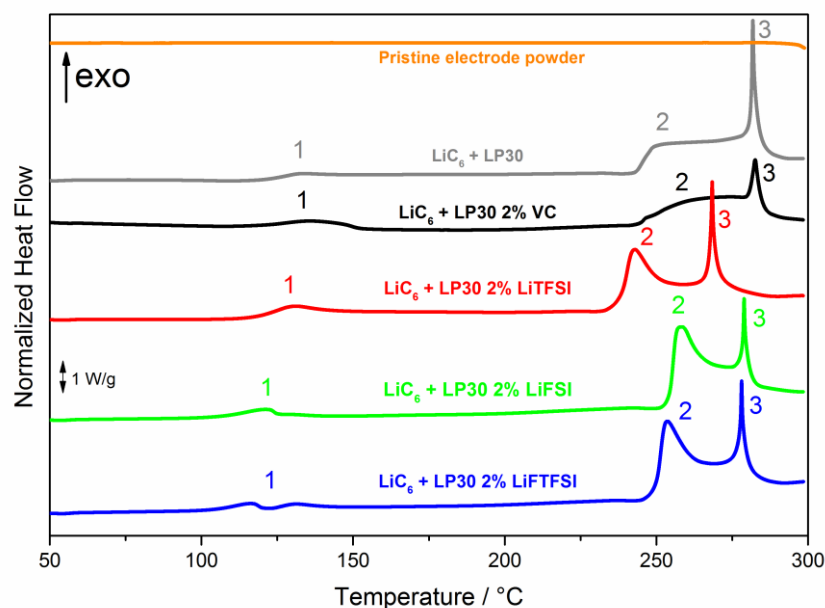
Figure 43. DSC traces of lithiated graphite electrodes in contact with the different electrolytes stated in the figure.

Table 7. Heat generated upon heating lithiated graphite electrodes in the electrolytes.

Electrolyte	1st peak, J/g	2nd + 3rd peaks, J/g	Total, J/g
LP30	16	468	484
LP30 + 2 wt% VC	56	366	422
LP30 + 2 wt% LiTFSI	45	499	544
LP30 + 2 wt% LiFSI	49	506	555
LP30 + 2 wt% LiFTFSI	38	541	579

4.2.5 Investigation on LiPF$_6$-LiTFSI mixture (total concentration of 1M)

To shed light on the origin of higher LiF amount on graphite anode SEI, detected by XPS, when using the electrolyte with LiTFSI (a relatively stable salt compared to LiPF$_6$ and other imide salts) additional measurements were conducted. For this purpose the electrolytes with 1M total concentration of Li$^+$ obtained using different molar ratios of LiPF$_6$ and LiTFSI (0.9:0.1, 0.8:0.2 and 0.7:0.3, respectively) in EC:DMC (1:1, v/v) were prepared. Indeed, the additional Li ions provided by the imide salt can further react with PF$_6^-$ anion (or its decomposition products), following the reactions:

$$PF_6^- + 3Li^+ + 2e^- \rightarrow 3LiF\downarrow + PF_3\uparrow \qquad (4.1)$$

$$PF_5 + 2xLi^+ + 2xe^- \rightarrow Li_xPF_{5-x}\downarrow + xLiF\downarrow \qquad (4.2)$$

$$POF_3 + 2xLi^+ + 2xe^- \rightarrow Li_xPF_{3-x}O\downarrow + xLiF\downarrow \qquad (4.3)$$
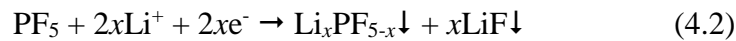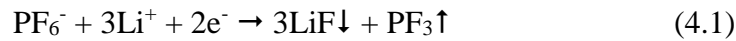
Thus, the amount of LiF produced can substantially increase. Limiting the total Li ion concentration to 1M permits to eliminate this additional contribution. The graphite electrodes were subjected to one charge/discharge cycle in coin cells with Li metal counter electrode and analyzed via XPS. Same cycling and washing procedure was applied to the graphite electrodes, as described in Section 3.9. To better appreciate differences in the SEI composition, the XSP data on the graphite electrode, subjected to one cycle in pristine LP30 electrolyte was added to the analysis.

The F1s XPS spectra of the delithiated graphite electrodes cycled with different electrolytes are shown in Figure 44a-d. The spectra were normalized to the total area of the peaks, obtained with LP30. Compared to bare electrolyte (panel *a*), the addition of LiTFSI leads to substantial increase in LiF signal (green peak at lower binding energy), highlighted in the bar chart in Figure 44e. Increasing the amount of LiTFSI results in the growth of LiF signal by 6-7 at%, but, interestingly, there is no linear trend. Furthermore, the atomic concentration of the pristine imide salt (blue peak at higher binding energy in Figure 44b-d), increases as well. This might indicate that LiTFSI undergoes only limited decomposition upon graphite polarization, probably induced by traces of impurities from the synthetic process or water residuals due to its hygroscopic properties. On the other hand, it would be expected that the amount of LiF would linearly increase with a higher LiTFSI content, as LiF is one of the products of PF$_6^-$ anion reaction with water. Although at present this behavior is not well-understood, the increase in LiF amount can be mostly attributed to the decomposition of LiPF$_6$.
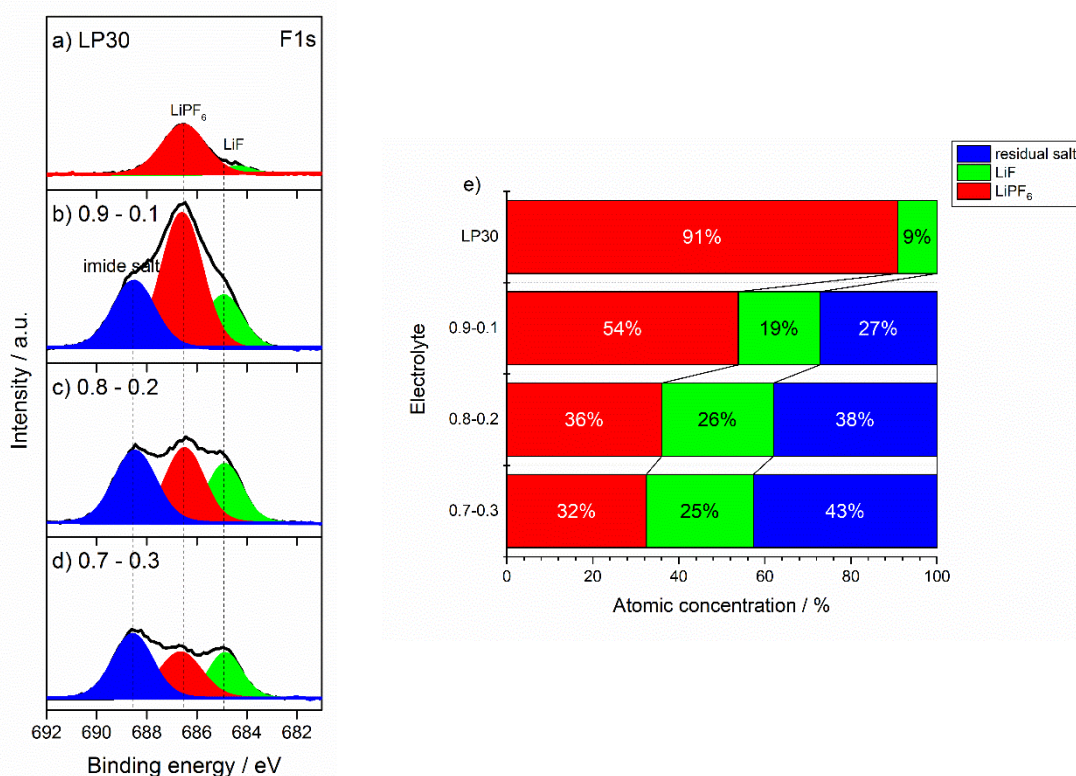
Figure 44. F1s XPS spectra (a-d) of the delithiated graphite electrodes with various electrolytes and e) atomic concentrations of corresponding SEI components after the 1st cycle.

To verify this hypothesis Figure 45 shows the variation of the atomic concentrations of another $LiPF_6$ decomposition product, i.e., $Li_xPF_yO_z$ analyzed using the P2p XPS spectra. It can be noticed that $Li_xPF_yO_z$ amount is higher in presence of LiTFSI as compared to bare LP30, supporting the initial speculation of LiTFSI promoting the decomposition of $LiPF_6$. However, it is reported that the increase in the amount of fluorophosphates and LiF can partially originate from the sample preparation [189]. On the other hand, for the three samples obtained from imide-containing electrolytes $Li_xPF_yO_z$ and LiF amounts are considerably higher with respect to the bare electrolyte. This excludes that their source is only or predominantly due to the sample preparation, which was the same for all electrodes (and as accurate as possible to avoid contact with ambient atmosphere).
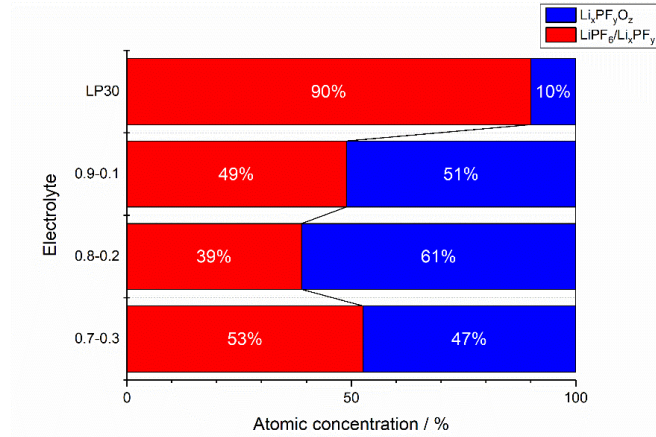
Figure 45. Atomic concentrations of SEI species from P2p XPS spectra on delithiated graphite electrodes cycled with various electrolytes after the 1st cycle.

The possible decomposition of LiTFSI upon cathodic polarization was discussed by several authors. Borgel et al. [199] proposed the reduction of TFSI anion (total salt concentration of 1M) in presence of Li ions in the ionic liquid electrolyte with the formation of insoluble salts, such as LiF, Li_xSO_y, $Li_2NSO_2CF_3$, and Li_xCF_y. These species could precipitate on the surface of the electrode and form the SEI. Eshetu et al. [182] suggested that the formation of LiF in presence of 1M LiTFSI in the mixture of cyclic and linear carbonates might result from the reduction of the salt impurities or through the salt reduction at very low potentials, following the reaction:

$$LiN(SO_2CF_3)_2 + ne^- + Li^+ \rightarrow Li_3N + Li_2S_2O_4 + LiF + C_2F_xLi_y \qquad (4.4)$$
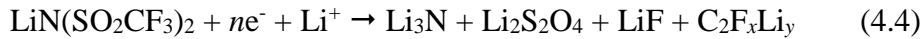
More pronounced decomposition of LiTFSI was observed at higher salt concentration (typically above 3M). The studies show that at higher salt concentration the salt anion could enter the solvation shell of Li ions [200]. Upon intercalation the salt anion was reduced to higher extent than the solvents, and the decomposition products of the anion participated in the SEI formation. However, at lower salt concentrations (i.e., below 0.5M) this process is hardly probable.

It is expected that higher amount of LiF in the SEI should increase its resistance due to the low ionic conductivity of this salt ($\sim10^{-31}$ S cm^{-1}) [201]. Therefore, impedance spectroscopy analysis was conducted in the same manner, as in Section 4.2.3. Only two electrolytes with LiTFSI concentrations of 0.1 and 0.3M were considered in this study and compared with the EIS results obtained using bare electrolyte. The spectra, obtained at different potentials upon graphite lithiation, are shown in Figure 46.
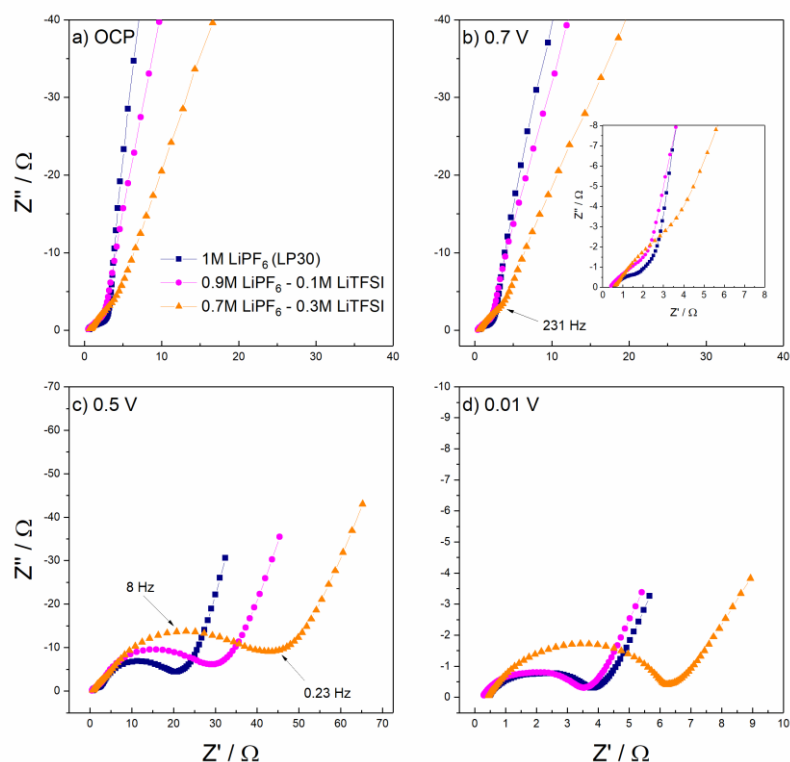
Figure 46. EIS spectra of the graphite electrodes measured at a) OCP, b) 0.7 with an inset, showing the high-frequency semicircle, attributed to contact issues, c) 0.5 and d) 0.01 V *vs* Li/Li$^+$ with electrolytes, containing various LiPF$_6$:LiTFSI molar ratios. Electrode area: 2.54 cm².

In line with the results shown in Section 4.2.3, the spectra at OCP and 0.7 V *vs* Li/Li$^+$ are very similar (Figure 46a,b), indicating no SEI formation also at the higher LiTFSI concentration. The contact resistance at OCP and 0.7 V *vs* Li/Li$^+$ is significantly higher with both 0.1 and 0.3M of LiTFSI than that with LP30. At present this phenomenon is not fully understood and would require further investigation. Nevertheless, the main purpose of the EIS measurements was to monitor the change in the interfacial resistance upon potential decrease. At 0.5 V *vs* Li/Li$^+$ and in the fully lithiated state (Figure 46c,d) the interfacial resistance with 0.3M of LiTFSI is almost double of that with 0.1M LiTFSI (27 *vs* 39 and 2.7 *vs* 4.2 Ω, respectively). When comparing these results with the ones from Section 4.2.3, it might be seen that with 2 wt% LiTFSI (corresponding to ~0.06M) the higher interfacial resistance is observed probably due to the higher total Li$^+$ concentration, leading to the complementary LiF formation. However, when the total concentration of Li ions is fixed to 1M the similar values of interfacial resistance are observed with LP30 and the electrolyte with 0.1M LiTFSI in the fully lithiated state.

The cell performance of the full graphite/LFP cells, using either 0.1 or 0.3M LiTFSI-containing electrolytes was compared to that with pristine LP30. Figure 47a shows the results of the C-rate test followed by the constant current cycling at 1C. Slightly higher rate capability at higher

LiTFSI content is observed probably due to the higher ionicity of LiTFSI than $LiPF_6$ in EC/DMC media [131]. However, increased capacity fading is observed at higher LiTFSI concentration. The 1st cycle efficiency increases with the increase of LiTFSI content, yielding 88.4%, 91.1% and 91.9 % for LP30, 0.9:0.1 and 0.7:0.3, respectively. In the voltage profiles, displayed in Figure 47b, the SEI formation (up to ~3.26 V) with addition of LiTFSI consumes less charge capacity, although, the resulting capacity with LP30 electrolyte is slightly higher. Furthermore, the voltage profiles of the cells with 0.3M LiTFSI electrolyte show slightly higher polarization, which might be attributed to the formation of a more resistive SEI in line with the EIS results. The higher coulombic efficiency and lower charge capacity, required for the SEI build-up in presence of LiTFSI might indicate that it acts as a sacrificial salt, supplying the Li ions for the SEI formation.
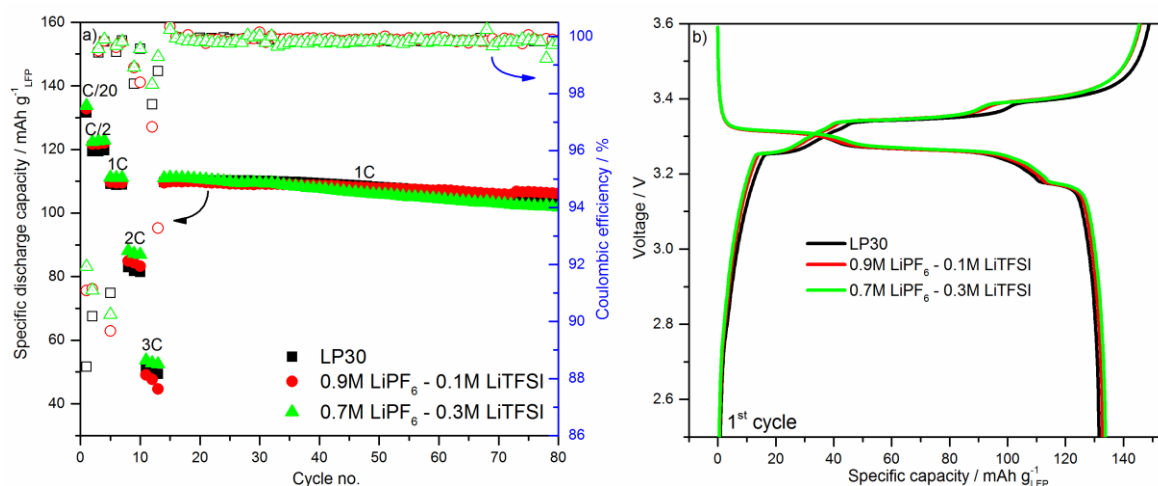
Figure 47. a) C-rate followed by cycling test and b) 1st cycle voltage profiles of the full graphite/LFP cells with different $LiPF_6$:LiTFSI molar ratios in the electrolytes.

4.2.6 Conclusions

The results of this section show that the use of Li-imide salts as electrolyte additives is beneficial for the long-term cycling stability of graphite/$LiFePO_4$ cells. At 20 °C, LiTFSI reduces the capacity retention by only 2% after 600 cycles, while the control cell with VC loses 20% of the initial capacity. Moreover, the 1st cycle coulombic efficiency is improved in presence of imide salts with respect to that obtained using VC additive. The presence of imide-based Li salts in the electrolyte does not shrink the electrochemical stability window but the resulting SEI is less thermally stable than that obtained using VC. Detailed XPS and EIS investigation were conducted to explain the role of the imide salt on the SEI formation on the graphite anode. XPS analysis reveals that with Li-imide salts thin LiF- and carbonates-rich SEI layers on the graphite electrode are obtained. For these electrodes impedance spectroscopy evidences that the SEI resistance is lower than the one originating from the electrolyte with VC

additive but higher than that obtained with bare LP30. Therefore, it can be inferred that the higher amount of LiF formed in presence of imide salt with respect to VC is the origin of the improved cell performance. While no doubt on the susceptibility to cathodic decomposition exists for LiFSI and LiFTFSI, the source of extra LiF in the case of LiTFSI was unclear. Therefore, additional electrolytes with 1M Li^+ concentration and different ration of $LiPF_6$ and LiTFSI were investigated. From the results in Section 4.2.5 it appeared that LiTFSI decomposes only partially and an excess of this salt (0.3M) does not result in the additional LiF formation but rather in the increased electrode resistance. Therefore, it seems that LiTFSI promotes the decomposition of $LiPF_6$, leading to higher amount of LiF when both salts are present simultaneously in the electrolyte. This study also evidences that, although the higher LiF content with respect to LP30 increases the interfacial resistance, the addition of LiTFSI leads to the higher 1st cycle efficiency in full cells, suggesting that it acts as a sacrificial salt and provides extra Li for SEI build-up.

4.3   Impact of the formation protocols on the graphite SEI characteristics and performance of Li-ion batteries

The use of electrolyte additives is not the only possible way to influence the formation of a stable SEI on the graphite surface. The formation step (formation protocol or simply formation) itself, which generally refers to the first charge/discharge followed by 3-4 additional cycles, has a significant impact on SEI build-up and growth. Formation generally represents a production bottleneck, since it is a time-consuming and cost-ineffective process. Therefore, accelerating the formation step is a highly desirable goal. Unfortunately, each battery manufacturer works independently to develop the most advantageous formation protocol and keeps research activities confidential. This limits the amount of available literature to compare different protocols and evaluate the influence of the different parameters (e.g., current density, rest time, or temperature) on the SEI formation and cell capacity retention.

In the next subchapter a dual-current formation protocol is compared to a lab standard one and the protocol applied by a battery manufacturer (for simplicity called "industrial"). To analyze the effect of the formation step galvanostatic cycling, impedance spectroscopy, transmission electron microscopy (TEM), and post-mortem XPS surface analysis of graphite electrodes were employed. The dual-current formation protocol was proposed by Dr. Iratxe de Meatza (CIDETEC, Spain). The source of the industrial protocol is EU-funded project SPICY. The HRTEM images were obtained and analyzed by Dr. Adrien Boulineau (CEA-LITEN, France).

4.3.1   Evaluation of the formation protocols in half Li/graphite cells

4.3.1.1   Lab standard protocol

The lab standard formation protocol consists of a single cycle at a constant current density with a constant voltage step at the end of charge (lithiation). Initially, the study focused on the influence of the used C-rate on the electrochemical performance of graphite anodes. A variety of C-rate values in the 1st cycle were used: C/100, C/50, C/20, C/10, and C/5 (1C = 372 mA g^{-1}), aiming to evaluate the optimum one. The cycling procedure is fully described in Table A2a (APPENDIX 1). LP30 electrolyte with addition of 2 wt% FEC was used due to the beneficial influence of this additive on the formation of SEI and cycling stability, as pointed out by various research groups [114, 116, 202, 203]. The results of the rate capability test followed by constant current cycling at C/2 and the 1st cycle voltage profiles are shown in Figure 48.
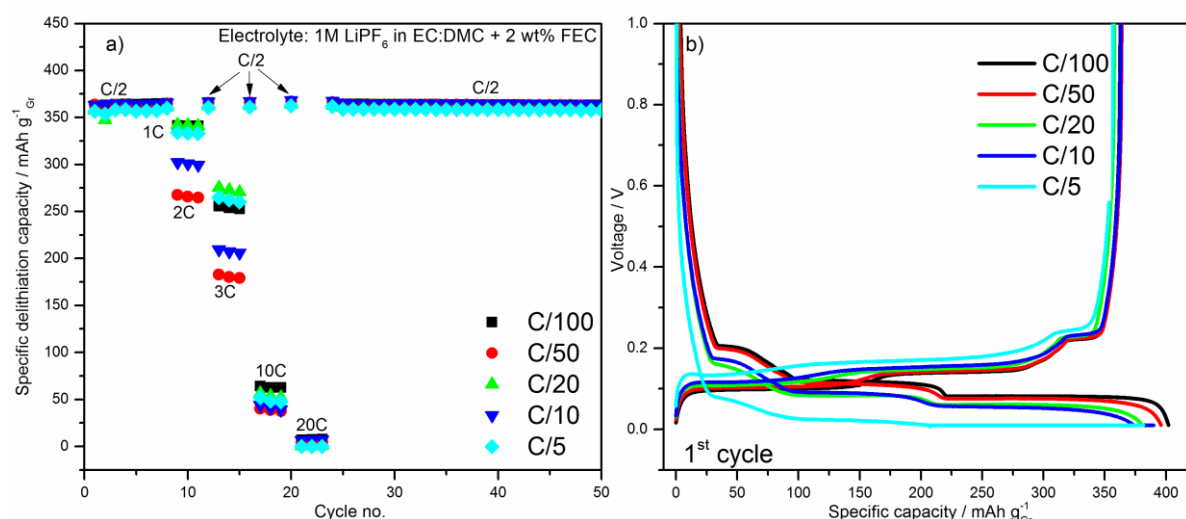
Figure 48. a) Rate test and cycling performance and b) voltage profiles of the formation cycle obtained at different rates using 1M LiPF$_6$ in EC:DMC (1:1, v/v) + 2 wt% FEC as electrolyte.

At 2C and 3C (Figure 48a) the electrodes initially cycled at C/100 (3.7 mA g^{-1}), C/20 (18 mA g^{-1}) and C/5 (74 mA g^{-1}) display comparable capacities, while for the others the delivered capacity is considerably lower. This suggests that the rate capability is not influenced by the conditions used for the 1st cycle. Furthermore, the relation between formation rate and rate capability is not linear but there is rather one (or more) optimum value. On the other hand, for the 1st cycle efficiency, reported in Table 8, the trend complies with an increase in coulombic efficiency with higher current density. Consequently, SEI formation at higher rates leads to the lower lithium consumption.

Table 8. Summary of the 1st cycle efficiencies and delivered capacities at 3C using different current densities during the formation cycle.

C-rate	1st cycle efficiency, %	Delivered delithiation capacity at 3C, mAh g^{-1}
C/100	90.2	235
C/50	91.9	197
C/20	92.9	270
C/10	93	209
C/5	93.4	260

The hysteresis for the voltage profiles in Figure 48b is minimal for C/100 and C/50, slightly higher for C/20 and C/10 but significantly higher for the cycle performed at C/5. Such hysteresis is probably linked with the formation of a more resistant SEI, as also reported in [13, 204]. This was ascribed to the formation of a large lithium concentration gradient, leading to the isolation

of some carbon particles and increasing the cell impedance. An incomplete, non-uniform and electrochemically unstable SEI has a detrimental effect on the battery cycle life and safety [13, 204, 205]. Furthermore, in the 1st cycle at C/5 the constant current charge contributed with only ~210 mAh g^{-1}, while the rest of the capacity was obtained during the constant voltage step. Moreover, the typical series of plateaus upon Li insertion into graphite was not observed below 0.2 V. All this indicates that C/5 rate is too high and the intercalation occurs too far from the thermodynamic equilibrium [206].

The differential capacity curves (Figure 49) show that a more pronounced electrolyte decomposition takes place at slower rates (C/100 and C/50). Instead, at C/5 the peak related to the electrode decomposition at ~0.65 V is barely distinguishable. This peak totally disappears in the following cycles (Figure A3, APPENDIX 2), suggesting that the formed SEI is able to prevent continuous electrolyte decomposition on the electrode surface.

Figure 49. Differential capacity plot of the formation cycles at different current densities using 1M LiPF$_6$ in EC:DMC (1:1, v/v) + 2 wt% FEC.

As the galvanostatic tests were only conducted in the half cells, the detrimental effect of a too high current density during the formation step on the cyclability might be hidden due to the large lithium reservoir in the system, which can be continuously consumed for the SEI rebuilding. Overall, C/20 seems to be the optimum current density to use for the lab standard protocol.

4.3.1.2   Dual-current formation protocol

The second protocol, called dual-current, aims to decrease the time required for the formation. However, a faster procedure should be designed, so that it does not deteriorate the long-term cycling performance of the cells. Therefore, the dual-current formation protocol keeps charging

the anode at C/20 till the voltage reaches 0.2 V. This is the value at which the SEI formation can be considered almost completed. Below 0.2 V the intercalation of Li$^+$ in between the graphene layers begins and the charge rate is increased to either C/10 or C/5 and maintained for the subsequent discharge. This protocol allows a substantial time saving compared to the lab standard protocol, as seen in Table 9. Herein, the influence of the additive amount is also tested, lowering the content of FEC to 1 wt%. The results of the Li/graphite cells cycling and the 1st cycle voltage profiles with the relative differential capacity plots are reported in Figure 50.
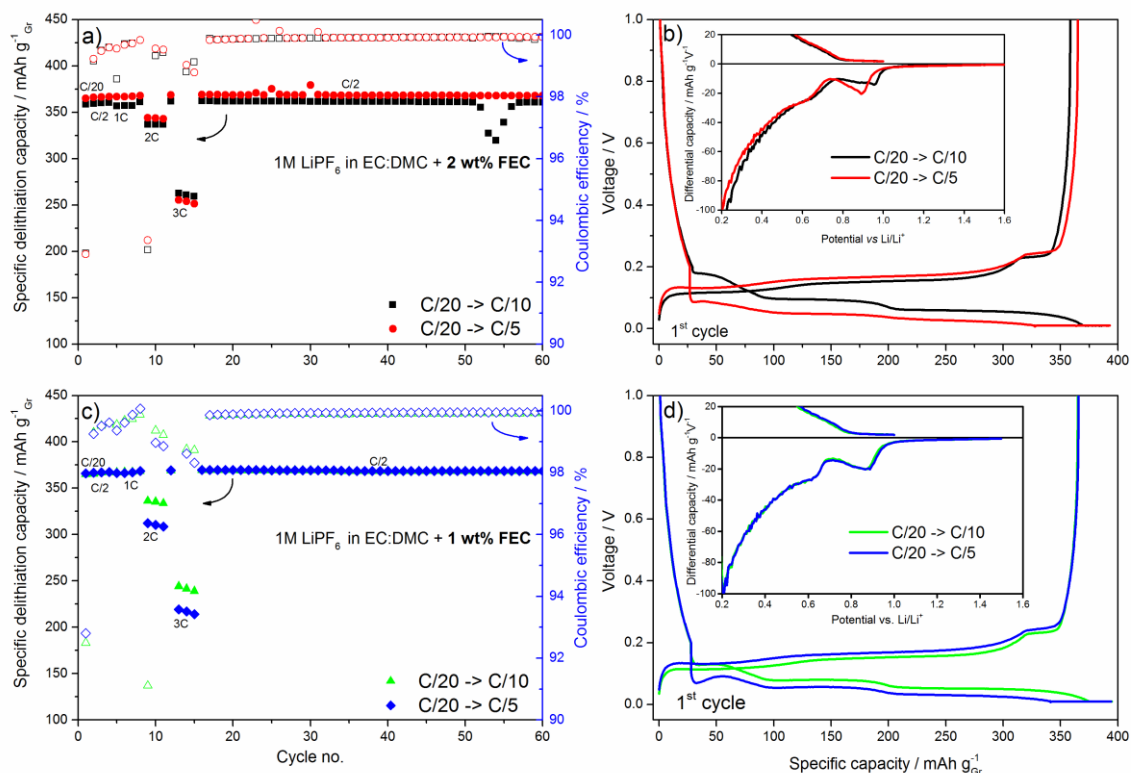
Figure 50. Cycling performance of the half Li/graphite and voltage profiles with the portions of differential capacity plots at the inset cells using dual-current formation protocol with 1M LiPF$_6$ in EC:DMC (1:1, v/v) and either 2 wt% (a and b) or 1 wt% FEC (c and d), respectively.

As shown in panels *a* and *c*, the dual-current formation protocol using C/10 and C/5 leads to the similar cycling behavior with both 2 and 1 wt% FEC. The main difference is observed at 3C, where the cells cycled at C/10 during the formation step deliver higher delithiation capacities than those, cycled at C/5. This effect is more pronounced for the cells with less additive (Figure 50c).

The voltage profiles are displayed in Figure 50 (panels *b* and *d*). Both in case of 2 or 1 wt% FEC, higher polarization is observed, when the C-rate is changed to C/5 due to the increase of the current density. The voltage drops sharply to ~0.1 V first, and only afterwards the staging intercalation starts. Furthermore, the delivered charge capacity using C/5 during the constant

current step is at least 50 mAh g^{-1} lower than that at C/10, indicating a rather sluggish intercalation. However, upon the constant voltage step when the cycling-related stresses are released, similar charge capacity to that of C/10 is obtained. The differential capacity plots at the insets of Figure 50b,d display only one peak between 0.8 and 1.0 V, attributed to the decomposition of FEC, independent of the amount of the additive.

No significant difference in the 1st cycle efficiency upon decrease of the additive content is observed, as summarized in Table 9. The table additionally includes the time saved when applying the dual-current protocol as compared to the lab standard counterpart. The capacity drop observed for the cells in Figure 50a between 60th and 70th cycles is most likely an artifact, originating from the side reactions on the lithium surface and does not depend on the applied formation step. This artifact was observed in a large number of half cells with different electrolytes after ~50 cycles. However, it always disappeared when the full cells were used. When comparing the results from Table 9 with the ones from Table 8, it can be seen that the dual-current protocol does not negatively influence the 1st cycle efficiency and rate capability, allowing at the same time reduction of the formation time by either 8 or 13 h with respect to the lab standard protocol, performed at C/20. Based on the cycling results, C/20 → C/10 protocol was selected for the full cell tests as it yielded improved rate capability and high 1st cycle coulombic efficiency.

Table 9. Summary of the efficiencies and delivered capacities at 3C with dual-current formation step and two electrolytes.

Electrolyte	Formation step rates	Time saved upon first lithiation, h	1st cycle coulombic efficiency, %	Specific delithiation capacity at 3C, mAh g^{-1}
1M LiPF$_6$ in EC:DMC + 2 wt% FEC	C/20 → C/10	8	92.3	259
	C/20 → C/5	13	92.9	251
1M LiPF$_6$ in EC:DMC + 1 wt% FEC	C/20 → C/10	8	92.5	239
	C/20 → C/5	13	92.8	214

4.3.2 Validation of the formation protocols in full graphite/LFP cells

Although the influence of the formation step on the cyclability of graphite material was tested in half cells, it does not represent the "real" case, when the lithium inventory is limited. Therefore, the formation protocols were further investigated in full graphite/LFP cells.

Section 4.3.1.1 showed that for the lab standard protocol charging at C/20 gave the best results, and, therefore, this rate was used for the full cells as well. The dual-current formation protocol, in turns, was designed to benefit from the slow current density employed upon the SEI

formation on the graphite electrode. In a two-electrode full cell (a coin cell in this case, which simulates practical conditions) only the total cell voltage can be monitored. Therefore, at first, a three-electrode T-cell was used to estimate the time necessary to bring the anode potential to 0.2 V *vs* Li/Li$^+$. The voltage profiles of the cells, including the separated contributions of the anode and cathode, obtained in the 1st cycle with 1M LiPF$_6$ in EC:DMC (1:1, v/v) + 2 wt% FEC electrolyte, are shown in Figure 51. The anode potential drops below 0.2 V *vs* Li/Li$^+$ after 3 h. Therefore, for the full cell tests this time was set as a cut-off for a switch from charge at C/20 to C/10.
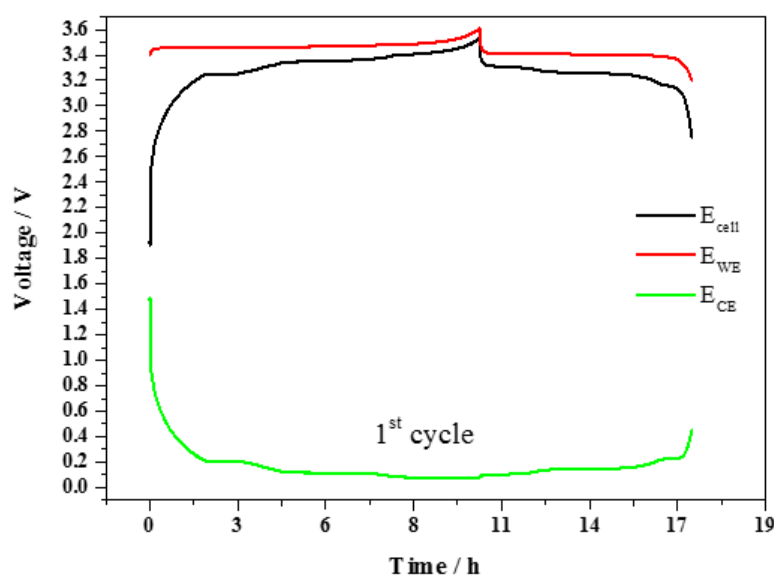
Figure 51. Three-electrode graphite/LFP cell (black), cathode (red) and anode (green) voltage profiles obtained at C/20 and 20 °C using 1M LiPF$_6$ in EC:DMC (1:1, v/v) + 2 wt% FEC electrolyte.

Additionally, the third protocol, designated as "industrial", was applied to the full cells. As reported in Table 10, the cell is initially charged up to ~3.0 V to ensure that the potential of graphite is below the threshold of Cu corrosion (~3.3 V *vs* Li/Li$^+$) [207]. After this step the current collector should not be influenced by the long wetting period of 10 h above room temperature. As reported in the available literature [207], this precharge reduces the amount of oxides on the graphite surface and induces the insertion of small portion of lithium into graphite, which is considered by the authors to be beneficial. In general, battery makers often perform the formation cycle(s) above room temperature (at 40 °C in this case) to accelerate the formation of the SEI and to enrich it with more compact inorganic species, such as Li$_2$CO$_3$, LiF and Li$_2$O than softer organic lithium alkyl carbonates [13]. After the wetting period is completed, the cell is charged in a constant current-constant voltage mode at C/10, followed by the 30-minute rest step, and discharged using the same rate.

Table 10. Industrial protocol description.

Step	Rate	Time, h	Cut-off voltage, V	Temperature, °C
Precharge	C/10	~0.5	3.0	20
Rest		10		40
Charge	C/10	10	3.6	40
Rest		0.2		40
Discharge	C/10	10	2.5	40
Rest		1		20

The electrolyte with 2 wt% FEC was used for the full cell investigation, as it yielded a slightly higher rate capability than that with 1 wt% of this additive. The electrolyte containing 2 wt% LiTFSI, which was discussed in Section 4.2, was also studied for the comparison. Both additives are beneficial for the cycling performance as they help the formation of stable and thin SEI on the anode surface. However, the reduction mechanism and the composition of the passive layer is different. The reductive decomposition of FEC can follow several mechanisms, which were discussed in Section 2.4.1.1. In case of LiTFSI no mechanism has been proposed yet; however, the results reported in Section 4.2 suggest that the salt anion is cathodically stable and probably incorporates into the SEI. Nevertheless, with both additives the resulting SEI is rich in LiF but contains more polymeric organic species with FEC than with LiTFSI.

Figure 52 displays the results of the rate test followed by the long-term cycling of the full graphite/LFP cells using two electrolytes and performing three different formation protocols. As follows from Figure 52a,b, using lab standard or dual-current protocols, the rate capability, is slightly enhanced compared to the industrial formation one. The long-term cycling stability is satisfactory with all protocols. In particular, as summarized in Table 11 the capacity retention with FEC is higher than that obtained with LiTFSI. This might indicate that the SEI, formed upon the decomposition of FEC, is more stable compared to LiTFSI. The main advantage of the electrolyte with LiTFSI additive, in line with results of Section 4.2, is the slight improvement of the 1st cycle coulombic efficiency.
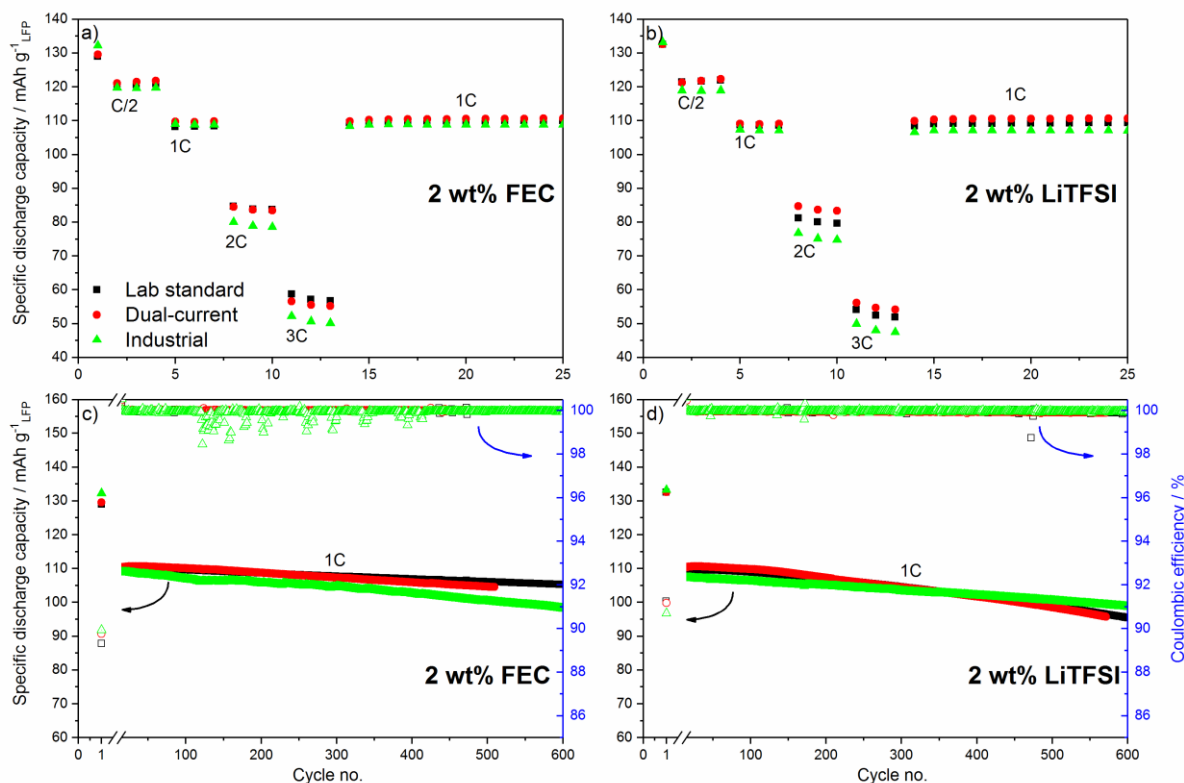
Figure 52. C-rate test (panels a and b) and long-term cycling (panels c and d) of the full graphite/LFP cells with two electrolytes using three formation protocols.

Table 11. Summary of the 1st cycle coulombic efficiency, rate capability and capacity retention with two electrolytes, using three formation steps.

Formation step	1st cycle efficiency, %		Discharge capacity at 3C, mAh g^{-1}		Capacity retention at 500th *vs* 15th cycles, %	
	2 wt% FEC	2 wt% LiTFSI	2 wt% FEC	2 wt% LiTFSI	2 wt% FEC	2 wt% LiTFSI
Lab standard	89.3	91.2	56.7	51.9	96.7	90.6
Dual-current	89.9	91.2	55.2	54.1	94.8	89.2
Industrial	89.9	90.7	50.1	47.4	92.1	93.7

The coulombic efficiency upon cycling at 1C is close to 100% for all cells, although, it should be mentioned that in some cases scattered values were obtained upon cycling (for example, as in case of the cell with FEC additive using industrial protocol in Figure 52c). This may arise from the side reactions at present unknown. Overall, the best results were obtained using FEC-additive and both dual-current and industrial formation protocols, but the former has the advantage of being easier to implement. To determine if the different protocols induce changes in the SEI composition, XPS analysis was conducted on the cycled graphite electrodes.

4.3.3 Ex-situ XPS analysis of the lithiated and delithiated graphite electrodes

XPS analysis of the SEI on the graphite, resulting from the different formation protocols, was conducted on the electrodes, extracted from full cells after complete graphite lithiation (charge) and delithiation (discharge). It should be kept in mind that the industrial protocol contained steps above room temperature. The signals were normalized to the total area of the peaks, obtained with the lab standard formation protocol, allowing direct comparison of the peak intensities. As the influence of LiTFSI as additive on the SEI formation has been already evaluated via XPS in Section 4.2.2, here the attention is focused on the electrolyte, containing 2 wt% FEC.

Figure 53 shows the C1s spectra, obtained for the lithiated and delithiated graphite electrodes. In all cases the peak with the highest intensity corresponds to C-C and C-H groups from graphite, conductive carbon and binder. The high intensity of this peak confirms the thin nature of the SEI, covering the material. The relative intensity of the C-O-C peak is mostly attributed to PEO, formed upon the decomposition of solvents. Among the lithiated electrodes (panel *g*) its contribution to the total atomic weight is lower for the lab standard protocol with respect to the other counterparts. However, after the delithiation (panel *h*) the trend is reversed. In particular, with the industrial and the dual-current protocols the C-O-C concentration shows a 10 at% decrease. In case of the lab standard protocol the minor change in the intensity of C-O-C peak indicates the retained presence of PEO in the outer SEI layer after the complete 1st cycle. Instead, in case of dual-current and industrial formation protocols, PEO is further decomposing upon discharge and forming carbonates, whose concentration in the SEI is increasing (Figure 53h). The atomic percentage of lithiated graphite species, obtained from the peak at 282.8 eV, surprisingly increases upon delithiation. Following the hypothesis that Li_xC_6 species are not the SEI components and that their signal is rather generated by the incomplete delithiation of graphite below SEI, this further suggests that the initially formed SEI is unstable and becomes thinner upon cell discharge. In line with the trend observed for PEO species, the variation of Li_xC_6 concentration is more significant for the dual-current and industrial protocols.
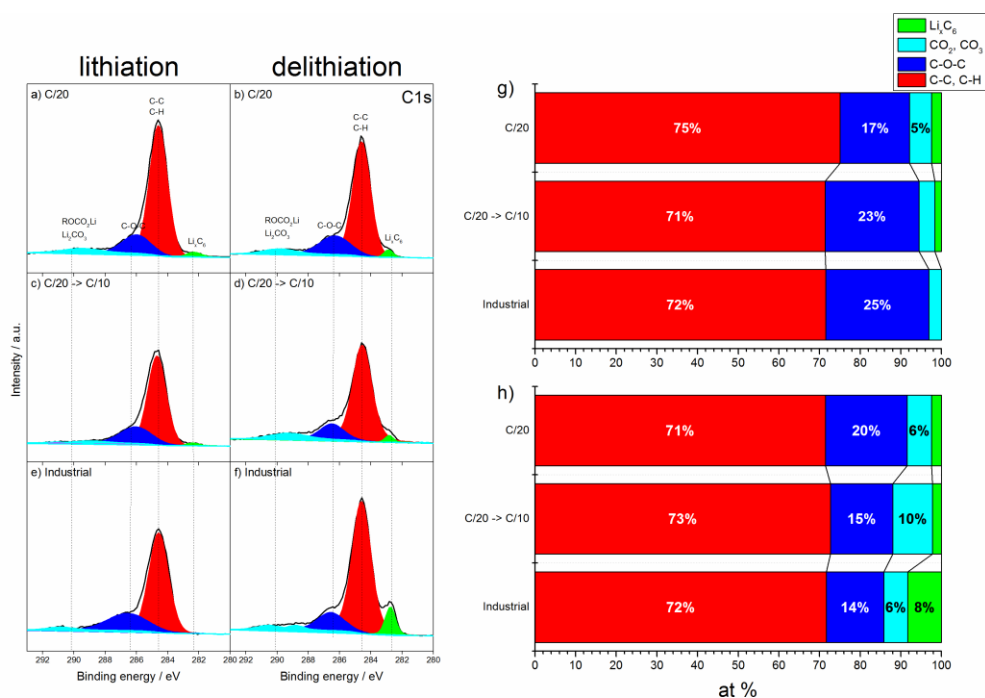
Figure 53. C1s XPS spectra of the graphite electrodes using different formation steps (a-f) and bar-charts with atomic weight percentages after g) first lithiation and h) first delithiation. The atomic concentrations below 5% are hidden for a better readability of the numbers.

The amount of formed LiF can be derived from the F1s XPS spectra in Figure 54. For lithiated electrodes using dual-current and industrial protocols, substantially higher amounts of LiF are found on the surface with respect to lab standard formation protocol. Taking into account that only 10% LiF was produced when bare LP30 was employed (Section 4.2.5), the rest of LiF is likely the decomposition product of FEC. Therefore, upon lithiation more organic species are produced using lab standard protocol, reducing the signal of LiF, whereas during dual-current and industrial protocols this salt stays rather on the surface. After the delithiation (Figure 54h), a strong decrease in LiF amount on the surface is observed for dual-current and industrial protocols, while for the lab standard one the opposite effect is seen.
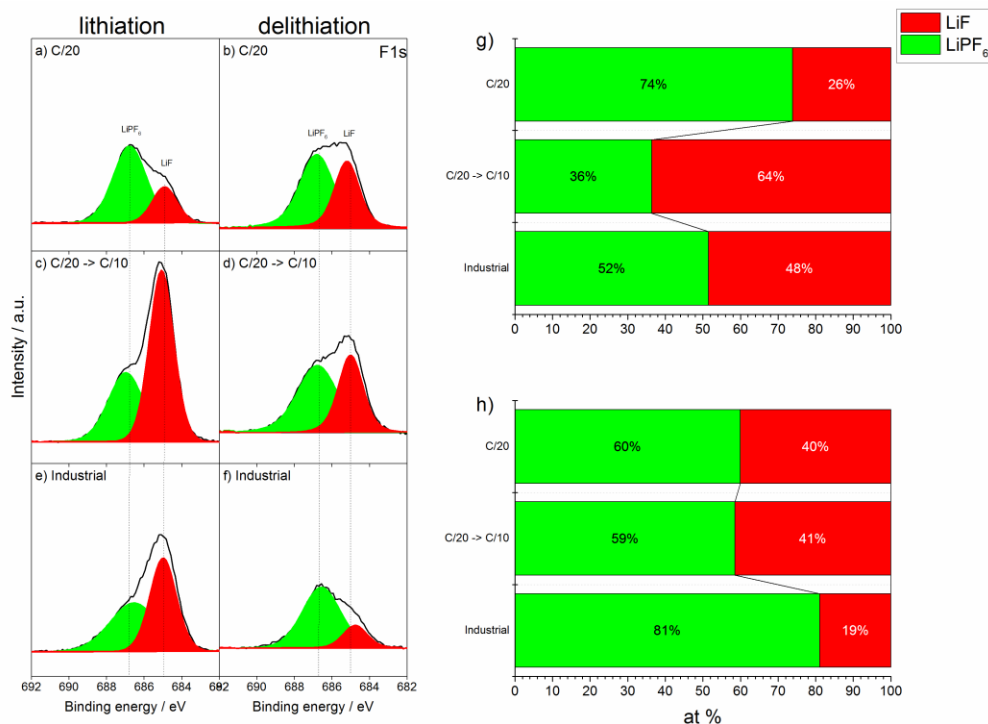
Figure 54. F1s XPS spectra of the graphite electrodes (a-f) and bar-charts with atomic compositions of SEI components after g) lithiation and h) delithiation.

The XPS results show that the SEI composition evolves upon lithiated and delithiated states. The more significant changes are observed for the dual-current and industrial protocols, for which PEO and LiF amounts decrease, whereas Li_xC_6 signal increases upon delithiation. This aspect is particularly interesting, considering that the two protocols are implemented at different temperatures (20 and 40 °C, respectively).

The SEI composition variation might be induced by graphite volume contraction upon delithiation (~10%). The generated mechanical stresses can lead to fracture and, thus, further electrolyte decomposition and re-precipitation of the insoluble products, like carbonates. However, this would imply that the additional re-precipitation of carbonates generates an increase of thickness, explaining the reduction of the detectable signal from PEO and LiF. It is, however, in contrast with the observations of more intense signal for Li_xC_6 species, which are supposed to be underneath the SEI. This aspect will be further discussed in the Section 4.3.5. Overall, the results clearly show that a single cycle is not enough to complete the SEI formation with any protocol.

4.3.4 EIS analysis of the graphite and LFP electrodes cycled in the full cells

The difference in the SEI composition may also affect the SEI resistance. Therefore, EIS measurements were conducted in the same conditions as for the XPS data collection, i.e., in

fully charged (lithiated) and discharged (delithiated) states. Additionally, the auxiliary cables were used to monitor the evolution of impedance between the reference (Li metal) and graphite electrodes to separate the cathode and anode contributions. The obtained spectra are shown in Figure 55. It should be noted that spectra of the electrodes, cycled using the lab standard and dual-current protocols, were obtained at 20 °C, whereas the ones using industrial formation step, were measured at 40 °C. This led to the shift (~0.5 Ω) towards lower resistance of the spectra acquired for industrial formation, as shown in Figure 55a,b. The higher temperature results in a higher electrolyte conductivity, and, thus, lower bulk resistance measured as the intercept of the semicircle at high frequency with Z' axis.
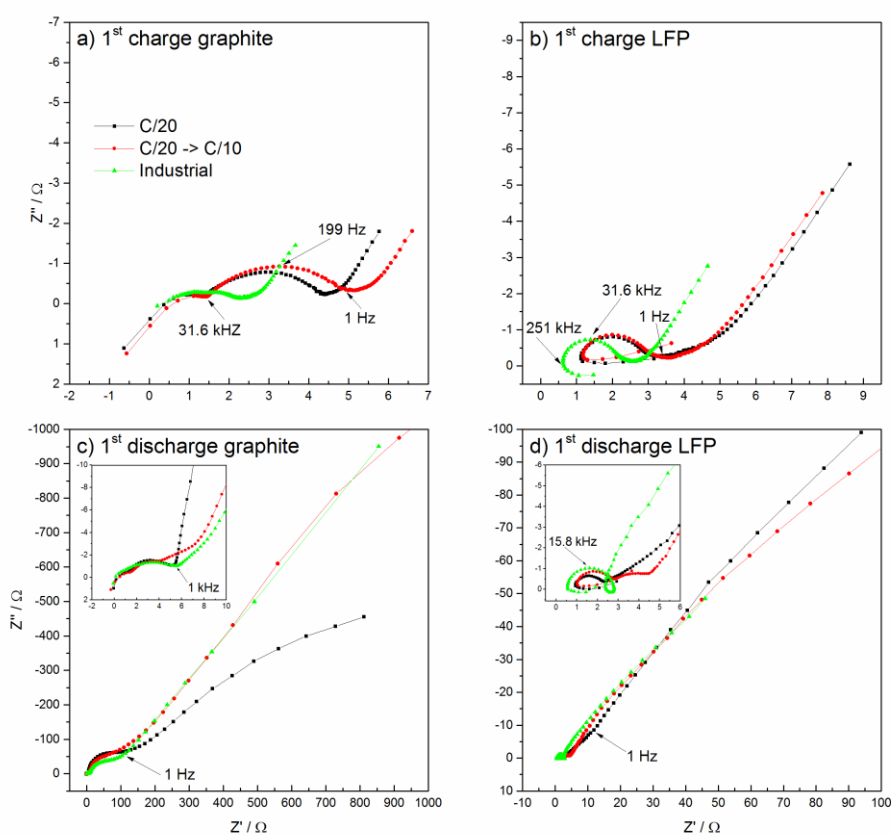
Figure 55. EIS spectra of the graphite (a and c) and LFP (b and d) electrodes measured after the 1st charge and discharge, respectively. Electrode area: 2.54 cm².

The graphite spectra in charged state consist of three semicircles, one in the high frequency region (above 31.6 kHz), attributed to the contact factors, and the other two highly overlapping in the high-to-middle frequency range (above 1 Hz), which are associated with the interfacial processes (SEI and charge transfer). Due to the higher operating temperature, the size of the latter semicircles is smaller when the industrial formation protocol is used, as compared to the lab standard and dual-current formation protocols done at 20 °C. The higher interfacial

resistance measured for the dual-current protocol with respect to the lab standard one may be related to the higher LiF and PEO contents. The length of the straight line below 1 Hz, attributed to the diffusion resistance of lithium ions on the graphite/electrolyte interface, is slightly lower using industrial formation protocol with the respect to the two counterparts. Hence, the lithium transport through the SEI is faster at 40 °C.

The spectra of the LFP electrodes in the charged state (Figure 55b) look very similar for all formation protocols. The semicircle between 251 kHz and 1 Hz is associated with the formation of the passivation layer on the cathode surface and the charge transfer due to lithium deinsertion. The straight line below 1 Hz arises from the ionic resistance in the pores of cathode material [208, 209].

After the delithiation of the anode (Figure 55c), the semicircle, attributed to the interfacial resistance can be split in two, as highlighted at the inset showing the enlarged portion of the spectra. The semicircle at higher frequencies, attributed to the SEI resistance remained almost unchanged with lab standard and dual-current formation protocols with respect to the lithiated state. Instead, the SEI resistance increased for the industrial protocol although the temperature was higher, which may reinforce the hypothesis of a more severe SEI reconstruction, as also shown via XPS. The increase in the charge transfer (semicircle between 1 kHz and 1 Hz) and Warburg resistances (the open semicircle below 1 Hz) of the graphite electrodes is due to the higher resistivity of the lithium deintercalation and migration through the double layer. Similar increase is also observed for the cathode, which is related to the resistance upon lithium intercalation into cathode, which has low conductivity [209]. Simultaneously, the diffusion-related resistance of the cathode at low frequency significantly increases, as shown by the straight line in Figure 55d. The cathode spectra, using industrial formation protocol, shows the inductive loop (inset of panel d). However, it is most likely an artifact of the three-electrode measurement set-up, as it was not observed for the cathodes, cycled using other two formation protocols.

4.3.5   *HRTEM investigation of the SEI formed using different formation protocols*

HRTEM is a useful tool to study the structural changes in graphite upon the SEI build-up. Therefore, the images of the pristine graphite electrodes were compared with those, obtained after the 1st or 104th charge/discharge cycle in the full cell configuration, using three different formation steps in FEC-containing electrolyte. Figure 56 depicts the pristine graphite material, and both basal and edge graphene planes can be distinguished, as also confirmed by the fast Fourier transform (FFT) images on the right. The interplanar distance of the graphene sheets

was determined to be ~3.67 Å. The edges of the graphene planes are slightly curved, which is attributed to the presence of surface defects.
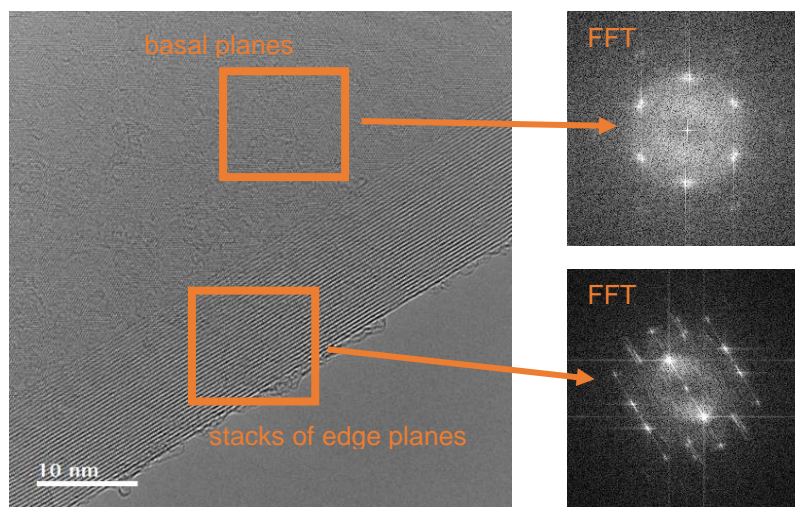
Figure 56. HRTEM and the corresponding FFT images of the pristine graphite.

The HRTEM image of the graphite after the 1st cycle using the lab standard formation step are shown in Figure 57a. The non-regular interplanar distance of the graphene sheets indicates a pronounced surface amorphization with respect to the pristine material. The SEI formed using this protocol seems to consist of two layers with different texture. These layers, however, disappear after prolonged cycling (Figure 57b). Instead, a thick amorphous layer in between the distorted graphene planes appears after 104 cycles. Although it is generally believed that the SEI layer grows at the electrode/electrolyte interface, the image in panel *b* shows that the passive layer is located in between the graphene sheets, which still can be distinguished.

In case of dual-current formation protocol (Figure 57c) the surface amorphization after the 1st cycle is even more pronounced, as no graphene planes can be distinguished. It might be also noted that the dual-current formation yields an apparently single-layered surface film, which is quite rough and inhomogeneous. After 104th cycle (Figure 57d) the SEI layer completely amorphizes and smoothens along the graphite particle. Additionally, a slight increase in the SEI thickness can be appreciated. However, the thickness increase is much less pronounced with respect to the lab standard protocol (Figure 57b).

Industrial formation protocol (Figure 57e) also leads to the surface amorphization, however, to a lesser extent compared to other protocols. Indeed, the graphene planes, though deformed, are still clearly visible on the surface even after prolonged cycling (Figure 57f). As in case of lab standard protocol, it seems that the SEI is located in between the graphene sheets. However, the graphene planes are less distorted, which might be attributed to the higher temperature applied during the industrial protocol.
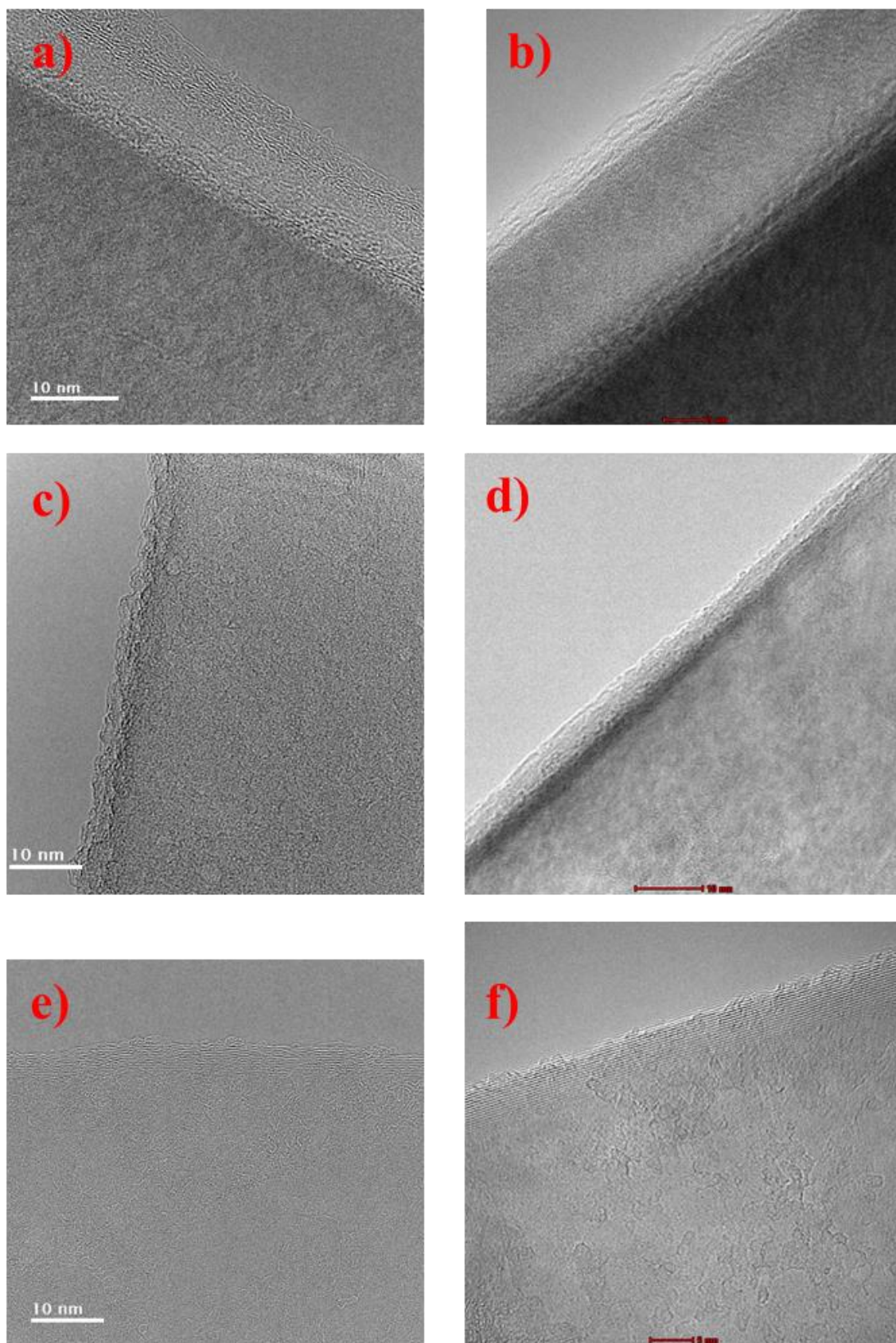
Figure 57. HRTEM images of the graphite powders extracted from the full cells after the 1st or 104th cycles, using lab standard (a and b), dual-current (c and d), and industrial (e and f) formation protocols.

As pointed above, accepted models describe SEI as a multiple layer on top of graphite particles [189]. However, the HRTEM images harvested from the samples do not reveal any clear additional surface film but rather an amorphous layer between the graphene sheets. This matches well with the early observation of Besenhard et al. [50]. The authors suggested that the electrolyte decomposition products remain between the layers and, thus, the SEI penetrates the surface of graphite. This would explain the detection of Li_xC_6 signal (see C1s XPS spectra discussion and Figure 53) also for the delithiated graphite electrodes, which was initially supposed to be underneath the SEI, erroneously suggesting a thickening of the passive layer. To fully prove the SEI interpretation with graphite electrodes the electron energy loss spectroscopy (EELS) would be useful to obtain the elemental composition of the amorphous surface layers to compare with the XPS results.

Another aspect evidenced by HRTEM is the graphite surface amorphization that was investigated by Sethuraman et al. [210]. The authors attributed this process to anisotropic character of lithium intercalation. As the high-energetic electrons are preferentially located on the edge sites, lithium bonding with carbon atoms rather occurs at these sites than in the bulk. This leads to the concentration gradient between the occupied surface sites and the bulk, inducing the lattice deformation near the edge of the graphene layers. The progressive structural disordering of the graphite surface is considered to have a negative impact on the composition and thickness of the SEI, which continuously reforms consuming Li^+ and reducing cell capacity upon cycling. Therefore, the higher level of crystallinity, observed using the industrial protocol indicates that the formed SEI is more stable, effectively protecting the graphite surface. This was also confirmed by Huang et al. [59], who showed that the higher formation temperature contributes to the formation of a more stable SEI, which impedes the side reactions at anode/electrolyte interface.

4.3.6 *Validation of the formation step protocols in the full lithium-ion pouch cells configuration*

Although labs-scale coin cells provide sufficient preliminary information about the effectiveness of each formation step, the employed set-up is not realistic. Indeed, glass fiber separators are never employed in industrial cells. Instead, the microporous polymer membranes (i.e., Celgard) are utilized due to their thinness and thermal shutdown properties [12]. However, the wettability of these separators is relatively poor compared to the glass fiber counterpart, which allows to use an excess of electrolyte to avoid cell dry-out upon extended cycling.

To validate the results obtained in coin cells in a more realistic environment, pouch cell configuration was selected allowing to test larger electrodes (16 cm²). Commercial cells are usually degassed after the formation step. As this procedure was complicated at the facilities due to the possible evaporation of toxic gases in the laboratory, a small tube was placed into the pouch cell, which could trap the gas bubbles inside the "dead volume". The pouch cells were prepared inside the dry room. The contact between the anode and cathode tabs (1 cm²) with Ni and Al current collectors, respectively, was realized by ultrasonic welding. Celgard 2325 was used as a separator. Electrolyte was added in a blister just before vacuum sealing of the cell and opened, applying external pressure, after the cell was hermetically closed. The open and closed pouch cells are shown in Figure 58.

Figure 58. a) Open and b) closed full pouch cell.

Manual pouch cell assembly is a time-consuming process. Thus, to reduce the number of variables (hence, the amount of cells to assemble), only two formation protocols (lab standard and dual-current) were validated using either FEC or LiTFSI additives in the electrolyte. Therefore, 4 cells were assembled in total. To analyze the evolution of impedance, the cells were subjected to EIS measurements immediately after the assembly, and after the 1st (formation step), 5th (at C/10), 106th, 506th and 1006th (latter three at 1C) cycles. Figure 59 shows the obtained cycling performance comparing the formation steps and electrolytes.
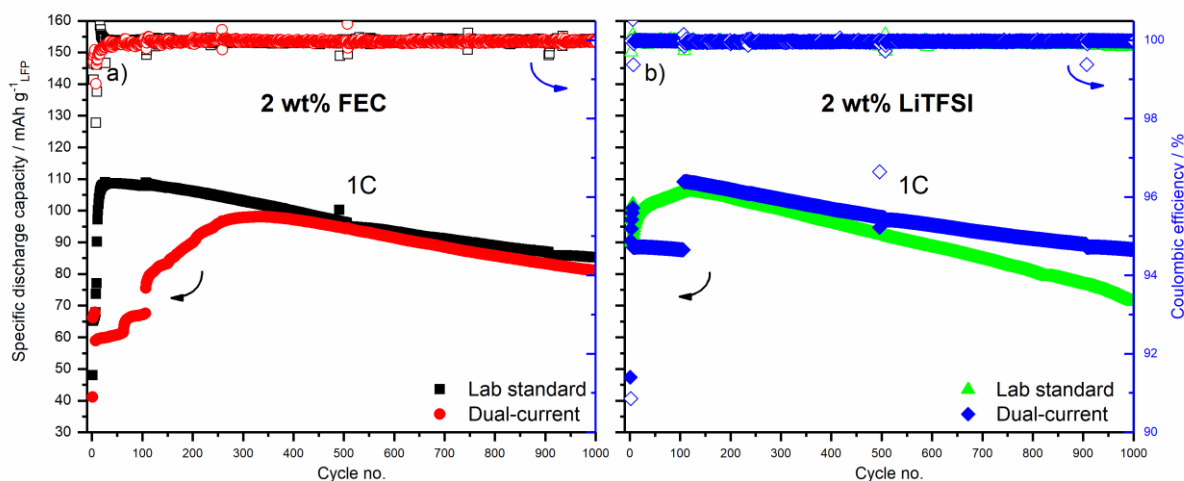
Figure 59. Long-term cycling of full graphite/LFP pouch cells with 1M LiPF$_6$ in EC:DMC (1:1, v/v) and a) 2 wt% FEC or b) 2 wt% LiTFSI. Electrode area: 16 cm².

The delivered capacity and the 1st cycle efficiency are much lower than those, obtained with coin cells. This is related to the factors, mentioned above (i.e., separator wettability, "dead volume", extended gas evolution, etc.). In case of LiTFSI-containing electrolyte, a stable capacity of ~100 mAh g^{-1} at 1C, delivered also in coin cells, is fully obtained after 100 cycles. This value is reached faster with FEC-containing electrolyte using C/20 formation step. However, when dual-current formation is employed with the same electrolyte, 300 cycles are required to reach the standard capacity at 1C. It is suggested that this behavior is related to the formation and growth of SEI, which can be negatively affected by the cell assembly and the applied formation step. Overall, at 1006th cycle the capacity retention of all cells is below 80%, except for LiTFSI-containing one with a dual-current formation. Although, the scale-up entails particular issues, which require further optimization, the cycling results suggest that the dual-current formation protocol does not deteriorate the capacity retention and allows stable cycling.

Figure 60 displays the EIS spectra, obtained at certain intervals during cycling. Each spectrum consists of two semicircles in the high-to-medium frequency range with a straight line in the low-frequency region. As also discussed in Section 4.3.4, the first semicircle is attributed to the formation of the SEI on the electrode, whereas the second semicircle is associated with the charge transfer and formation of the double layer. Although it is known that a passivation film is also formed on the cathode (cathode electrolyte interphase or CEI), the losses related to its formation are negligible. Therefore, the first semicircle might be attributed mostly to the resistance of the anode SEI. The straight line in the low-frequency range is related to the diffusion of Li ions through the SEI. At OCV, as no diffusion-related process is expected to occur at the electrode (no faradaic reactions), the feature at low frequency has an angle of about 90°, approaching the blocking electrode behavior. The most significant difference in spectra is

observed between the 1st and 5th cycles. Upon cycling the spectra shrink, and no significant change is seen between them after 506th and 1006th cycles. The spectra of the cell that performed the lab standard formation step with LiTFSI-containing electrolyte grow in a marked manner upon cycling, which might be related to the increase of the SEI resistance upon its continuous growth.
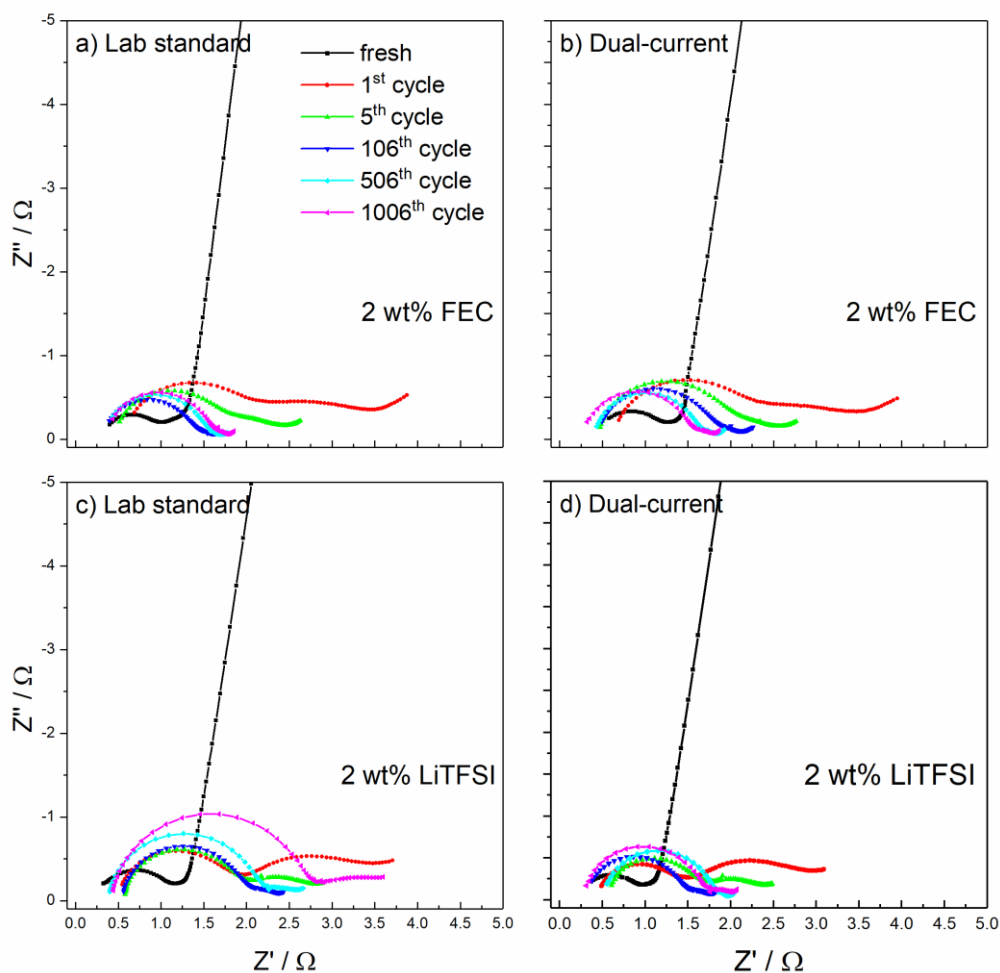
Figure 60. EIS spectra of the full pouch cells, using lab standard (a and c) or dual-current (b and d) formation steps with two electrolytes upon cycling (see the legend). Electrode area: 16 cm².

The equivalent circuit, used for the fitting of the experimental data is shown in Figure 61c. The model consists of a resistor and two R|Q elements, connected in series. The determination of each circuit element has been already discussed in Section 4.2.3, and will be omitted here. The evolution of R_{SEI} and R_{ct} as a function of cycle number is displayed in Figure 61 (panels *a* and *b*, respectively). The resistance of the SEI is slightly decreasing between the 1st and 5th cycles. Instead, the charge transfer resistance undergoes substantial decrease in this cycle range. This indicates that the 1st cycle with both formation steps was not enough to form a stable SEI on the anode surface, which is also in line with the coin cells results. A further decrease in charge transfer resistance between the 5th and 100th cycles is related to the completion of SEI and fast

transport of Li ions through it. Upon prolonged cycling R_{SEI} is only slight growing, except for the cell with LiTFSI additive, formed using lab standard protocol. Similar trend is also observed for R_{ct}. These results show that continuous, although, relatively small growth of the SEI rather than the charge transfer resistance influences the capacity fading upon cycling.
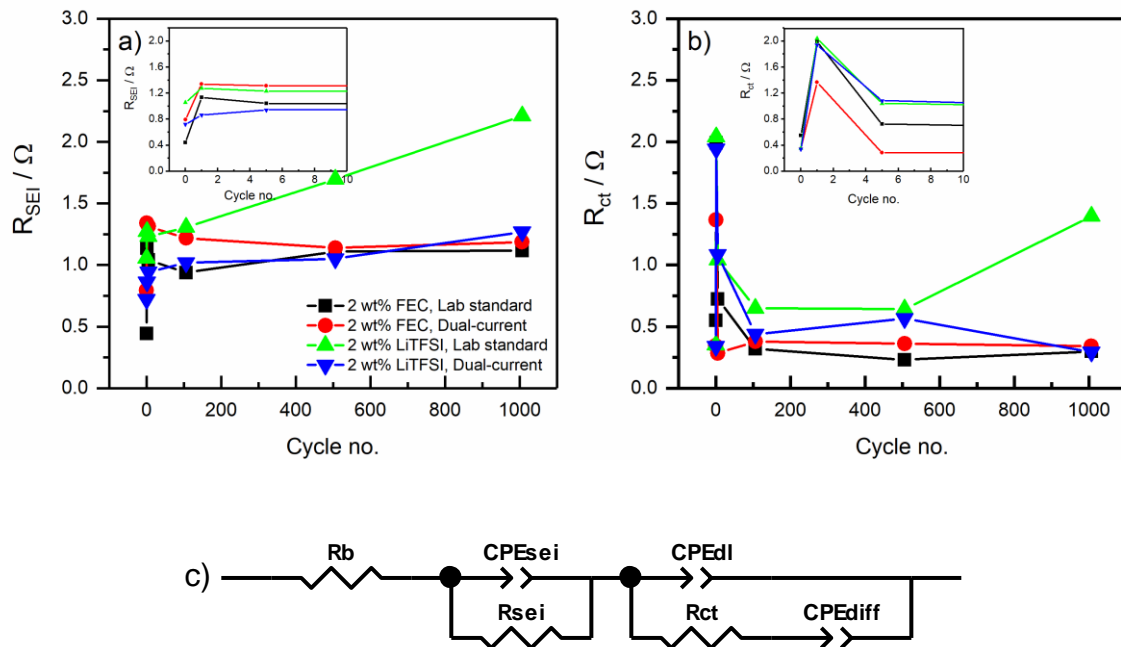
Figure 61. a) R_{SEI} and b) R_{ct} as a function of cycle number of the full pouch cells with different electrolytes, using two formation steps; c) equivalent circuit used for the modelling. Electrode area: 16 cm².

In case of FEC-containing electrolyte, the influence of the formation step on the obtained R_{SEI} and R_{ct} values is relatively small. However, with LiTFSI additive, the lab standard formation step seems to be disadvantageous and leads to the continuous increase in the SEI resistance. As mentioned above, the reason for such behavior is not fully understood and would require testing of additional cells.

4.3.7 Conclusions

The influence of the formation protocols on graphite SEI features and cell cycling stability was evaluated in the half and full cell configurations. It was shown that the use of dual-current protocol, which permits considerable time reduction necessary for the cell formation, yields slightly higher rate capability and similar capacity retention in the full cells with respect to the industrial protocol. However, for both dual-current and industrial protocols significant variation of the graphite SEI composition was observed between fully lithiated and delithiated states. This suggests a similar nature of the passivation films using both protocols, although obtained at different temperatures, and evidences that the formation is not complete after a single cycle. The EIS measurements on graphite electrodes after in the fully charged and discharged states

revealed the most pronounced changes for the industrial protocol, which are attributed to the higher operating temperature and stronger SEI reconstruction. The HRTEM images showed that the SEI penetrated the outer graphene layers, reducing the surface crystallinity. Interestingly, the graphite electrode subjected to the industrial protocol showed a reduced degree of amorphization after 104 cycles and, thus, it can be concluded that the as formed SEI is more stable with respect to other protocols.

At first instance the results show that a consistent reduction of time can be achieved using the dual-current protocol without sensibly affecting the electrochemical performance. The attempt to scale up the cells and cycling them in more realistic conditions evidenced when the dual-current protocol is used, the interfacial resistance is generally quite high, related to the kinetic limitations upon current density change. As the preliminary results in the coin cells showed similar behavior for dual-current and industrial protocols in terms of the SEI composition, further studies on pouch cells would be necessary to conclude the study.

4.4 Evaluation of carbon-coated graphite as negative electrode material for Li-ion batteries

As discussed in the previous subchapters, the use of electrolyte additives or drafting a suitable formation step protocol can lead to substantial differences in the composition of the formed SEI, resulting in the enhanced capacity retention upon extended cycling. However, such limitations of the graphite material itself, as the unfavorable orientation of the graphene sheets with respect to the flowing current [211], resulting in the limited Li$^+$ diffusion especially at lower temperatures, where the plating of Li metal is possible, should also be addressed. One of the most common methods to increase the rate capability of graphite is to introduce the carbon coating on its surface. Thin coating layer of disordered carbon can allow more random intercalation of lithium ions, thus, enhancing the performance of graphite at higher rates.

Therefore, the following subchapter, based on publication [160], presents an evaluation study of the use of low-cost and environmentally-friendly materials as carbon-coating precursors for the modification of the surface of commercial graphite anode for Li-ion battery. The coating procedure and final carbon content were tuned to study the influence of the precursors on the electrochemical performance of graphite. Thermogravimetric analysis and Brunauer–Emmett–Teller surface area analysis were used to characterize the carbon coating content and the surface area, respectively, whereas X-ray diffraction and Raman spectroscopy allowed tracking of the graphite's structural changes and surface amorphization. The Raman measurements were performed by D. Vieira Carvalho and analyzed by Dr. G. A. Giffin.

4.4.1 Physico-chemical characterization of the materials

The choice of carbon precursors was based on the goal of limiting the environmental impact associated with the coating process. Therefore, precursors requiring processing in organic solvents or releasing toxic compounds during the thermal treatment (e.g., poly(vinyl chloride)) were not considered [68]. Glucose, sucrose, and citric acid (CA) have been extensively studied as carbon sources for positive and negative electrode coatings [152, 212-214]. Polymer-type precursors, such as poly(acrylic acid) (PAA) and poly(vinyl alcohol) (PVA) were also investigated, as they possibly form a more homogeneous network around the graphite particles, thus leading to a better dispersion of carbon on the surface [68, 215, 216]. For the selection of the most suitable coating method, sucrose was used as a carbon source and the graphite:sucrose weight ratio was set to 1:1.

Figure 62 shows the TGA traces of the carbon-coated graphite obtained using three methods, which are described in Section 3.2 and summarized in Table 12. Pristine graphite is stable up

to 550 °C; therefore, the weight loss at lower temperatures is mainly attributed to the carbon coating. TGA results of the coated graphite using sucrose via three synthesis routes reveal that the coating accounted for about 20 wt% of the total mass, independent of the mixing method.
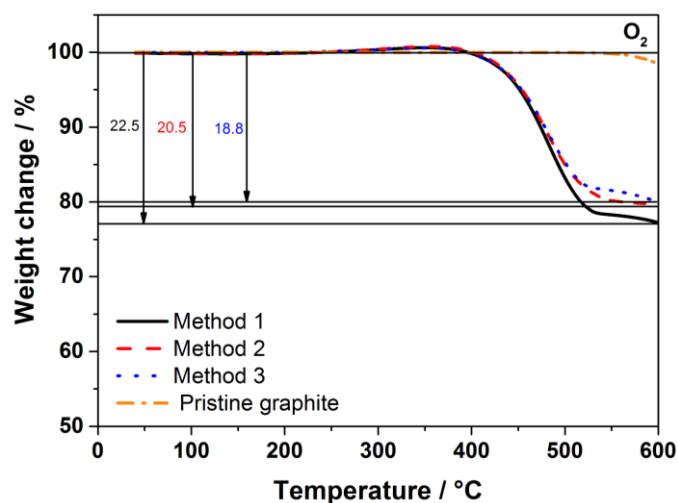
Figure 62. TGA curves of pristine and carbon-coated graphite materials in oxygen atmosphere. Sucrose was used as the carbon precursor for all synthesis routes.

Table 12. Summary of the mixing methods.

Method	Solvent	Mixing device	Duration
1	Ultra-pure H_2O	Magnetic plate	8 h
2	–	Agate mortar	10 min
3	Ultra-pure H_2O	Magnetic plate	1 h
		Ball mill	2×45 min at 400 rpm, 10 min rest

Figure 63 shows the scanning electron microscopy (SEM) images of the pristine and coated graphite materials. In all coated samples, but especially in those obtained via methods 2 and 3, the graphite particles are agglomerated. Method 1 was selected for further investigations since "wet" coating methods yield more homogeneous coating layers with respect to "dry" methods [212], and the introduction of the ball milling step (Method 3) did not lead to any clear advantage. SEM images of the carbon-coated samples show that all synthesis procedures resulted in the modification of the graphite surface, which appeared rougher than that of pristine graphite. This indicates the presence of a coating layer, which is, however, difficult to visualize by SEM.
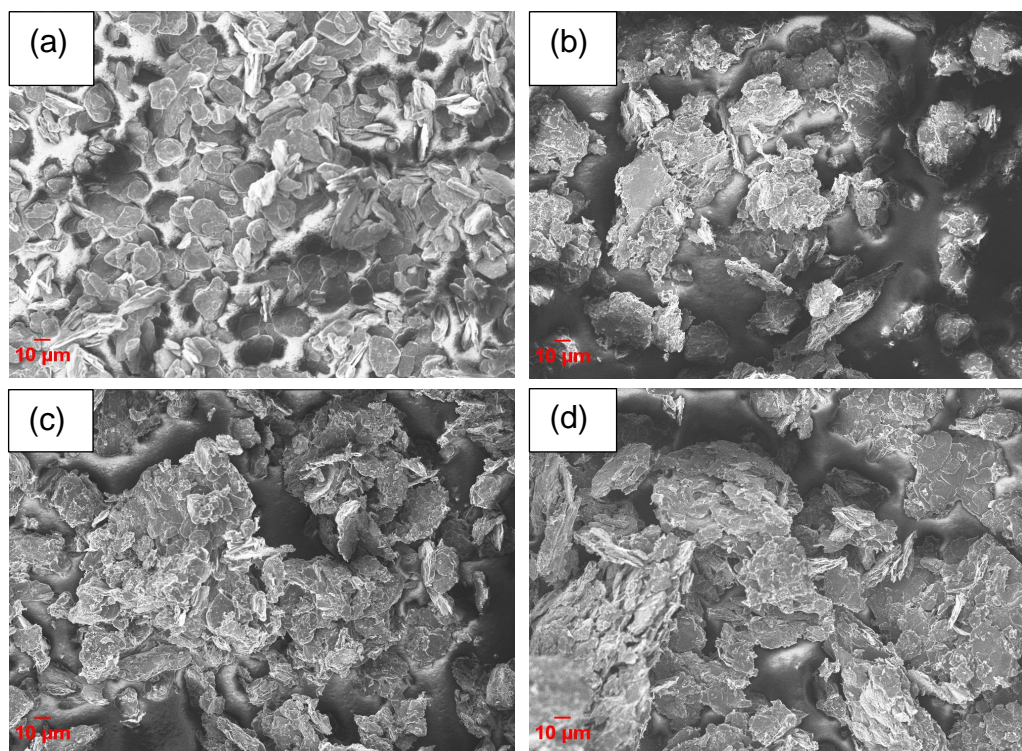
Figure 63. Micrographs of (a) pristine and coated graphite materials obtained using (b) Method 1, (c) Method 2, and (d) Method 3. Sucrose was used as the carbon precursor.

Method 1 was then extended to glucose and PAA as carbon sources, while maintaining the 1:1 graphite:precursor weight ratio. The carbon yield obtained with glucose was similar to that of sucrose (~20 wt%), whereas the use of PAA as a precursor yielded a lower amount of carbon (about 13 wt%), shown in Figure A4 in APPENDIX 2. Since a high content of amorphous carbon can exacerbate the irreversible reactions taking place at the anode/electrolyte interface [67, 68], 5 wt% of residual carbon was targeted for the coatings using all precursors. The characteristics of the coated samples are reported in Table 13. It is interesting to note that, although the amount of carbon coating is almost the same when employing water solutions of glucose and citric acid, the Brunauer-Emmett-Teller (BET) surface area of the coated samples increased with respect to that of pristine graphite. In the case of sucrose, the surface area of the final product is three times higher. An inverse effect is obtained with the polymeric precursors, leading to comparable or smaller surface areas of the coated samples with respect to pristine graphite.

Table 13. Characteristic of pristine and coated samples and electrodes: graphite:precursor weight ratios, carbon coating fraction, surface area, D/G band ratio, first cycle efficiency and delivered discharge capacity at 3C.

Sample	Graphite: precursor weight ratio	Carbon coating from TGA1, wt%	Surface area from BET^2, m^2 g^{-1}	Ratio D/G bands	1st cycle efficiency, %	Delithiation (discharge) capacity @ 3C, mAh g^{-1}
Graphite	–	–	6.9	1.05	91.2	211
Gr/Sucrose	4:1	5.3	26.1	2.04	80.8	112
Gr/Glucose	4:1	4.7	18.2	1.11	83.0	180
Gr/CA	2:1	5.0	16.9	1.12	83.4	228
Gr/PAA	3:1	4.2	8.1	1.12	82.3	171
Gr/PVA	2.5:1	4.8	4.0	1.05	87.2	116

[1] Thermogravimetric analysis (TGA) error: ±0.1 %, [2] Brunauer–Emmett–Teller (BET) error: ±0.15 %

SEM images in Figure 64 reveal that the 5 wt% carbon-coated samples appear to be less agglomerated than those in Figure 63. The coated graphite particles have a similar morphology except for the sample coated using PAA, which displays the additional formation of needle-like carbon particles (panel *d*).
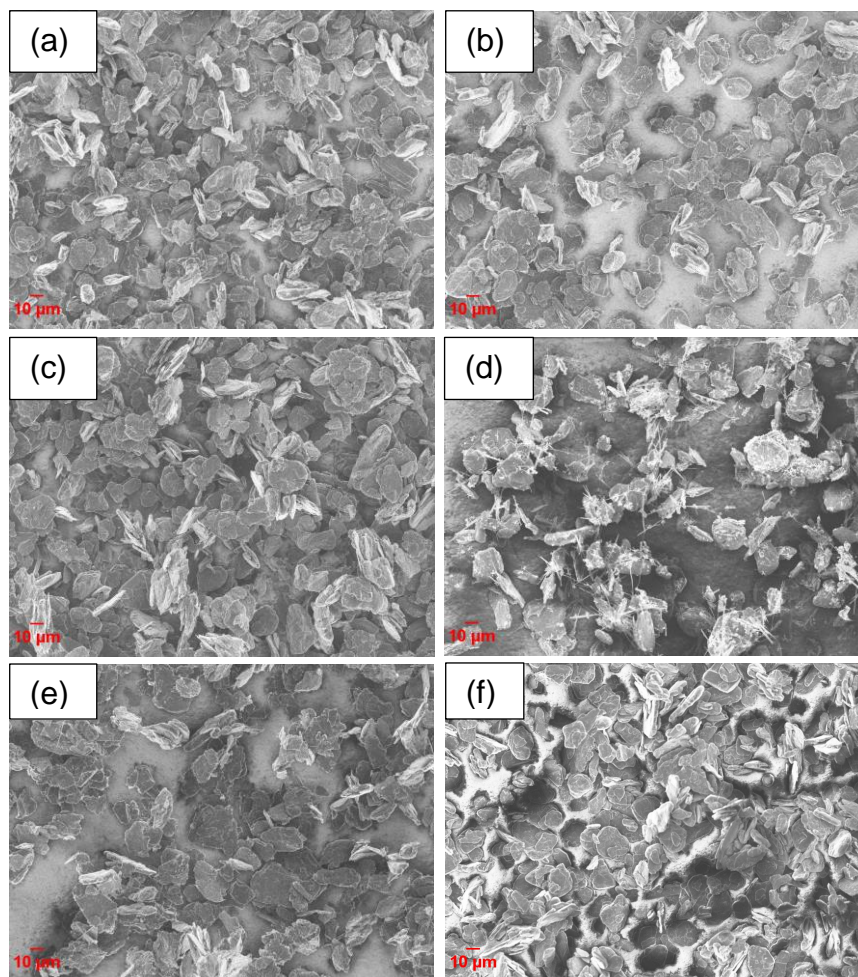
Figure 64. Scanning electron microscopy (SEM) images of carbon-coated materials: (a) Gr/Sucrose; (b) Gr/Glucose; (c) Gr/CA; (d) Gr/PAA; (e) Gr/PVA; pristine graphite (f) is also shown for comparison.

The change of the graphite crystallinity due to the formation of the amorphous carbon layer on its surface was evaluated using Raman spectroscopy. The Raman spectra of the pristine and carbon-coated graphite materials are shown in Figure 65a. The spectrum of pristine graphite exhibits an intense peak at 1572 cm^{-1}, marked with G, which is associated with sp^2 carbon bonds stretching in the basal plane of graphite. The smaller peak at 1325 cm^{-1}, marked with D, is attributed to the breathing mode of sp^3 atoms at the edge sites of graphite [217, 218]. The small shoulder at 1603 cm^{-1}, marked as D´, is also indicative of defects in the crystalline structure of graphite [219]. The D/G area ratio obtained from Raman spectroscopy is commonly used as an indicator of the extent of surface disorder in carbonaceous materials [66]. The coated samples, except that derived from PVA, have higher D/G ratios than graphite, thus confirming the surface modification due to the carbon coating. An increase in the surface disorder is supported by the broadening of D and D′ bands upon carbon coating, as indicated by Raman spectroscopy. The coated samples also have additional shoulders on both sides of the D band, which can be associated with coating-induced defects and/or the presence of heteroatoms on the graphite surface. The degree of surface "amorphization", expressed by the D/G ratio, reaches a maximum with sucrose as the carbon precursor. Gr/Sucrose and Gr/PVA samples have rather different surface areas, highlighting the different impact of the carbon precursors on the final coated samples.

Figure 65b reports the X-ray diffraction (XRD) patterns of pristine and carbon-coated graphite samples. The carbon coating does not change the graphite structure. However, a shift towards higher angles is observed for the materials prepared using citric acid and PAA, as shown in the inset of Figure 65b.
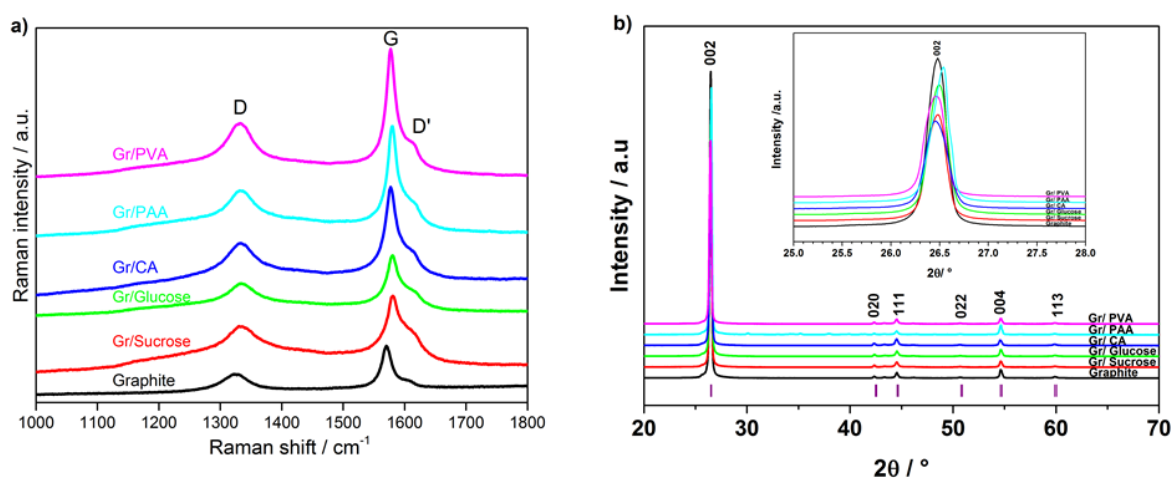
Figure 65. (a) Raman spectra and (b) X-ray diffraction (XRD) patterns of pristine and coated graphite samples.

The XRD patterns show that the carbon coating does not significantly change the graphite structure. However, the intensity decrease of the (002) diffraction peak and its broadening may indicate the reduced crystallinity of the coated materials with respect to the pristine graphite. Furthermore, the pattern of the sample using PAA contains additional peaks, which confirms the presence of crystalline impurities, i.e., needle-like particles, also observed in the SEM images, most likely arising from incomplete precursor decomposition.

4.4.2 Galvanostatic cycling in half cells

In terms of electrochemical performance, the effect of the carbon coating (~5 wt%) from the various precursors on the discharge rate of graphite in half cells is reported in Figure 66. The galvanostatic charge rate was kept constant (C/2) with the addition of the constant voltage step at the end of the charge to accomplish the full lithiation of the anode. In Figure 66a the results of the C-rate test are reported, while Figure 66b shows the subsequent cycling at C/2. Figure 66c,d reports, respectively, the first cycle voltage profile and a portion of the relative differential capacity plot.
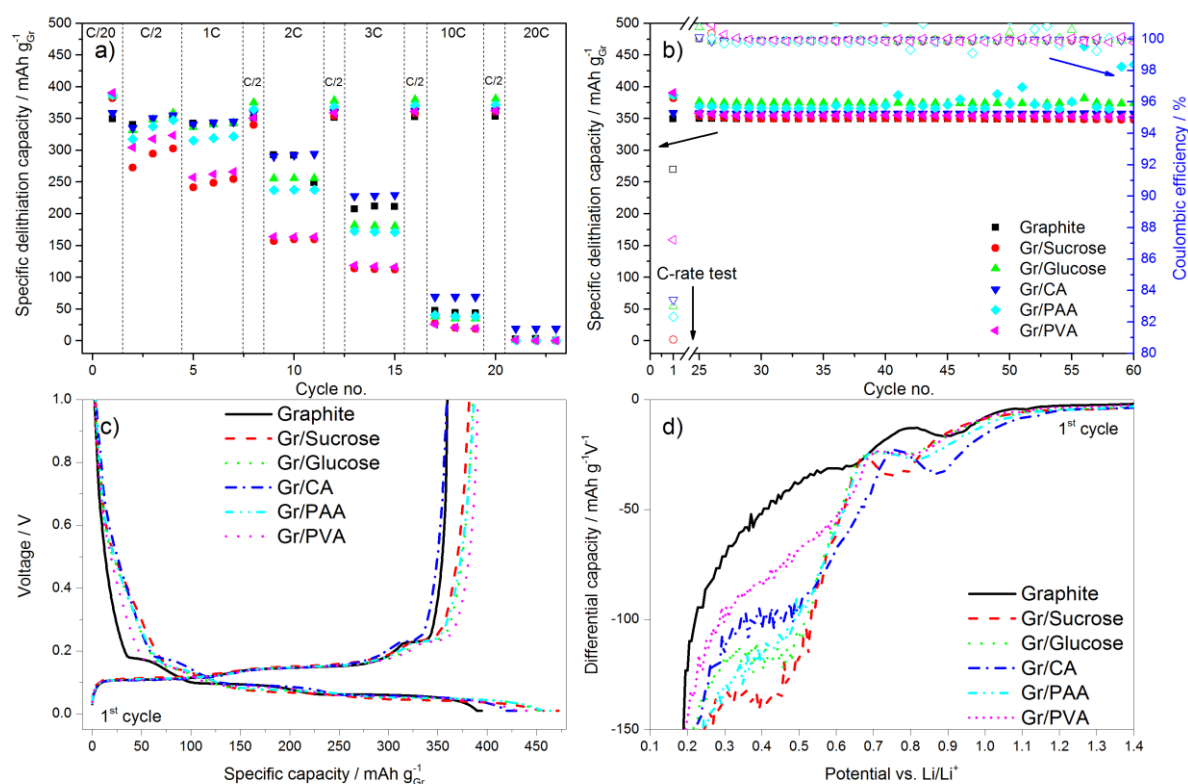
Figure 66. Electrochemical performance of pristine graphite and the carbon-coated graphite electrodes. (a) C-rate test; (b) constant cycling at C/2; (c) first cycle voltage profile; and (d) enlarged portion of differential capacity plot of the first cycle.

During the first delithiation (discharge) the carbon-coated graphite electrodes deliver a higher capacity than the pristine material. However, the values of the 1st cycle coulombic efficiency

obtained for the former electrodes are lower than that of pristine graphite, especially for the samples with the higher surface area (i.e., Gr/Sucrose, Gr/Glucose and Gr/CA). This is due to the extended SEI formation occurring in the voltage region between 1.0 and 0.2 V. Below 1.0 V the decomposition of fluoroethylene carbonate (FEC) takes place [202], the extent of which is larger for the carbon-coated materials as indicated by the relative peaks in Figure 66d being more intense. The reduction peak just below 0.7 V for the uncoated graphite is related to the decomposition of the electrolyte solvents (mainly EC), which is not completely prevented by the addition of FEC [220]. For the carbon-coated graphite electrodes, the electrolyte reduction peak is shifted to a lower voltage (~0.5 V) and its intensity is higher for the samples that have higher surface area than pristine graphite such as Gr/Glucose, Gr/Sucrose, and Gr/PAA.

The results of the cycling test show that the presence of a high surface area amorphous carbon layer intensifies the electrolyte decomposition reactions during the SEI formation, leading to lower values of the 1st cycle coulombic efficiency. Indeed, for the sample coated with PVA, which has only half the surface area of pristine graphite, the coulombic efficiency also approaches that of the uncoated material. It should also be noted that the calculations of the current densities were only based on the graphite loading, although the carbon coating is also electrochemically active and contributes to the total delivered capacity values. This results in the slight capacity increase of 30 mAh g^{-1} upon first lithiation (charge) and 10 mAh g^{-1} upon the following cycling steps as compared to the pristine graphite. Upon increasing the cycling rates, only the sample coated with citric acid displays a slightly higher discharge capacity than pristine graphite. Surprisingly, the lowest capacity values are obtained from the graphite coated using sucrose and PVA, which have the highest and the lowest surface area, respectively. However, when the cycle rate is brought back to C/2, the Gr/PAA and Gr/Glucose electrodes deliver slightly higher capacities than pristine graphite, indicating that the carbon coating participates in the Li$^+$ storage process [25]. This suggests that the amount of Li$^+$ stored in the coating varies with the precursor and the final carbon nature, thickness, and homogeneity of the layer [9,15].

In terms of rate capability improvement, citric acid seemed to be the most appropriate carbon precursor. In an attempt to further improve the performance, the amount of carbon coating was reduced from 5 to 2 wt%. This corresponded to the surface area reduction of 50% and, in fact, the 1st cycle coulombic efficiency increased (from 83.4% to 88.6%), as shown in Figure 67a. This can be univocally attributed to the lower surface area available for the SEI formation as confirmed by the voltage profile and differential capacity plots in Figure 67b. However, this approach lead to a decrease of the rate capability, as the discharge capacity at 3C for the sample

with 2 wt% carbon-coating was 30% lower than that obtained using the 5 wt% carbon-coating. The higher capacity upon constant cycling at C/2 with 2 wt% carbon-coating was additionally contributed by the moderate variation of active material loading in the electrodes.
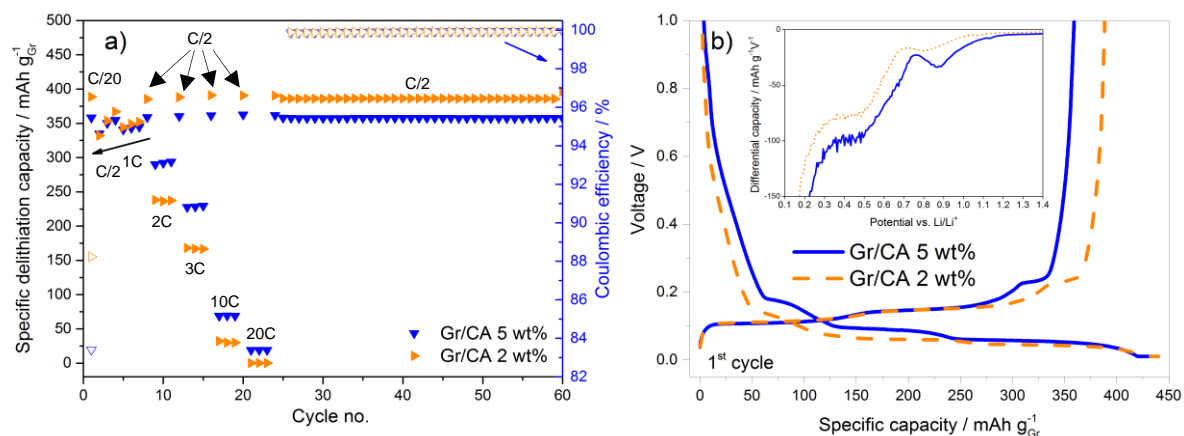
Figure 67. Electrochemical performance of coated graphite electrodes with 5 wt% and 2 wt% carbon-coating made using citric acid as a precursor. (a) C-rate test and constant cycling at C/2 (the arrows point at the corresponding y axes, closed symbols represent capacity, open symbols – coulombic efficiency); (b) first cycle voltage profile (inset: differential capacity plot for the first cycle).

Upon decreasing the carbon coating amount from 5 to 2 wt% the increase of the 1st cycle coulombic efficiency was obtained, but at the expense of the decreased rate capability. Therefore, the amount of carbon in the coating needs to be optimized in order to achieve the best trade-off between these two parameters.

Carbon coating was reported to allow Li^+ intercalation/deintercalation into graphite even in non-SEI forming electrolytes (i.e., without EC) [221]. Indeed, the possibility of using electrolytes with a high amount of PC in combination with DMC would be beneficial for the low temperature performance as PC has a lower melting point than EC. However, the use of PC is commonly prevented by the occurrence of graphite exfoliation upon solvent co-intercalation, as shown in the cyclic voltammetry (CV) in Figure 68a, where 1M $LiPF_6$ in PC:DMC (1/1, w/w) was used as the electrolyte. Figure 68b shows that the presence of 5 wt% of carbon coating was not sufficient to protect graphite. When the test is repeated using a ternary solvents mixture containing 16.67 wt% of PC (EC:DMC:PC (1/3/1, w/w/w)), one peak in the cathodic sweep is observed at 0.6 V for the pristine graphite, as shown in Figure 68c. This peak indicates the formation of the protective SEI [220], which enables reversible cycling of the uncoated material. However, in the case of 5 wt% carbon-coating, no peak is seen until 0.2 V *vs* Li/Li^+. This results in the continuous Li^+ consumption, as shown by the constant decrease of the peak intensity in Figure 68d.
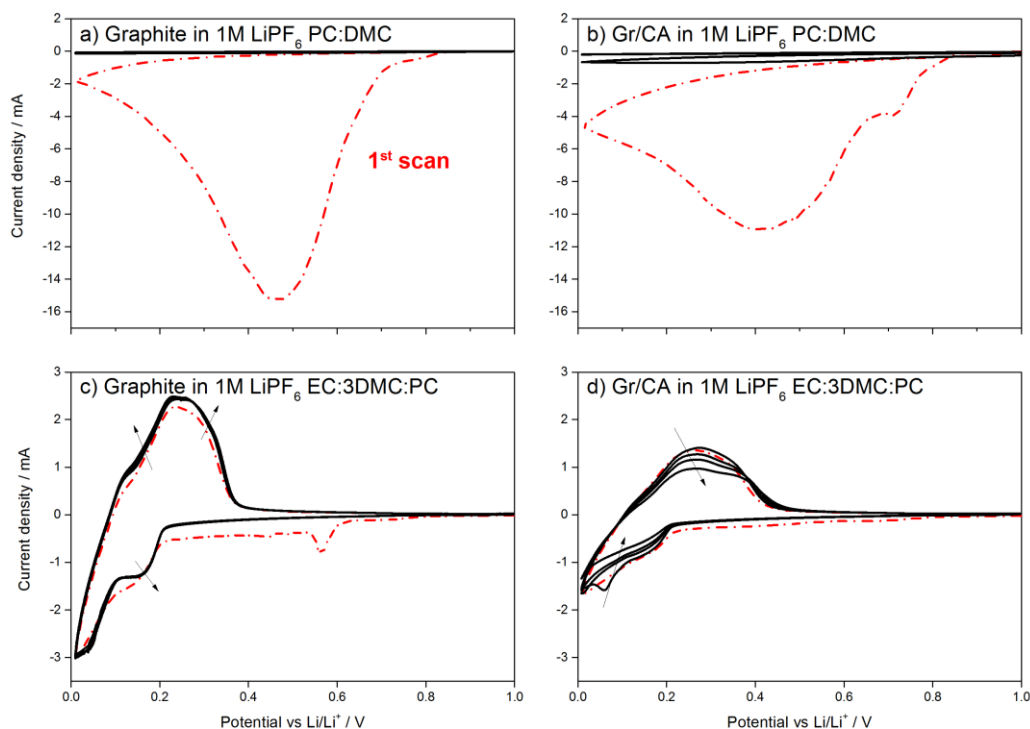
Figure 68. Cyclic voltammetry (CV) of pristine and carbon-coated (5 wt% of carbon from citric acid) graphite samples in 1M LiPF6 PC:DMC electrolyte (panels a and b) and in EC:3DMC:PC 1M LiPF6 electrolyte (panels c and d). The arrows indicate the cycle increment. PC: propylene carbonate, DMC: dimethyl carbonate, EC: ethylene carbonate. Electrode area: 1.13 cm². Scan rate: 0.1 mV s^{-1}.

As shown in the CV test, 5 wt% of carbon coating on graphite is not sufficient to protect it from exfoliation in PC-rich electrolyte, which is in line with other reports, highlighting that more than 10 wt% of carbon coating is necessary [70, 211, 221]. When the ternary electrolyte with EC is used, however, the carbon coating prevents the formation of the SEI on the graphite electrode, which leads to the continuous capacity fading upon cycling.

4.4.3   Conclusions

Carbon coating of graphite, derived from non-toxic and abundant materials using aqueous processing, was investigated in this chapter with a particular focus on the impact of the carbon source on the electrochemical properties. It was shown that the use of monomer-type precursors resulted in higher surface areas as compared to the polymer-type ones. The Raman spectroscopy suggested the surface amorphization to occur in all carbon-coated materials except the one made using PVA. At the same time, the graphite structure remained unchanged for all coated materials, as confirmed by XRD. The decreased first cycle efficiency, with respect to pristine graphite, was ascribed to the higher surface area available for the electrolyte decomposition of the carbon-coated materials. In contrast, the use of citric acid as a carbon precursor resulted in the improved rate capability compared to pristine graphite. In an attempt to reduce the

irreversible reactions at the anode/electrolyte interface and increase first cycle efficiency, a lower amount of carbon coating (from 5 to 2 wt%) was investigated. A higher coulombic efficiency was obtained, albeit at the expense of the rate capability. Although previous reports have shown that the carbon coating allows the use of graphite in combination with PC, the herein investigated amount of carbon coating (5 wt%) was not sufficient to protect the graphite from exfoliation.

5. CONCLUSIONS AND OUTLOOK

The results presented in this thesis demonstrate that the electrolyte formulation, formation protocol or surface modification of the anode material can lead to significant improvements in the performance of lithium batteries, comprising state-of-the-art materials. Furthermore, the proper selection of electrolyte additives or a design of a formation protocol can significantly improve the lifespan of the battery. Although the development of new materials and cell chemistries is an important part of the battery research, the optimization of the state-of-the-art systems is also of high significance. While the new materials require months or even years to be upscaled, the improvements of the commercially available systems can be implemented faster and with the lower costs.

The addition of a ceramic filler to the solid polymer electrolyte, comprising PEO polymer, Li conducting salt and ionic liquid lead to a higher ionic conductivity and formation of stable Li/SPE interface. As the price of the ceramic filler is lower than that of the ionic liquid, the study showed that the lithium transfer could be enhanced without undesirable cost rise. Furthermore, this quaternary solid polymer electrolyte possessed high mechanical integrity, which generally was challenging with high ionic liquid content. As the next step this quaternary SPE could be implemented with a high voltage cathode (i.e., NMC) and lithium metal. Although it is known that PEO is not stable at high voltages, the coating of the active cathode material with a ceramic material (Al_2O_3, ZrO_2, etc.) or vanadium oxide may enable stable cycling of Li-metal-polymer batteries.

The optimization of the state-of-the-art liquid electrolyte via the use of additives is another cost-efficient strategy. Among the three lithium imide salts, investigated in this work, LiTFSI had the most beneficial influence on both 1st cycle efficiency and cycling performance in full cell configuration. It is also suggested that LiTFSI mostly remains cathodically stable and rather incorporates into the SEI as a sacrificial salt, promoting formation of a stable SEI. However, the thermal stability of the SEI formed in presence of LiTFSI is relatively poor. Therefore, the combination of several additives (i.e., VC and LiTFSI) should be considered to obtain the electrolyte with the optimal properties.

Formation step protocol itself is a cost- and time-consuming process, which requires continuous optimization. Three formation protocols were studies in the thesis. The combination of electrochemical, microscopic and spectroscopic techniques was used to evaluate the influence of such parameters as current density and temperature on the formation of the SEI and capacity retention upon cycling in full cells. The dual-current formation protocol seems to be promising

in terms of time reduction compared to the lab standard counterpart and in terms of implementation compared to the industrial one. However, additional investigations in the pouch cells are required to validate the results of the coin cells. The new insight on the SEI formation, which was shown to form in between the graphene planes rather than on the surface of the anode needs further verification through the chemical analysis of the surface layer and comparison to the electrodes, obtained from the cycling in pouch cells.

Finally, the influence of the carbon-coating of graphite surface on the enhanced rate capability was evaluated, focusing on cheap and environmentally friendly carbon precursors. Indeed, the rate capability can be improved, but at the expense of lower first cycle coulombic efficiency due to higher surface area, available for electrolyte decomposition. Furthermore, the amount of carbon coating (5 wt%) was not sufficient enough to protect the graphite from exfoliation in PC-based electrolyte. Therefore, the carbon coating brings the challenge of finding a balance between the rate capability and irreversible capacity loss. As the limited rate capability of graphite is determined by its structure, one way to improve it is to engineer the particles to shorten the diffusion paths for lithium ions. Another possibility is to dope graphite with metals or attach functional groups to the surface, thus increasing its ionic conductivity.

Despite all challenges related to the research and development in the field of energy storage, I believe in the "greener" future, driven by emission-free vehicles, powered by lithium batteries. Based on the activities, initiated by the governments of a number of countries and strong interest of the automotive enterprises, I suppose that electric vehicles will become more attractive and would be able to substitute the ICE vehicles in the next 20 years. Therefore, each contribution to the field of battery technology is a valuable asset, helping the society move forward to the emission-free future. Finally, I hope that the current work will not remain as a pile of papers but become a useful brochure for other researches, working on the similar topics.

LIST OF TABLES

LIST OF FIGURES

REFERENCES

1. Blomgren, G.E., *The Development and Future of Lithium Ion Batteries.* Journal of The Electrochemical Society, 2017. **164**(1): p. A5019-A5025.
2. Scrosati, B. and J. Garche, *Lithium batteries: Status, prospects and future.* Journal of Power Sources, 2010. **195**(9): p. 2419-2430.
3. *Lithium Batteries: The Pros and Cons.* 15.08.2017]; Available from: http://electronics360.globalspec.com/article/5555/lithium-batteries-the-pros-and-cons.
4. *Lithium-ion Battery Costs: Squeezed Margins and New Business Models.* 23.09.2017]; Available from: Lithium-ion Battery Costs: Squeezed Margins and New Business Models.
5. Wood Iii, D.L., J. Li, and C. Daniel, *Prospects for reducing the processing cost of lithium ion batteries.* Journal of Power Sources, 2015. **275**: p. 234-242.
6. Kalhoff, J., et al., *Safer Electrolytes for Lithium-Ion Batteries: State of the Art and Perspectives.* ChemSusChem, 2015. **8**(13): p. 2154-2175.
7. Tarascon, J.M. and M. Armand, *Issues and challenges facing rechargeable lithium batteries.* Nature, 2001. **414**(6861): p. 359-367.
8. PILLOT, C., *Battery Market Development for Consumer Electronics, Automotive, and Industrial: Materials Requirements and Trends.* 2015.
9. Katona, V. *When Will Russia Run Out Of Oil?* Oilprice.com 2017 03.09.2017]; Available from: http://oilprice.com/Energy/Crude-Oil/When-Will-Russia-Run-Out-Of-Oil.html.
10. *Russia prepared to cut greenhouse gas emissions to 70% by 2030.* 03.09.2017]; Available from: https://www.rbth.com/news/2015/12/10/russia-prepared-to-cut-greenhouse-gas-emissions-to-70-by-2030_549469.
11. Brummer, S., et al., *Materials for Advanced Batteries.* edited by DW Murphy, J. Broadhead and BCH Steele, Plenum Press, New York, 1980: p. 123.
12. Zhang, S.S., *A review on the separators of liquid electrolyte Li-ion batteries.* Journal of Power Sources, 2007. **164**(1): p. 351-364.
13. An, S.J., et al., *The state of understanding of the lithium-ion-battery graphite solid electrolyte interphase (SEI) and its relationship to formation cycling.* Carbon, 2016. **105**: p. 52-76.
14. Armand, M., J. Chabagno, and N. Duclot, in *Fast ion transport in solids*, M. Vashishta, Editor. 1979: Shenoy (North-Holland, Amsterdam). p. 131.
15. Fong, R., U. von Sacken, and J.R. Dahn, *Studies of Lithium Intercalation into Carbons Using Nonaqueous Electrochemical Cells.* Journal of The Electrochemical Society, 1990. **137**(7): p. 2009-2013.
16. Edström, K., T. Gustafsson, and J.O. Thomas, *The cathode–electrolyte interface in the Li-ion battery.* Electrochimica Acta, 2004. **50**(2–3): p. 397-403.
17. Liu, Y.-M., et al., *Characterization of the Cathode Electrolyte Interface in Lithium Ion Batteries by Desorption Electrospray Ionization Mass Spectrometry.* Analytical Chemistry, 2016. **88**(14): p. 7171-7177.
18. Aurbach, D., et al., *A short review of failure mechanisms of lithium metal and lithiated graphite anodes in liquid electrolyte solutions.* Solid State Ionics, 2002. **148**(3–4): p. 405-416.
19. Dahn, J., et al., *Lithium Batteries: New Materials, Developments and Perspectives 1994.* Elsevier, Amsterdam.
20. Liu, Z., et al., *Interfacial Study on Solid Electrolyte Interphase at Li Metal Anode: Implication for Li Dendrite Growth.* Journal of The Electrochemical Society, 2016. **163**(3): p. A592-A598.
21. Zaban, A. and D. Aurbach, *Impedance spectroscopy of lithium and nickel electrodes in propylene carbonate solutions of different lithium salts A comparative study.* Journal of Power Sources, 1995. **54**(2): p. 289-295.
22. Aurbach, D., et al., *The electrochemical behaviour of 1,3-dioxolane—LiClO4 solutions—I. Uncontaminated solutions.* Electrochimica Acta, 1990. **35**(3): p. 625-638.
23. Aurbach, D., et al., *Recent studies of the lithium-liquid electrolyte interface Electrochemical, morphological and spectral studies of a few important systems.* Journal of Power Sources, 1995. **54**(1): p. 76-84.
24. Aurbach, D., et al., *The behaviour of lithium electrodes in propylene and ethylene carbonate: Te major factors that influence Li cycling efficiency.* Journal of Electroanalytical Chemistry, 1992. **339**(1): p. 451-471.
25. Butler, J.N., D.R. Cogley, and J.C. Synnott, *Effect of water on the kinetics of the solid lithium-lithium ion reaction in propylene carbonate.* The Journal of Physical Chemistry, 1969. **73**(11): p. 4026-4027.

26. Morita, M., S. Aoki, and Y. Matsuda, *ac imepedance behaviour of lithium electrode in organic electrolyte solutions containing additives.* Electrochimica Acta, 1992. **37**(1): p. 119-123.

27. Mogi, R., et al., *Effects of Some Organic Additives on Lithium Deposition in Propylene Carbonate.* Journal of The Electrochemical Society, 2002. **149**(12): p. A1578-A1583.

28. Ding, M.S., S.L. Koch, and S. Passerini, *The Effect of 1-Pentylamine as Solid Electrolyte Interphase Precursor on Lithium Metal Anodes.* Electrochimica Acta, 2017. **240**: p. 408-414.

29. Li, N.-W., et al., *An Artificial Solid Electrolyte Interphase Layer for Stable Lithium Metal Anodes.* Advanced Materials, 2016. **28**(9): p. 1853-1858.

30. Brissot, C., et al., *Dendritic growth mechanisms in lithium/polymer cells.* Journal of Power Sources, 1999. **81**: p. 925-929.

31. Matsui, T. and K. Takeyama, *Lithium deposit morphology from polymer electrolytes.* Electrochimica Acta, 1995. **40**(13): p. 2165-2169.

32. Nitta, N., et al., *Li-ion battery materials: present and future.* Materials Today, 2015. **18**(5): p. 252-264.

33. Kumar, T.P., T.S.D. Kumari, and M.A. Stephan, *Carbonaceous anode materials for lithium-ion batteries–the road ahead.* Journal of the Indian Institute of Science, 2012. **89**(4): p. 393-424.

34. Sivakkumar, S.R., J.Y. Nerkar, and A.G. Pandolfo, *Rate capability of graphite materials as negative electrodes in lithium-ion capacitors.* Electrochimica Acta, 2010. **55**(9): p. 3330-3335.

35. Mochida, I., S.-H. Yoon, and W. Qiao, *Catalysts in syntheses of carbon and carbon precursors.* Journal of the Brazilian Chemical Society, 2006. **17**: p. 1059-1073.

36. Sato, K., et al., *A mechanism of lithium storage in disordered carbons.* Science, 1994. **264**(5158): p. 556-559.

37. Buiel, E. and J.R. Dahn, *Li-insertion in hard carbon anode materials for Li-ion batteries.* Electrochimica Acta, 1999. **45**(1): p. 121-130.

38. Mabuchi, A., et al., *Charge-Discharge Characteristics of the Mesocarbon Miocrobeads Heat-Treated at Different Temperatures.* Journal of The Electrochemical Society, 1995. **142**(4): p. 1041-1046.

39. Zheng, T., J.S. Xue, and J.R. Dahn, *Lithium Insertion in Hydrogen-Containing Carbonaceous Materials.* Chemistry of Materials, 1996. **8**(2): p. 389-393.

40. Dahn, J.R., et al., *Mechanisms for Lithium Insertion in Carbonaceous Materials.* Science, 1995. **270**(5236): p. 590-593.

41. Wang, Z., S.M. Selbach, and T. Grande, *Van der Waals density functional study of the energetics of alkali metal intercalation in graphite.* RSC Advances, 2014. **4**(8): p. 4069-4079.

42. Luo, W., et al., *Na-Ion Battery Anodes: Materials and Electrochemistry.* Accounts of Chemical Research, 2016. **49**(2): p. 231-240.

43. Winter, M., et al., *Insertion Electrode Materials for Rechargeable Lithium Batteries.* Advanced Materials, 1998. **10**(10): p. 725-763.

44. Yan, J., et al., *A novel perspective on the formation of the solid electrolyte interphase on the graphite electrode for lithium-ion batteries.* Electrochimica Acta, 2010. **55**(5): p. 1785-1794.

45. Dahn, J.R., *Phase diagram of $\mathrm{Li}_{\mathit{x}}$$\mathrm{C}_{6}$.* Physical Review B, 1991. **44**(17): p. 9170-9177.

46. A.Herold, Bulletin de la Societe Chimique de France, 1955. **187**(999).

47. Ogumi, Z. and M. Inaba, *Electrochemical lithium intercalation within carbonaceous materials: intercalation processes, surface film formation, and lithium diffusion.* Bulletin of the Chemical Society of Japan, 1998. **71**(3): p. 521-534.

48. Endo, E., et al., *Electron Spin Resonance Study of the Electrochemical Reduction of Electrolyte Solutions for Lithium Secondary Batteries.* Journal of The Electrochemical Society, 1998. **145**(11): p. 3757-3764.

49. Chusid, O., et al., *Electrochemical and spectroscopic studies of carbon electrodes in lithium battery electrolyte systems.* Journal of Power Sources, 1993. **43**(1): p. 47-64.

50. Besenhard, J.O., et al., *Filming mechanism of lithium-carbon anodes in organic and inorganic electrolytes.* Journal of Power Sources, 1995. **54**(2): p. 228-231.

51. Chung, G.C., et al., *Origin of Graphite Exfoliation An Investigation of the Important Role of Solvent Cointercalation.* Journal of The Electrochemical Society, 2000. **147**(12): p. 4391-4398.

52. Yamada, Y., et al., *Kinetics of Lithium Ion Transfer at the Interface between Graphite and Liquid Electrolytes: Effects of Solvent and Surface Film.* Langmuir, 2009. **25**(21): p. 12766-12770.

53. Xu, K., A. von Cresce, and U. Lee, *Differentiating Contributions to "Ion Transfer" Barrier from Interphasial Resistance and Li+ Desolvation at Electrolyte/Graphite Interface.* Langmuir, 2010. **26**(13): p. 11538-11543.

54. Verma, P., P. Maire, and P. Novák, *A review of the features and analyses of the solid electrolyte interphase in Li-ion batteries.* Electrochimica Acta, 2010. **55**(22): p. 6332-6341.

55. Aurbach, D., et al., *Failure and Stabilization Mechanisms of Graphite Electrodes.* The Journal of Physical Chemistry B, 1997. **101**(12): p. 2195-2206.

56. Chiang, P.-C.J., M.-S. Wu, and J.-C. Lin, *A Novel Dual-Current Formation Process for Advanced Lithium-Ion Batteries.* Electrochemical and Solid-State Letters, 2005. **8**(8): p. A423-A427.

57. Li, J., et al., *The effects of pulse charging on cycling characteristics of commercial lithium-ion batteries.* Journal of Power Sources, 2001. **102**(1–2): p. 302-309.

58. Vetter, J., et al., *Ageing mechanisms in lithium-ion batteries.* Journal of Power Sources, 2005. **147**(1–2): p. 269-281.

59. Huang, C., et al., *The effect of solid electrolyte interface formation conditions on the aging performance of Li-ion cells.* Journal of Solid State Electrochemistry, 2011. **15**(9): p. 1987-1995.

60. An, S.J., et al., *Fast formation cycling for lithium ion batteries.* Journal of Power Sources, 2017. **342**: p. 846-852.

61. Herstedt, M., L. Fransson, and K. Edström, *Rate capability of natural Swedish graphite as anode material in Li-ion batteries.* Journal of Power Sources, 2003. **124**(1): p. 191-196.

62. Sawai, K. and T. Ohzuku, *Factors Affecting Rate Capability of Graphite Electrodes for Lithium-Ion Batteries.* Journal of The Electrochemical Society, 2003. **150**(6): p. A674-A678.

63. Shim, J. and K.A. Striebel, *Effect of electrode density on cycle performance and irreversible capacity loss for natural graphite anode in lithium-ion batteries.* Journal of Power Sources, 2003. **119–121**: p. 934-937.

64. Li, F.-S., et al., *A Mechanically Robust and Highly Ion-Conductive Polymer-Blend Coating for High-Power and Long-Life Lithium-Ion Battery Anodes.* Advanced Materials, 2015. **27**(1): p. 130-137.

65. Nobili, F., et al., *Tin-coated graphite electrodes as composite anodes for Li-ion batteries. Effects of tin coatings thickness toward intercalation behavior.* Journal of Power Sources, 2012. **198**: p. 243-250.

66. Lee, H.-Y., et al., *Characteristics of carbon-coated graphite prepared from mixture of graphite and polyvinylchloride as anode materials for lithium ion batteries.* Journal of Power Sources, 2001. **101**(2): p. 206-212.

67. Ohta, N., et al., *Carbon-coated graphite for anode of lithium ion rechargeable batteries: Graphite substrates for carbon coating.* Journal of Power Sources, 2009. **194**(2): p. 985-990.

68. Nozaki, H., et al., *Carbon-coated graphite for anode of lithium ion rechargeable batteries: Carbon coating conditions and precursors.* Journal of Power Sources, 2009. **194**(1): p. 486-493.

69. Wang, C., et al., *Electrochemical performance of modified artificial graphite as anode material for lithium ion batteries.* Ionics, 2013. **19**(2): p. 221-226.

70. Inagaki, M., *Carbon coating for enhancing the functionalities of materials.* Carbon, 2012. **50**(9): p. 3247-3266.

71. Striebel, K.A., et al., *The effect of compression on natural graphite anode performance and matrix conductivity.* Journal of Power Sources, 2004. **134**(2): p. 241-251.

72. Jung, H.-G., et al., *A high-rate long-life Li4Ti5O12/Li[Ni0.45Co0.1Mn1.45]O4 lithium-ion battery.* 2011. **2**: p. 516.

73. Colbow, K.M., J.R. Dahn, and R.R. Haering, *Structure and electrochemistry of the spinel oxides LiTi2O4 and Li43Ti53O4.* Journal of Power Sources, 1989. **26**(3): p. 397-402.

74. Scharner, S., W. Weppner, and P. Schmid-Beurmann, *Evidence of Two-Phase Formation upon Lithium Insertion into the Li1.33Ti1.67 O 4 Spinel.* Journal of The Electrochemical Society, 1999. **146**(3): p. 857-861.

75. Belharouak, I., et al., *Performance Degradation and Gassing of Li4Ti5O12/LiMn2O4 Lithium-Ion Cells.* Journal of The Electrochemical Society, 2012. **159**(8): p. A1165-A1170.

76. Wang, G.J., et al., *Preparation and characteristic of carbon-coated Li4Ti5O12 anode material.* Journal of Power Sources, 2007. **174**(2): p. 1109-1112.

77. He, Y.-B., et al., *Gassing in Li(4)Ti(5)O(12)-based batteries and its remedy.* Scientific Reports, 2012. **2**: p. 913.

78. Obrovac, M.N. and L. Christensen, *Structural Changes in Silicon Anodes during Lithium Insertion/Extraction.* Electrochemical and Solid-State Letters, 2004. **7**(5): p. A93-A96.

79. Li, H., et al., *A High Capacity Nano‐Si Composite Anode Material for Lithium Rechargeable Batteries.* Electrochemical and Solid-State Letters, 1999. **2**(11): p. 547-549.

80. Zhang, H., et al., *Hollow Si/C composite as anode material for high performance lithium-ion battery.* Powder Technology.

81. Yang, J., et al., *Si/C Composites for High Capacity Lithium Storage Materials.* Electrochemical and Solid-State Letters, 2003. **6**(8): p. A154-A156.

82. Li, X., et al., *Hollow core-shell structured porous Si-C nanocomposites for Li-ion battery anodes.* Journal of Materials Chemistry, 2012. **22**(22): p. 11014-11017.

83. Liu, N., et al., *A pomegranate-inspired nanoscale design for large-volume-change lithium battery anodes.* Nat Nano, 2014. **9**(3): p. 187-192.

84. Poizot, P., et al., *Nano-sized transition-metal oxides as negative-electrode materials for lithium-ion batteries.* Nature, 2000. **407**(6803): p. 496-499.

85. Palacin, M.R., *Recent advances in rechargeable battery materials: a chemist's perspective.* Chemical Society Reviews, 2009. **38**(9): p. 2565-2575.

86. Nitta, N. and G. Yushin, *High-Capacity Anode Materials for Lithium-Ion Batteries: Choice of Elements and Structures for Active Particles.* Particle & Particle Systems Characterization, 2014. **31**(3): p. 317-336.

87. Bruce, P.G., B. Scrosati, and J.-M. Tarascon, *Nanomaterials for Rechargeable Lithium Batteries.* Angewandte Chemie International Edition, 2008. **47**(16): p. 2930-2946.

88. Bresser, D., S. Passerini, and B. Scrosati, *Leveraging valuable synergies by combining alloying and conversion for lithium-ion anodes.* Energy & Environmental Science, 2016. **9**(11): p. 3348-3367.

89. Manthiram, A., et al., *Nanostructured electrode materials for electrochemical energy storage and conversion.* Energy & Environmental Science, 2008. **1**(6): p. 621-638.

90. Padhi, A.K., K.S. Nanjundaswamy, and J.B. Goodenough, *Phospho-olivines as Positive-Electrode Materials for Rechargeable Lithium Batteries.* Journal of The Electrochemical Society, 1997. **144**(4): p. 1188-1194.

91. Whittingham, M.S., *Lithium Batteries and Cathode Materials.* Chemical Reviews, 2004. **104**(10): p. 4271-4302.

92. Wang, J. and X. Sun, *Understanding and recent development of carbon coating on LiFePO4 cathode materials for lithium-ion batteries.* Energy & Environmental Science, 2012. **5**(1): p. 5163-5185.

93. Lee, K.T. and K.S. Lee, *Electrochemical properties of LiFe0.9Mn0.1PO4/Fe2P cathode material by mechanical alloying.* Journal of Power Sources, 2009. **189**(1): p. 435-439.

94. Roberts, M.R., et al., *High Throughput Electrochemical Observation of Structural Phase Changes in LiFe1 − x Mn x PO4 during Charge and Discharge.* Journal of The Electrochemical Society, 2010. **157**(4): p. A381-A386.

95. Zheng, T., et al., *Lithium Insertion in High Capacity Carbonaceous Materials.* Journal of The Electrochemical Society, 1995. **142**(8): p. 2581-2590.

96. Du Pasquier, A., et al., *A comparative study of Li-ion battery, supercapacitor and nonaqueous asymmetric hybrid devices for automotive applications.* Journal of Power Sources, 2003. **115**(1): p. 171-178.

97. Palacín, M.R., et al., *Low-Temperature Synthesis of LiNiO2 : Reaction Mechanism, Stability, and Electrochemical Properties.* Journal of The Electrochemical Society, 1997. **144**(12): p. 4226-4236.

98. Gu, M., et al., *Formation of the Spinel Phase in the Layered Composite Cathode Used in Li-Ion Batteries.* ACS Nano, 2013. **7**(1): p. 760-767.

99. Jaber-Ansari, L., et al., *Suppressing Manganese Dissolution from Lithium Manganese Oxide Spinel Cathodes with Single-Layer Graphene.* Advanced Energy Materials, 2015. **5**(17): p. 1500646-n/a.

100. Gowda, S.R., et al., *Oxidation state of cross-over manganese species on the graphite electrode of lithium-ion cells.* Physical Chemistry Chemical Physics, 2014. **16**(15): p. 6898-6902.

101. Zheng, H., et al., *Correlation between dissolution behavior and electrochemical cycling performance for LiNi1/3Co1/3Mn1/3O2-based cells.* Journal of Power Sources, 2012. **207**: p. 134-140.

102. Liu, Q., et al., *Phase conversion and morphology evolution during hydrothermal preparation of orthorhombic LiMnO2 nanorods for lithium ion battery application.* Journal of Power Sources, 2007. **173**(1): p. 538-544.

103. Kakuda, T., et al., *Electrochemical performance of Al-doped LiMn2O4 prepared by different methods in solid-state reaction.* Journal of Power Sources, 2007. **167**(2): p. 499-503.

104. Lee, S., et al., *Carbon-Coated Single-Crystal LiMn2O4 Nanoparticle Clusters as Cathode Material for High-Energy and High-Power Lithium-Ion Batteries.* Angewandte Chemie International Edition, 2012. **51**(35): p. 8748-8752.

105. Marcinek, M., et al., *Electrolytes for Li-ion transport – Review.* Solid State Ionics, 2015. **276**: p. 107-126.

106. Xu, K., *Nonaqueous Liquid Electrolytes for Lithium-Based Rechargeable Batteries.* Chemical Reviews, 2004. **104**(10): p. 4303-4418.

107. Owen, B.B., et al., *THE DIELECTRIC CONSTANT OF WATER AS A FUNCTION OF TEMPERATURE AND PRESSURE1,2.* The Journal of Physical Chemistry, 1961. **65**(11): p. 2065-2070.

108. Harris, W.S., *Electrochemical studies in cyclic esters*. 1958, California Univ., Berkeley, CA (US). Radiation Lab.

109. Besenhard, J.O., *Handbook of battery materials*. 2008: John Wiley & Sons.

110. Aurbach, D., M. Koltypin, and H. Teller, *In Situ AFM Imaging of Surface Phenomena on Composite Graphite Electrodes during Lithium Insertion.* Langmuir, 2002. **18**(23): p. 9000-9009.

111. Nakamura, H., H. Komatsu, and M. Yoshio, *Suppression of electrochemical decomposition of propylene carbonate at a graphite anode in lithium-ion cells.* Journal of Power Sources, 1996. **62**(2): p. 219-222.

112. Xu, K., M.S. Ding, and T.R. Jow, *Quaternary Onium Salts as Nonaqueous Electrolytes for Electrochemical Capacitors.* Journal of The Electrochemical Society, 2001. **148**(3): p. A267-A274.

113. Yang, C.R., Y.Y. Wang, and C.C. Wan, *Composition analysis of the passive film on the carbon electrode of a lithium-ion battery with an EC-based electrolyte.* Journal of Power Sources, 1998. **72**(1): p. 66-70.

114. Wang, Z.-C., et al., *Fluoroethylene Carbonate as an Electrolyte Additive for Improving the Performance of Mesocarbon Microbead Electrode.* ECS Transactions, 2012. **41**(41): p. 29-40.

115. Markevich, E., G. Salitra, and D. Aurbach, *Fluoroethylene Carbonate as an Important Component for the Formation of an Effective Solid Electrolyte Interphase on Anodes and Cathodes for Advanced Li-Ion Batteries.* ACS Energy Letters, 2017. **2**(6): p. 1337-1345.

116. McMillan, R., et al., *Fluoroethylene carbonate electrolyte and its use in lithium ion batteries with graphite anodes.* Journal of Power Sources, 1999. **81**: p. 20-26.

117. Markevich, E., et al., *Fluoroethylene Carbonate as an Important Component in Electrolyte Solutions for High-Voltage Lithium Batteries: Role of Surface Chemistry on the Cathode.* Langmuir, 2014. **30**(25): p. 7414-7424.

118. Lin, Y.-M., et al., *High performance silicon nanoparticle anode in fluoroethylene carbonate-based electrolyte for Li-ion batteries.* Chemical Communications, 2012. **48**(58): p. 7268-7270.

119. Etacheri, V., et al., *Effect of Fluoroethylene Carbonate (FEC) on the Performance and Surface Chemistry of Si-Nanowire Li-Ion Battery Anodes.* Langmuir, 2012. **28**(1): p. 965-976.

120. Nie, M., et al., *Silicon Solid Electrolyte Interphase (SEI) of Lithium Ion Battery Characterized by Microscopy and Spectroscopy.* The Journal of Physical Chemistry C, 2013. **117**(26): p. 13403-13412.

121. Leung, K., et al., *Modeling Electrochemical Decomposition of Fluoroethylene Carbonate on Silicon Anode Surfaces in Lithium Ion Batteries.* Journal of The Electrochemical Society, 2014. **161**(3): p. A213-A221.

122. Shkrob, I.A., K.Z. Pupek, and D.P. Abraham, *Allotropic Control: How Certain Fluorinated Carbonate Electrolytes Protect Aluminum Current Collectors by Promoting the Formation of Insoluble Coordination Polymers.* The Journal of Physical Chemistry C, 2016. **120**(33): p. 18435-18444.

123. Aravindan, V., et al., *Lithium-Ion Conducting Electrolyte Salts for Lithium Batteries.* Chemistry – A European Journal, 2011. **17**(51): p. 14326-14346.

124. Han, H.-B., et al., *Lithium bis(fluorosulfonyl)imide (LiFSI) as conducting salt for nonaqueous liquid electrolytes for lithium-ion batteries: Physicochemical and electrochemical properties.* Journal of Power Sources, 2011. **196**(7): p. 3623-3632.

125. Dahbi, M., et al., *Interfacial Properties of LiTFSI and LiPF6-Based Electrolytes in Binary and Ternary Mixtures of Alkylcarbonates on Graphite Electrodes and Celgard Separator.* Industrial & Engineering Chemistry Research, 2012. **51**(14): p. 5240-5245.

126. Burns, J.C., et al., *Impedance Reducing Additives and Their Effect on Cell Performance: I. LiN(CF3SO2)2.* Journal of The Electrochemical Society, 2012. **159**(7): p. A1095-A1104.

127. Moretti, A., et al., *Li-doped N-methoxyethyl-N-methylpyrrolidinium fluorosulfonyl-(trifluoromethanesulfonyl)imide as electrolyte for reliable lithium ion batteries.* Journal of Power Sources, 2014. **269**: p. 645-650.

128. Nie, M. and B.L. Lucht, *Role of Lithium Salt on Solid Electrolyte Interface (SEI) Formation and Structure in Lithium Ion Batteries.* Journal of The Electrochemical Society, 2014. **161**(6): p. A1001-A1006.

129. Younesi, R., et al., *Lithium salts for advanced lithium batteries: Li-metal, Li-O2, and Li-S.* Energy & Environmental Science, 2015. **8**(7): p. 1905-1922.

130. J. Kalhoff, et al., *Enabling LiTFSI-based electrolytes for safer lithium-ion batteries.* ChemSusChem, 2014.

131. Dahbi, M., et al., *Comparative study of EC/DMC LiTFSI and LiPF6 electrolytes for electrochemical storage.* Journal of Power Sources, 2011. **196**(22): p. 9743-9750.

132. Zhang, S.S., *A review on electrolyte additives for lithium-ion batteries.* Journal of Power Sources, 2006. **162**(2): p. 1379-1394.

133. Aurbach, D., et al., *On the use of vinylene carbonate (VC) as an additive to electrolyte solutions for Li-ion batteries.* Electrochimica Acta, 2002. **47**(9): p. 1423-1439.

134. Ota, H., et al., *Analysis of Vinylene Carbonate Derived SEI Layers on Graphite Anode.* Journal of The Electrochemical Society, 2004. **151**(10): p. A1659-A1669.

135. Xia, J., et al., *Combinations of Ethylene Sulfite (ES) and Vinylene Carbonate (VC) as Electrolyte Additives in Li(Ni1/3Mn1/3Co1/3)O2/Graphite Pouch Cells.* Journal of The Electrochemical Society, 2014. **161**(6): p. A1149-A1157.

136. El Ouatani, L., et al., *The Effect of Vinylene Carbonate Additive on Surface Film Formation on Both Electrodes in Li-Ion Batteries.* Journal of The Electrochemical Society, 2009. **156**(2): p. A103-A113.

137. El Ouatani, L., et al., *Effect of Vinylene Carbonate Additive in Li-Ion Batteries: Comparison of LiCoO2∕C , LiFePO4∕C , and LiCoO2/Li4Ti5O12 Systems.* Journal of The Electrochemical Society, 2009. **156**(6): p. A468-A477.

138. Burns, J.C., et al., *Evaluation of Effects of Additives in Wound Li-Ion Cells Through High Precision Coulometry.* Journal of The Electrochemical Society, 2011. **158**(3): p. A255-A261.

139. Wang, D.Y., et al., *Effect of Mixtures of Lithium Hexafluorophosphate (LiPF6) and Lithium Bis(fluorosulfonyl)imide (LiFSI) as Salts in Li[Ni1/3Mn1/3Co1/3]O2/Graphite Pouch Cells.* Journal of The Electrochemical Society, 2015. **162**(1): p. A169-A175.

140. *Bollore Official Webpage.* 22.12.2015]; Available from: http://www.bollore.com/en-us.

141. autolib. *A UNIQUE TECHNOLOGY FOR SMART ENERGY MANAGEMENT.* [cited 2016 17.11]; Available from: https://www.autolib.eu/en/our-commitment/bluecar-menu-en/100-electric/.

142. Gorecki, W., et al., *Physical properties of solid polymer electrolyte PEO(LiTFSI) complexes.* Journal of Physics: Condensed Matter, 1995. **7**(34): p. 6823.

143. Dokko, K., et al., *Solvate Ionic Liquids for Lithium–Sulfur Batteries.* Meeting Abstracts, 2014. **MA2014-04**(3): p. 540.

144. Croce, F., et al., *Nanocomposite polymer electrolytes for lithium batteries.* Nature, 1998. **394**(6692): p. 456-458.

145. Marzantowicz, M., et al., *Phase segregation phenomena in poly(ethylene oxide):LiN(CF3SO2)2 electrolyte studied by local Raman spectroscopy.* Electrochimica Acta, 2010. **55**(19): p. 5446-5452.

146. Kim, G.T., et al., *UV cross-linked, lithium-conducting ternary polymer electrolytes containing ionic liquids.* Journal of Power Sources, 2010. **195**(18): p. 6130-6137.

147. Shin, J.-H., W.A. Henderson, and S. Passerini, *Ionic liquids to the rescue? Overcoming the ionic conductivity limitations of polymer electrolytes.* Electrochemistry Communications, 2003. **5**(12): p. 1016-1020.

148. de Vries, H., S. Jeong, and S. Passerini, *Ternary polymer electrolytes incorporating pyrrolidinium-imide ionic liquids.* RSC Advances, 2015. **5**(18): p. 13598-13606.

149. Sun, H.Y., et al., *Ferroelectric Materials as a Ceramic Filler in Solid Composite Polyethylene Oxide-Based Electrolytes.* Journal of The Electrochemical Society, 2000. **147**(7): p. 2462-2467.

150. Croce, F., et al., *Role of the ceramic fillers in enhancing the transport properties of composite polymer electrolytes.* Electrochimica Acta, 2001. **46**(16): p. 2457-2461.

151. Appetecchi, G.B., et al., *Transport and interfacial properties of composite polymer electrolytes.* Electrochimica Acta, 2000. **45**(8–9): p. 1481-1490.

152. Mueller, F., et al., *Influence of the carbonaceous conductive network on the electrochemical performance of ZnFe2O4 nanoparticles.* Journal of Power Sources, 2013. **236**: p. 87-94.

153. Wetjen, M., et al., *Thermal and electrochemical properties of PEO-LiTFSI-Pyr14TFSI-based composite cathodes, incorporating 4 V-class cathode active materials.* Journal of Power Sources, 2014. **246**(0): p. 846-857.

154. Kim, G.-T., et al., *Solvent-free, PYR1ATFSI ionic liquid-based ternary polymer electrolyte systems: I. Electrochemical characterization.* Journal of Power Sources, 2007. **171**(2): p. 861-869.

155. Lasia, A., *Definition of Impedance and Impedance of Electrical Circuits*, in *Electrochemical Impedance Spectroscopy and its Applications*. 2014, Springer New York: New York, NY. p. 7-66.

156. Ruhi, G. and S.K. Dhawan, *Conducting Polymer Nano Composite Epoxy Coatings for Anticorrosive Applications*, in *Modern Electrochemical Methods in Nano, Surface and Corrosion Science*, M. Aliofkhazraei, Editor. 2014, InTech: Rijeka. p. Ch. 05.

157. Sekar N, R.R., *lectrochemical Impedance Spectroscopy for Microbial Fuel Cell Characterization.* J Microb Biochem Technol, 2013.

158.   *Differential Scanning Calorimetry.* 26.09.2017]; Available from: http://archive.cnx.org/contents/f443169d-16c3-402f-9712-17a994953365@2/differential-scanning-calorimetry-dsc.

159.   Sharova, V., et al., *Quaternary Polymer Electrolytes Containing an Ionic Liquid and a Ceramic Filler.* Macromolecular Rapid Communications, 2016. **37**(14): p. 1188-1193.

160.   Sharova, V., et al., *Evaluation of Carbon-Coated Graphite as a Negative Electrode Material for Li-Ion Batteries.* C, 2017. **3**(3): p. 22.

161.   Shin, J.-H., W.A. Henderson, and S. Passerini, *PEO-Based Polymer Electrolytes with Ionic Liquids and Their Use in Lithium Metal-Polymer Electrolyte Batteries.* Journal of The Electrochemical Society, 2005. **152**(5): p. A978-A983.

162.   Lu, Z., L. Yang, and Y. Guo, *Thermal behavior and decomposition kinetics of six electrolyte salts by thermal analysis.* Journal of Power Sources, 2006. **156**(2): p. 555-559.

163.   Borodin, O. and G.D. Smith, *Molecular Dynamics Simulations of Poly(ethylene oxide)/LiI Melts. 2. Dynamic Properties.* Macromolecules, 2000. **33**(6): p. 2273-2283.

164.   Timachova, K., H. Watanabe, and N.P. Balsara, *Effect of Molecular Weight and Salt Concentration on Ion Transport and the Transference Number in Polymer Electrolytes.* Macromolecules, 2015. **48**(21): p. 7882-7888.

165.   Joost, M., et al., *Ionic mobility in ternary polymer electrolytes for lithium-ion batteries.* Electrochimica Acta, 2012. **86**(0): p. 330-338.

166.   Ji, K.-S., et al., *Role of functional nano-sized inorganic fillers in poly(ethylene) oxide-based polymer electrolytes.* Journal of Power Sources, 2003. **117**(1–2): p. 124-130.

167.   Rupp, B., et al., *Polymer electrolyte for lithium batteries based on photochemically crosslinked poly(ethylene oxide) and ionic liquid.* European Polymer Journal, 2008. **44**(9): p. 2986-2990.

168.   Pawlicka, A. and J.P. Donoso, *3 - Polymer electrolytes based on natural polymers*, in *Polymer Electrolytes*, C. Sequeira and D. Santos, Editors. 2010, Woodhead Publishing. p. 95-128.

169.   Henderson, W.A. and S. Passerini, *Phase Behavior of Ionic Liquid−LiX Mixtures: Pyrrolidinium Cations and TFSI- Anions.* Chemistry of Materials, 2004. **16**(15): p. 2881-2885.

170.   Eschen, T., et al., *Ionic Transport in Polymer Electrolytes Based on PEO and the PMImI Ionic Liquid: Effects of Salt Concentration and Iodine Addition.* The Journal of Physical Chemistry B, 2012. **116**(28): p. 8290-8298.

171.   Diddens, D. and A. Heuer, *Lithium Ion Transport Mechanism in Ternary Polymer Electrolyte-Ionic Liquid Mixtures: A Molecular Dynamics Simulation Study.* ACS Macro Letters, 2013. **2**(4): p. 322-326.

172.   Rey, I., et al., *Spectroscopic and Theoretical Study of (CF3SO2)2N- (TFSI-) and (CF3SO2)2NH (HTFSI).* The Journal of Physical Chemistry A, 1998. **102**(19): p. 3249-3258.

173.   Rey, I., et al., *Infrared and Raman study of the PEO-LiTFSI polymer electrolyte.* Electrochimica Acta, 1998. **43**(10–11): p. 1505-1510.

174.   Edman, L., *Ion Association and Ion Solvation Effects at the Crystalline−Amorphous Phase Transition in PEO−LiTFSI.* The Journal of Physical Chemistry B, 2000. **104**(31): p. 7254-7258.

175.   Barpanda, P., et al., *LiZnSO4F Made in an Ionic Liquid: A Ceramic Electrolyte Composite for Solid-State Lithium Batteries.* Angewandte Chemie International Edition, 2011. **50**(11): p. 2526-2531.

176.   Wetjen, M., et al., *Temperature dependence of electrochemical properties of cross-linked poly(ethylene oxide)–lithium bis(trifluoromethanesulfonyl)imide–N-butyl-N-methylpyrrolidinium bis(trifluoromethanesulfonyl)imide solid polymer electrolytes for lithium batteries.* Electrochimica Acta, 2013. **87**(0): p. 779-787.

177.   Grande, L., et al., *Li/air Flow Battery Employing Ionic Liquid Electrolytes.* Energy Technology, 2015: p. n/a-n/a.

178.   De Vos, N., C. Maton, and C.V. Stevens, *Electrochemical Stability of Ionic Liquids: General Influences and Degradation Mechanisms.* ChemElectroChem, 2014. **1**(8): p. 1258-1270.

179.   Mousavi, M.P.S., et al., *Unbiased Quantification of the Electrochemical Stability Limits of Electrolytes and Ionic Liquids.* Journal of The Electrochemical Society, 2015. **162**(12): p. A2250-A2258.

180.   Delp, S.A., et al., *Importance of Reduction and Oxidation Stability of High Voltage Electrolytes and Additives.* Electrochimica Acta, 2016. **209**: p. 498-510.

181.   Simonetti, E., et al., *Towards Li(Ni0.33Mn0.33Co0.33)O2/graphite batteries with ionic liquid-based electrolytes. I. Electrodes' behavior in lithium half-cells.* Journal of Power Sources, 2016. **331**: p. 426-434.

182.   Eshetu, G.G., et al., *In-Depth Interfacial Chemistry and Reactivity Focused Investigation of Lithium–Imide- and Lithium–Imidazole-Based Electrolytes.* ACS Applied Materials & Interfaces, 2016. **8**(25): p. 16087-16100.

183. Philippe, B., et al., *Improved Performances of Nanosilicon Electrodes Using the Salt LiFSI: A Photoelectron Spectroscopy Study.* Journal of the American Chemical Society, 2013. **135**(26): p. 9829-9842.

184. Dedryvère, R., et al., *XPS Valence Characterization of Lithium Salts as a Tool to Study Electrode/Electrolyte Interfaces of Li-Ion Batteries.* The Journal of Physical Chemistry B, 2006. **110**(26): p. 12986-12992.

185. Ensling, D., et al., *A comparative XPS surface study of Li2FeSiO4/C cycled with LiTFSI- and LiPF6-based electrolytes.* Journal of Materials Chemistry, 2009. **19**(1): p. 82-88.

186. Ghimbeu, C.M., et al., *Influence of Graphite Characteristics on the Electrochemical Performance in Alkylcarbonate LiTFSI Electrolyte for Li-Ion Capacitors and Li-Ion Batteries.* Journal of The Electrochemical Society, 2013. **160**(10): p. A1907-A1915.

187. Kim, H., et al., *Ethylene bis-carbonates as telltales of SEI and electrolyte health, role of carbonate type and new additives.* Electrochimica Acta, 2014. **136**: p. 157-165.

188. Pan, Y., G. Wang, and B.L. Lucht, *Cycling performance and surface analysis of Lithium bis(trifluoromethanesulfonyl)imide in propylene carbonate with graphite.* Electrochimica Acta, 2016. **217**: p. 269-273.

189. Edström, K., M. Herstedt, and D.P. Abraham, *A new look at the solid electrolyte interphase on graphite anodes in Li-ion batteries.* Journal of Power Sources, 2006. **153**(2): p. 380-384.

190. Zhang, Q., et al., *Synergetic Effects of Inorganic Components in Solid Electrolyte Interphase on High Cycle Efficiency of Lithium Ion Batteries.* Nano Letters, 2016. **16**(3): p. 2011-2016.

191. Gaberscek, M., et al., *The Importance of Interphase Contacts in Li Ion Electrodes: The Meaning of the High-Frequency Impedance Arc.* Electrochemical and Solid-State Letters, 2008. **11**(10): p. A170-A174.

192. Dsoke, S., et al., *Strategies to reduce the resistance sources on Electrochemical Double Layer Capacitor electrodes.* Journal of Power Sources, 2013. **238**: p. 422-429.

193. Zhang, S.S., K. Xu, and T.R. Jow, *EIS study on the formation of solid electrolyte interface in Li-ion battery.* Electrochimica Acta, 2006. **51**(8–9): p. 1636-1640.

194. Zhang, S.S., *Electrochemical study of the formation of a solid electrolyte interface on graphite in a LiBC2O4F2-based electrolyte.* Journal of Power Sources, 2007. **163**(2): p. 713-718.

195. Umeda, M., et al., *Electrochemical impedance study of Li-ion insertion into mesocarbon microbead single particle electrode: Part I. Graphitized carbon.* Electrochimica Acta, 2001. **47**(6): p. 885-890.

196. Basu, S., et al., *Synthesis and properties of lithium-graphite intercalation compounds.* Materials Science and Engineering, 1979. **38**(3): p. 275-283.

197. Thomas, S., P.A. Soloman, and V.O. Rejini, *Preparation of Chitosan- CMC Blends and Studies on Thermal Properties.* Procedia Technology, 2016. **24**: p. 721-726.

198. Anyszka, R., et al., *Thermal Stability and Flammability of Styrene-Butadiene Rubber-Based (SBR) Ceramifiable Composites.* Materials, 2016. **9**(7): p. 604.

199. Borgel, V., et al., *On the application of ionic liquids for rechargeable Li batteries: High voltage systems.* Journal of Power Sources, 2009. **189**(1): p. 331-336.

200. Zheng, J., et al., *Research Progress towards Understanding the Unique Interfaces between Concentrated Electrolytes and Electrodes for Energy Storage Applications.* Advanced Science, 2017. **4**(8): p. 1700032-n/a.

201. Pan, J., Y.-T. Cheng, and Y. Qi, *General method to predict voltage-dependent ionic conduction in a solid electrolyte coating on electrodes.* Physical Review B, 2015. **91**(13): p. 134116.

202. Nie, M., et al., *Effect of Vinylene Carbonate and Fluoroethylene Carbonate on SEI Formation on Graphitic Anodes in Li-Ion Batteries.* Journal of The Electrochemical Society, 2015. **162**(13): p. A7008-A7014.

203. Michan, A.L., et al., *Fluoroethylene Carbonate and Vinylene Carbonate Reduction: Understanding Lithium-Ion Battery Electrolyte Additives and Solid Electrolyte Interphase Formation.* Chemistry of Materials, 2016. **28**(22): p. 8149-8159.

204. Agubra, V.A., et al., *Analysis of effects of the state of charge on the formation and growth of the deposit layer on graphite electrode of pouch type lithium ion polymer batteries.* Journal of Power Sources, 2014. **270**: p. 213-220.

205. Agubra, V.A. and J.W. Fergus, *The formation and stability of the solid electrolyte interface on the graphite anode.* Journal of Power Sources, 2014. **268**: p. 153-162.

206. Märkle, W., C.-Y. Lu, and P. Novák, *Morphology of the Solid Electrolyte Interphase on Graphite in Dependency on the Formation Current.* Journal of The Electrochemical Society, 2011. **158**(12): p. A1478-A1482.

207. Long, B.R., et al., *Enabling High-Energy, High-Voltage Lithium-Ion Cells: Standardization of Coin-Cell Assembly, Electrochemical Testing, and Evaluation of Full Cells.* Journal of The Electrochemical Society, 2016. **163**(14): p. A2999-A3009.

208. Ogihara, N., et al., *Theoretical and Experimental Analysis of Porous Electrodes for Lithium-Ion Batteries by Electrochemical Impedance Spectroscopy Using a Symmetric Cell.* Journal of The Electrochemical Society, 2012. **159**(7): p. A1034-A1039.

209. Juarez-Robles, D., et al., *Impedance Evolution Characteristics in Lithium-Ion Batteries.* Journal of The Electrochemical Society, 2017. **164**(4): p. A837-A847.

210. Sethuraman, V.A., et al., *Surface structural disordering in graphite upon lithium intercalation/deintercalation.* Journal of Power Sources, 2010. **195**(11): p. 3655-3660.

211. Wang, H., et al., *Characterization of Carbon-Coated Natural Graphite as a Lithium-Ion Battery Anode Material.* Journal of The Electrochemical Society, 2002. **149**(4): p. A499-A503.

212. Li, H. and H. Zhou, *Enhancing the performances of Li-ion batteries by carbon-coating: present and future.* Chemical Communications, 2012. **48**(9): p. 1201-1217.

213. Fu, L.J., et al., *Synthesis of carbon coated nanoporous microcomposite and its rate capability for lithium ion battery.* Microporous and Mesoporous Materials, 2009. **117**(1–2): p. 515-518.

214. Zhang, W.-M., et al., *Carbon Coated Fe3O4 Nanospindles as a Superior Anode Material for Lithium-Ion Batteries.* Advanced Functional Materials, 2008. **18**(24): p. 3941-3946.

215. Komaba, S., T. Ozeki, and K. Okushi, *Functional interface of polymer modified graphite anode.* Journal of Power Sources, 2009. **189**(1): p. 197-203.

216. Fang, W., et al., *A facile strategy to prepare nano-crystalline Li4Ti5O12/C anode material via polyvinyl alcohol as carbon source for high-rate rechargeable Li-ion batteries.* Electrochimica Acta, 2013. **93**: p. 173-178.

217. Ferrari, A.C. and J. Robertson, *Interpretation of Raman spectra of disordered and amorphous carbon.* Physical Review B, 2000. **61**(20): p. 14095-14107.

218. Ferrari, A.C., *Raman spectroscopy of graphene and graphite: Disorder, electron–phonon coupling, doping and nonadiabatic effects.* Solid State Communications, 2007. **143**(1–2): p. 47-57.

219. Pimenta, M.A., et al., *Studying disorder in graphite-based systems by Raman spectroscopy.* Physical Chemistry Chemical Physics, 2007. **9**(11): p. 1276-1290.

220. Wang, H. and M. Yoshio, *Carbon-coated natural graphite prepared by thermal vapor decomposition process, a candidate anode material for lithium-ion battery.* Journal of Power Sources, 2001. **93**(1–2): p. 123-129.

221. Yoshio, M., et al., *Effect of Carbon Coating on Electrochemical Performance of Treated Natural Graphite as Lithium-Ion Battery Anode Material.* Journal of The Electrochemical Society, 2000. **147**(4): p. 1245-1250.

222. *Battery University.* 15.08.2017]; Available from: http://batteryuniversity.com/learn/article/secondary_batteries.

223. *Batteries for Mobile Robots.* 15.08.2017]; Available from: http://www.inf.fu-berlin.de/lehre/WS02/robotik/Vorlesungen/Vorlesung5/ComparisonBattery.pdf.

APPENDIX 1

Table A1. Summary of the main characteristics of different rechargeable battery types (taken from Ref. [222, 223], available online).

Characteristic	Lead acid	NiCd	NiMH	Li-ion	Li-polymer
Gravimetric energy density (Wh/kg)	30-50	45-80	60-120	100-160	100-150
Volumetric energy density (Wh/L)	30-50	120	240	400-450	350-420
Cycle life (80% of initial capacity)	200-300	1,500	300-500	500-1000	300-500
Charge time, h	8-16	1-2	2-4	2-4	2-4
Self-discharge, month (RT)	5%	20%	30%	<5%	<5%
Cell voltage (V/cell)	2	1.25	1.25	3.6	3.6
Peak load current	5C	20C	5C	>2C	>2C
Operating temperature (discharge), °C	-20 – +60	-40 – +60	-20 – +60	-20 – +60	0 – +60
Toxicity	Very high	Very high	Low	Low	Low
Cost	Low	Moderate		High	High

Table A2. Protocols used to cycle half (a and b) and full (c) cells.

a) Half-cell: Graphite			
Test	Step	Conditions	Number of cycles
1st cycle	Dis	C/20 -> 0.01 V / CV <C/40 & 10h	1
	Ch	C/20 -> 1 V	
C-rate test	Dis	C/2 -> 0.01 V / CV <C/40 & 2h	3
	Ch	C/2 -> 1 V	
	Dis	C/2 -> 0.01 V / CV <C/40 & 2h	3
	Ch	1C -> 1 V	
	Dis	C/2 -> 0.01 V / CV <C/40 & 2h	1
	Ch	C/2 -> 1 V	
	Dis	C/2 -> 0.01 V / CV <C/40 & 2h	3
	Ch	2C -> 1 V	
	Dis	C/2 -> 0.01 V / CV <C/40 & 2h	1
	Ch	C/2 -> 1 V	
	Dis	C/2 -> 0.01 V / CV <C/40 & 2h	3
	Ch	3C -> 1 V	
	Dis	C/2 -> 0.01 V / CV <C/40 & 2h	1
	Ch	C/2 -> 1 V	
	Dis	C/2 -> 0.01 V / CV <C/40 & 2h	3
	Ch	10C -> 1 V	

	Dis	C/2 -> 0.01 V / CV <C/40 & 2h	1
	Ch	C/2 -> 1 V	
	Dis	C/2 -> 0.01 V / CV <C/40 & 2h	3
	Ch	20C -> 1V	
Cycle life test	Dis	C/2 -> 0.01 V / CV <C/40 & 2h	> 100
	Ch	C/2 -> 1 V	

b) Half-cell: LFP

Test	Step	Conditions	Number of cycles
1st cycle	Ch	C/10 -> 3.65 V / CV <C/20 & 2h	1
	Dis	C/10 -> 2.5 V	
C-rate test	Ch	C/3 -> 3.65 V / CV <C/20 & 1h	3
	Dis	C/3 -> 2.5 V	
	Ch	C/3 -> 3.65 V / CV <C/20 & 1h	3
	Dis	1C -> 2.5 V	
	Ch	C/3 -> 3.65 V / CV <C/20 & 1h	1
	Dis	C/3 -> 2.5 V	
	Ch	C/3 -> 3.65 V / CV <C/20 & 1h	3
	Dis	2C -> 2.5 V	
	Ch	C/3 -> 3.65 V / CV <C/20 & 1h	1
	Dis	C/3 -> 2.5 V	

Test	Step	Conditions	Number of cycles
	Ch	C/3 -> 3.65 V / CV <C/20 & 1h	3
	Dis	3C -> 2.5 V	
	Ch	C/3 -> 3.65 V / CV <C/20 & 1h	1
	Dis	C/3 -> 2.5 V	
	Ch	C/3 -> 3.65 V / CV <C/20 & 1h	3
	Dis	10C -> 2.5 V	
	Ch	C/3 -> 3.65 V / CV <C/20 & 1h	1
	Dis	C/3 -> 2.5 V	
	Ch	C/3 -> 3.65 V / CV <C/20 & 1h	3
	Dis	20C -> 2.5 V	
Cycle life test	Ch	C/3 -> 3.65 V / CV <C/20 & 1h	> 100
	Dis	C/2 -> 1 V	

c) Full cell: graphite/LFP

Test	Step	Conditions	Number of cycles
1st cycle	Ch	C/20 -> 3.6 V / CV <C/20 & 1h	1
	Dis	C/20 -> 2.5 V	
C-rate test	Ch	C/2 -> 3.6 V / CV <C/20 & 1h	3
	Dis	C/2 -> 2.5 V	
	Ch	1C -> 3.6 V / CV <C/20 & 1h	3
	Dis	1C -> 2.5 V	
	Ch	1C -> 3.6 V / CV <C/20 & 1h	3
	Dis	2C -> 2.5 V	

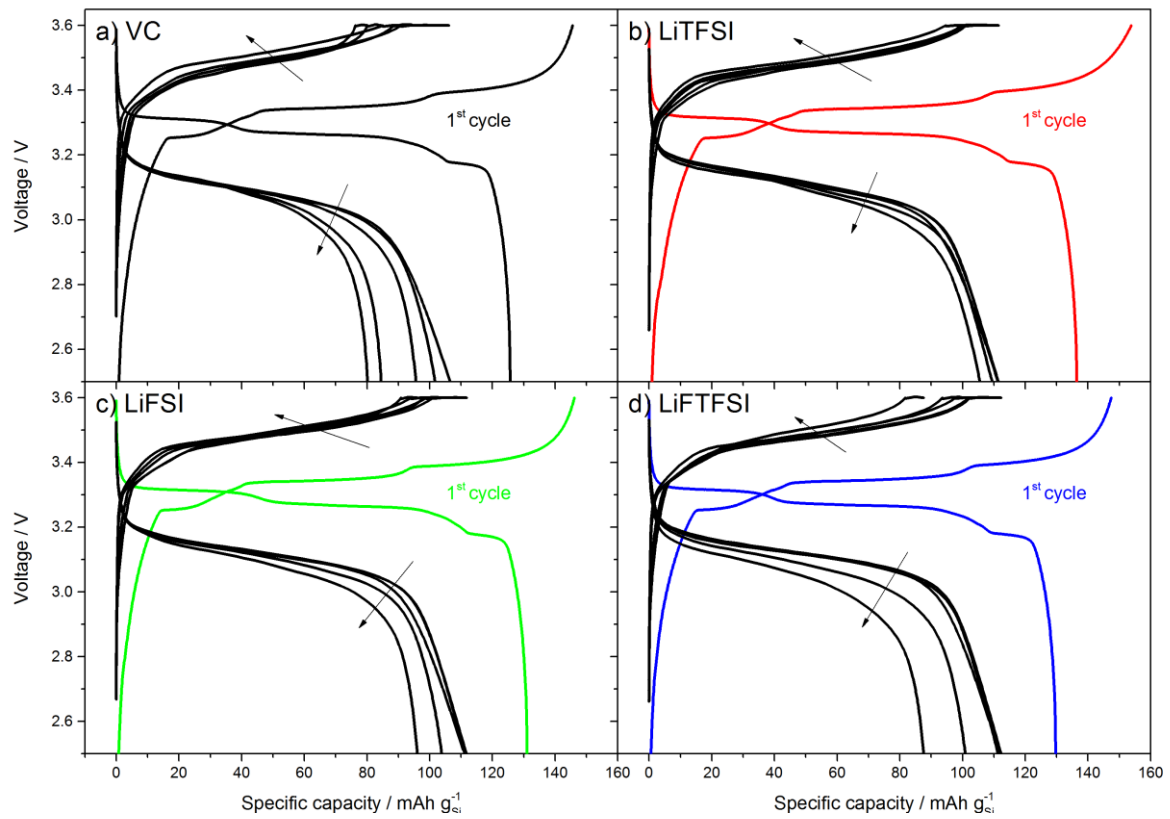|	Ch	1C -> 3.6 V / CV <C/20 & 1h	3
	Dis	3C -> 2.5 V	
Cycle life test	Ch	1C -> 3.6 V / CV <C/20 & 1h	> 100
	Dis	1C -> 2.5 V	

APPENDIX 2

Figure A1. Voltage profiles of the Li-ion cells with a) VC, b) LiTFSI, c) LiFSI, and d) LiFTFSI as the additives in the 1st, 15th, 50th, 100th, 500th and 900th galvanostatic cycles at 20 °C.
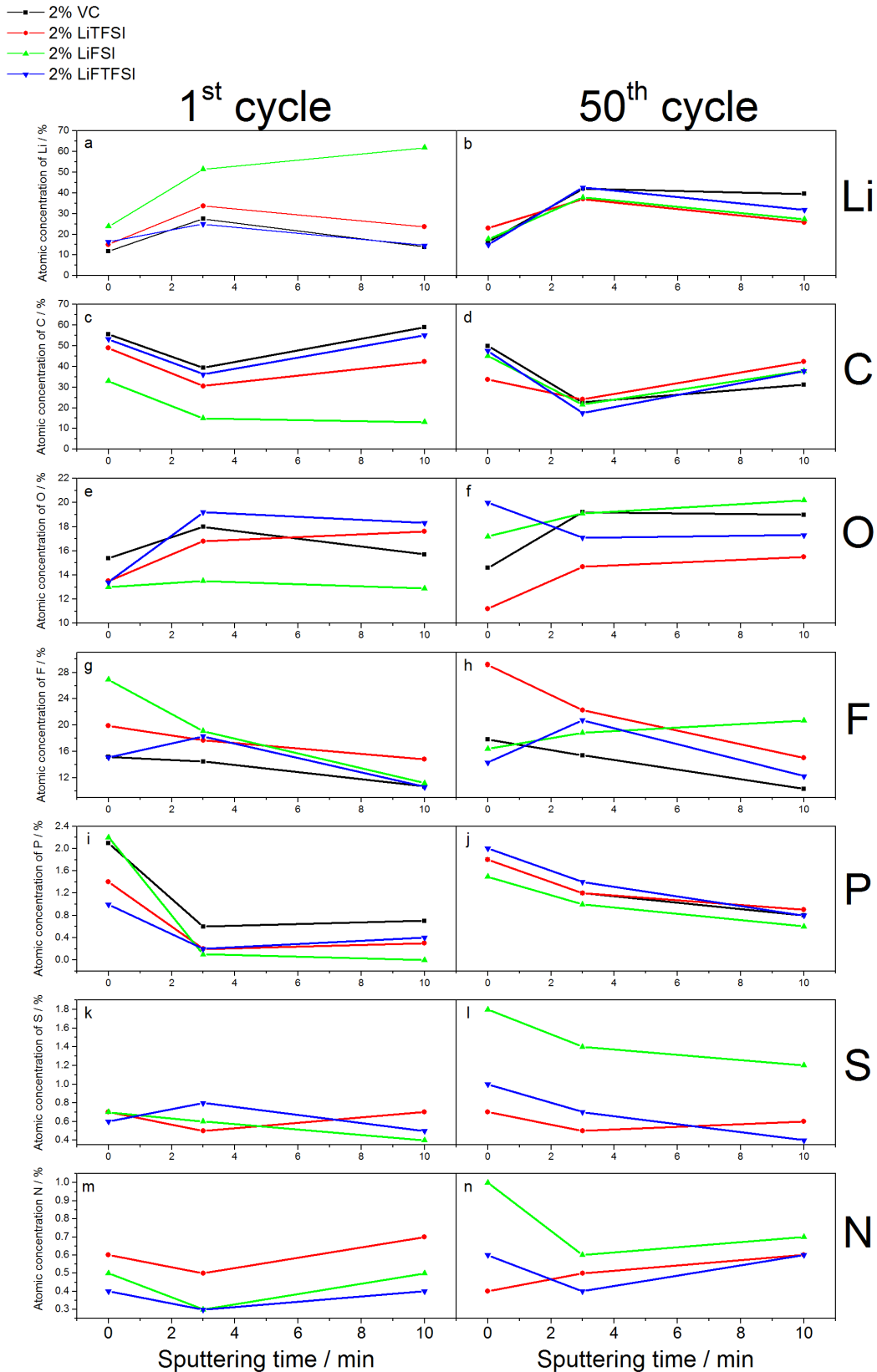
Figure A2. Evolution of the atomic concentrations of the elements as a function of sputtering time of graphite electrodes in contact with the various electrolytes (see legend) after the 1st or 50th galvanostatic cycle.
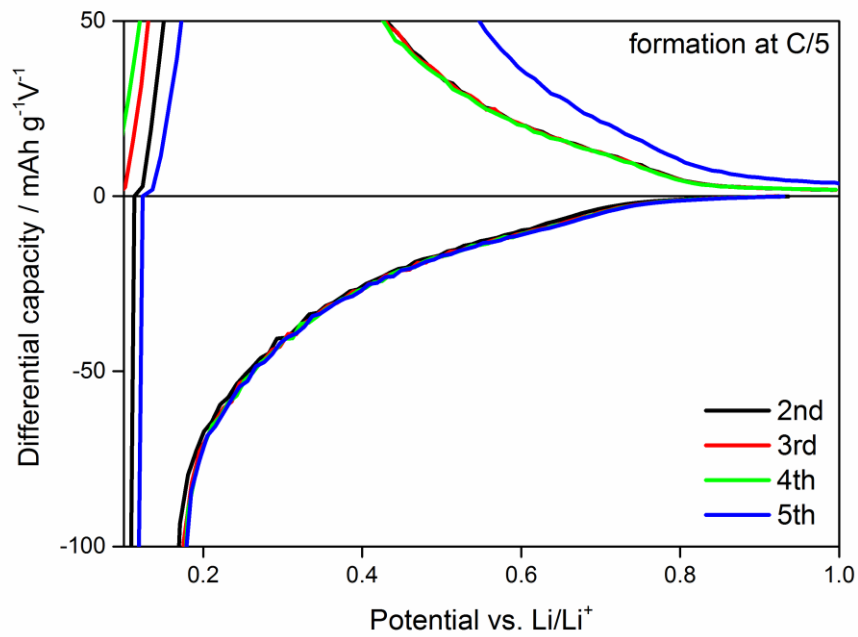
Figure A3. Differential capacity plots of the 2nd, 3rd, 4th (all at C/2) and 5th (1C) cycles after the formation at C/5 using 1M LiPF$_6$ in EC:DMC + 2 wt% FEC.
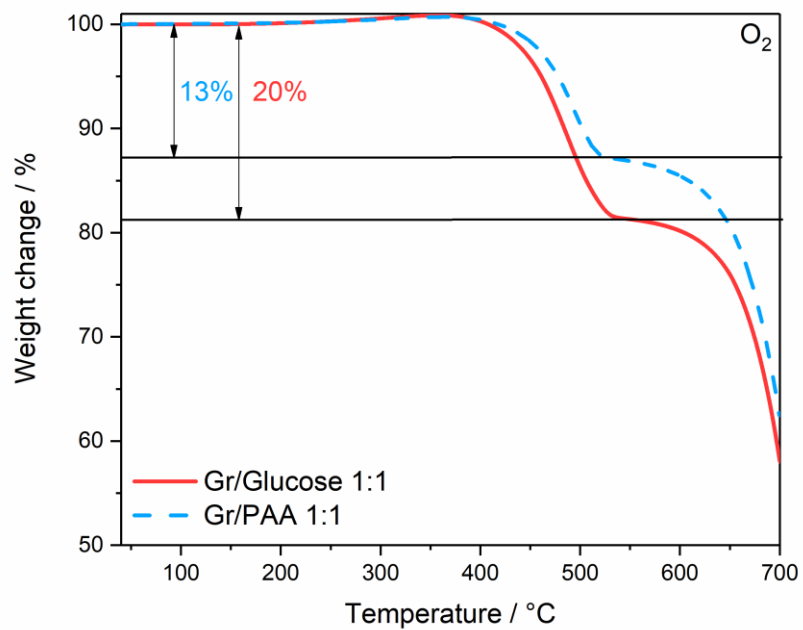

Figure A4. TGA traces of carbon-coated graphite materials using glucose and PAA as carbon precursors via Method 1 in oxygen atmosphere.